

**MECHANICAL PROPERTIES AND
MICROSTRUCTURAL
CHARACTERISATION OF MULTI
DIRECTIONAL FORGED AND HEAT
TREATED Zn-24Al-2Cu ALLOY**

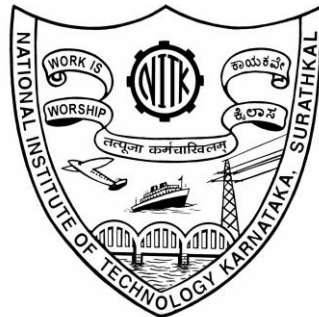
Thesis

Submitted in partial fulfillment of the requirements for the degree of

DOCTOR OF PHILOSOPHY

by

SHARATH P. C



**DEPARTMENT OF METALLURGICAL AND MATERIALS
ENGINEERING**

NATIONAL INSTITUTE OF TECHNOLOGY KARNATAKA

SURATHKAL, MANGALURU-575025

JANUARY, 2018

D E C L A R A T I O N

I hereby declare that the Research Thesis entitled “**MECHANICAL PROPERTIES AND MICROSTRUCTURAL CHARACTERIZATION OF MULTI DIRECTIONAL FORGED AND HEAT TREATED Zn-24Al-2Cu ALLOY**” which is being submitted to the **National Institute of Technology Karnataka, Surathkal** in partial fulfillment of the requirements for the award of the Degree of **Doctor of Philosophy** in the **Department of Metallurgical and Materials Engineering** is a bonafide report of the research work carried out by me. The material contained in this Research Thesis has not been submitted to any University or Institution for the award of any degree.

Register Number : **138019MT13FO6**

Name of the Research Scholar : **Sharath P. C.**

Signature of the Research Scholar :

Department of Metallurgical and Materials Engineering

Place : **NITK-Surathkal**

Date :

C E R T I F I C A T E

This is to certify that the Research Thesis entitled “**MECHANICAL PROPERTIES AND MICROSTRUCTURAL CHARACTERIZATION OF MULTI DIRECTIONAL FORGED AND HEAT TREATED Zn-24Al-2Cu ALLOY**” submitted by **Mr. Sharath P. C. (Register Number: 138019MT13FO6)** as the record of the research work carried out by him, is accepted as the Research Thesis submission in partial fulfillment of the requirements for the award of degree of **Doctor of Philosophy.**

Research Guides

Dr. Preetham Kumar G. V.
Assistant Professor

Prof. K. Rajendra Udupa
Professor

Chairman - DRPC

Date:

ACKNOWLEDGEMENT

I would like to express my deep heart felt feelings of gratitude to my guides Dr. Preetham Kumar G V, Assistant Professor and Dr. K Rajendra Udupa, Professor, Department of Metallurgical and Materials Engineering for their excellent guidance and support throughout the work. Both of them have been an excellent mentor and a constant source of energy, ideas and enthusiasm. I cannot thank them enough for the support they have given me and for their patience as I worked through this thesis.

I am grateful to Dr. Udaya Bhat K, Associate Professor and current Head of the Department of Metallurgical and Materials Engineering, NITK, Surathkal and Dr. Jagannath Nayak, Professor and previous Head of the Department of Metallurgical and Materials Engineering for the laboratory facility made available. I would also like to thank Dr. K Narayana Prabhu, who was the Head, Department of Metallurgical and Materials Engineering at the time of my admission.

I am also grateful to my Research Progress Assessment Committee members: Dr. Anish S, Assistant Professor, Department of Mechanical Engineering and Dr. Subray R Hegde, Assistant Professor, Department of Metallurgical and Materials Engineering for their insightful suggestions, advice and patience.

I am thankful to get constant encouragement and support from all the Teaching and Non-Teaching staff of the Department of Metallurgical and Materials Engineering, NITK, Surathkal, during the entire research work. I would like to express my sincere thanks and gratitude to Applied Mechanics Department staff for their kind help, encouragement for the successful completion of this research work.

I would like to thank my parents for their wise counsel and sympathetic ear. You are always there for me. Finally, there are my friends. We were not only able to support each other by deliberating over our problems and findings, but also happy by talking about things other than our research papers.

Sharath P C

Abstract

Multi directional forging (MDF) is one of the techniques to achieve severe plastic deformation (SPD) which yields ultrafine grained metallic materials. In this technique, the material is compressed in a channel die to a fixed strain, retaining its shape by appropriately rotating it over the three axis. In the present investigation, the MDF process was carried out on selected Zn-24Al-2Cu alloy at two different temperatures, viz., 100 °C for three passes and 200 °C for six passes. Further, the MDF process was subjected to age hardening treatment by following the sequence of solutionizing, MDF processing and post aging. The aging studies were carried out by the choice of aging temperature between 100 to 250 °C and aging curves were generated. Further, all mechanical characterizations of the material were carried out on the test samples which had been aged at 100 °C for one hour as this combination of parameters yielded highest hardness in all the categories of sample.

Techniques like optical microscopy, electron microscopy and X-Ray diffractometry were used to characterize and analyze the microstructure of MDF processed and age hardened materials. Microstructural analysis revealed that the MDF processing reduces the grain size, yielding fine grained materials, apart from well-distributed phases. The microstructure is observed to be consisting of three phases, viz., Al-rich α phase, Zn-rich η phase and CuZn_4 ϵ phase.

Mechanical characterization of the materials revealed an important fact that strength and hardness increased along with the ductility. It was attributed to fineness of grain and evolution of phases in a favorable manner because of MDF and aging treatment meted out to the material.

The creep behavior of the material is investigated by conducting the indentation creep test with 2 kg and 2.5 kg load at different temperatures from 30 to 150 °C. The MDF processed material is found to lose its creep resistance substantially mainly because of microstructural refinement. It was possible to infer from the determination of value of

activation energy that creep occurred by various mechanisms at different temperature regimes. Those mechanisms include dislocation creep and diffusional creep.

Wear behavior of the materials was assessed by conducting the test on pin on disc machine resorting optimization of parameters using Taguchi method. It was proved that processing the materials by MDF followed by post-aging improved the wear resistance of the materials. Wear mechanism was observed to be abrasive type in the case of solutionized samples and adhesive type in MDF-processed samples as revealed by SEM investigations on worn surface.

Keywords: Zn-Al-Cu alloy, Multi Directional Forging, Microstructure, Mechanical properties, Grain Refinement, Precipitation hardening, Creep and Wear.

CONTENTS

ACKNOWLEDGEMENT	
ABSTRACT	
CONTENTS	i
LIST OF FIGURES	v
LIST OF TABLES	xi
NOMENCLATURE	xiii
1. INTRODUCTION	1
1.1 Objectives of the Present Work	3
1.2 Contribution of the Present Work	4
1.3 Organization of the Thesis	5
2. LITERATURE REVIEW	7
2.1 Severe Plastic Deformation	7
2.2 Multi Directional Forging Process	8
2.3 Process Parameters of MDF Process	9
2.3.1 Strain Imposed	9
2.3.2 Strain Rate	9
2.3.3 Pressing Temperature	10
2.3.4 Friction and Lubrication	10
2.4 Advantages and Disadvantages of MDF	10
2.4.1 Advantages of MDF	10
2.4.2 Disadvantages of MDF	11
2.5 Zinc-Aluminium Alloys	11
2.6 Precipitation Hardening in Zn-Al Alloy	15
2.7 Effect of Severe Plastic Deformation on Zn-Al Alloy	18
2.8 Creep	20

2.9	Creep Mechanism	22
	2.9.1 Diffusion Creep	22
	2.9.2 Dislocation Creep	23
	2.9.3 Dislocation Glide	24
	2.9.4 Grain Boundary Sliding	24
2.10	Creep Behavior of Zn and Zn-Al Alloy	24
2.11	Wear	27
2.12	Wear Mechanism	27
	2.12.1 Adhesive Wear	27
	2.12.2 Abrasive Wear	28
	2.12.3 Corrosive Wear	29
	2.12.4 Fretting Wear	29
	2.12.5 Erosive Wear	29
	2.12.6 Delamination Wear	30
2.13	Wear Studies on SPD Processed Materials	30
2.14	Taguchi Method	32
2.15	Taguchi's Approach on Wear Behavior	35
3.	EXPERIMENTAL PROCEDURES	37
3.1	Material	37
3.2	Multi Directional Forging	38
3.3	Precipitation Hardening	42
3.4	Microstructural Analysis	43
	3.4.1 X-Ray Diffractometry	43
	3.4.2 Optical Microscopy	43
	3.4.3 Scanning Electron Microscopy	43
	3.4.4 Transmission Electron Microscopy	44
3.5	Mechanical Property Evaluation	44
	3.5.1 Hardness Measurement	44
	3.5.2 Tensile Test	45

3.5.3	Compression Test	46
3.5.4	Impression Creep Test	47
3.5.5	Wear Test	50
3.5.6	Design of Experiments for Wear Test	51
4.	RESULTS AND DISCUSSION	53
4.1	Zn-24Al-2Cu Alloy	53
4.2	MDF of Zn-24Al-2Cu	55
4.2.1	XRD Analysis	55
4.2.2	Microstructure	56
4.2.3	Mechanical Properties	58
4.2.4	Fractography	64
4.3	Precipitation Hardening of Zn-24Al-2Cu	66
4.3.1	Age Hardening Profile	66
4.3.2	XRD Analysis	67
4.3.3	Solutionized and Aging at 100 °C for One Hour	73
4.4	MDF with Aging at 100 °C for One Hour	73
4.4.1	XRD Analysis	74
4.4.2	Microstructure	75
4.4.3	Mechanical Properties	77
4.4.4	Fractography	84
4.5	Formation of Fine-Grained Structure by MDF Process: TEM Studies	86
4.6	Impression Creep Test	88
4.6.1	Stress Exponent	94
4.6.2	Apparent Activation Energy	95
4.6.3	Threshold Stress	95
4.6.4	True Activation Energy and Creep Mechanism	99
4.6.5	Microstructural Characterization: TEM Studies	100
4.7	Dry Sliding Wear Test	103
4.7.1	Wear Study on Solutionized Specimens Using Taguchi Method	103

4.7.2 Analysis of Variance	105
4.7.3 Multiple Linear Regression Model	106
4.7.4 Confirmation Test	107
4.7.5 Wear Behavior of Solutionized and Aged, MDF Processed, MDF with Post-Aging Samples using Optimized Parameters	108
4.7.6 Mechanism of Wear	109
5. CONCLUSIONS	115
REFERENCES	119
LIST OF PUBLICATIONS	
BIO-DATA	

LIST OF FIGURES

<u>Fig. No.</u>	<u>Contents</u>	<u>Page No.</u>
2.1	Schematic diagram of MDF processing along the three directions of the sample	9
2.2	Phase diagram of Zn-Al binary alloy system	12
2.3	Isothermal sections of Zn-Al-Cu ternary alloy phase diagram at (a) 200 °C, (b) 350 °C, (c) 550 °C and (d) 700 °C	14
2.4	Hardness versus time profiles of aging heat treatment samples at 100, 150 and 250 °C	17
2.5	Schematic view of typical creep curve	21
2.6	Schematic diagram of the indentation creep test	21
2.7	Creep deformation mechanism map for coarse pure Zn	25
2.8	Illustration of (a) two body abrasive wear and (b) three body abrasive wear	28
3.1	EDAX analysis of as-received Zn-Al alloy	38
3.2	Two dimensional representation of (a) MDF die and (b) base plate	39
3.3	Schematic three dimensional representation of the MDF split type die with plunger	40
3.4	Photograph of multi directional forging die assembly	40
3.5	Photograph of the 200 ton hydraulic press	41
3.6	Zn-24Al-2Cu alloys after MDF processing at (a) room temperature, (b) 100 °C up to three passes and (c) 200 °C up to six passes	42
3.7	Schematic diagram of tensile test specimens in accordance with ASTM E-8 standard	45
3.8	Photograph of tensile test specimen	45
3.9	Compression test specimens in accordance with ASTM E9-09 standard (a) schematic view and (b) photographic image	46
3.10	Apparatus used for impression creep test	48
3.11	Split cage used in the impression creep test	48

3.12	Indenter used in the impression creep test	49
3.13	Schematic creep curve of indentation strain versus time	50
3.14	Pin-on-disc tribometer (a) schematic diagram and (b) photograph of pin on disc wear testing machine	51
4.1	Optical micrograph of as-cast Zn-24Al-2Cu alloy (100X Magnification)	53
4.2	Solutionized sample (a) optical micrograph (500X Magnification) (b) SEM micrograph (3% Nital etchant)	54
4.3	XRD patterns of (a) solutionized (b) MDF -100 °C-3P, (c) MDF-200 °C-3P and (d) MDF-200 °C-6P	55
4.4	Multidirectional forged sample at 100 °C up to three passes (a) optical micrograph (1000X Magnification) and (b) SEM micrograph (3% Nital etchant)	56
4.5	Multidirectional forged sample at 200 °C up to three passes (a) optical micrograph (1000X Magnification) and (b) SEM micrograph (3% Nital etchant)	57
4.6	Multidirectional forged sample at 200 °C up to six passes (a) optical micrograph (1000X Magnification) and (b) SEM micrograph (3% Nital etchant)	57
4.7	Bar chart showing Rockwell hardness variations with solutionized, MDF processed at 100 °C up to three passes and 200 °C up to three and six passes	58
4.8	Engineering stress versus engineering strain graph from tensile test after solutionized, MDF processed at 100 °C up to three passes and 200 °C up to three and six passes	59
4.9	Bar chart showing ultimate tensile strength and percentage of elongation for solutionized, MDF processed at 100 °C up to three passes and 200 °C up to three and six passes	59
4.10	True stress versus true strain graph from compression test after solutionized, MDF processed at 100 °C up to three passes and 200 °C up to three and six passes	61

4.11	Bar chart showing strength co-efficient (K) and strain hardening exponent (n) from compression test for solutionized and MDF processed at 100 °C up to three passes and 200 °C up to three and six passes	63
4.12	Movements of dislocation: (a) conservative (b) non-conservative and (c) non-conservative movements creating interstitials	64
4.13	SEM images of the fracture surfaces of alloy after tensile tests in (a) as-cast (b) solutionized (c) MDF at 100 °C up to three passes and (d) MDF at 200 °C up to six passes	65
4.14	Hardness curves of the Zn-24Al-2Cu alloy artificially aged at 100, 150, 200 and 250 °C for different times	66
4.15	XRD patterns of sample solution treated at 365 °C for 5 hours, water-quenched and aged at 100 °C for different durations; with enlarged view showing τ' phase after three hours of aging	68
4.16	XRD patterns of sample solution treated at 365 °C for 5 hours water quenched and aged at 150 °C for different durations; with enlarged view showing τ' phase after one hours of aging	69
4.17	XRD patterns of sample solution treated at 365 °C for 5 hours water quenched and aged at 200 °C for different durations; with enlarged view showing τ' phase after one hours of aging	70
4.18	XRD patterns of sample solution treated at 365 °C for 5 hours water quenched and aged at 250 °C for different durations; with enlarged view showing τ' phase after 1 hours of aging	71
4.19	Aging time for appearance of τ' phase versus aging temperature from XRD analysis	72
4.20	(a) Optical micrograph (500X Magnification) (b) SEM micrograph of solutionized and aged at 100 °C for one hour (3% Nital etchant)	73
4.21	XRD patterns of (a) solutionized sample (b) MDF-100 °C-3P+aging, (c) 200 °C-3P+aging and (d) 200 °C-6P+aging	74

4.22	Multidirectional forged sample at 100 °C up to three passes and post aging at 100 °C for one hour (a) optical micrograph (500X Magnification) (b) SEM micrograph (3% Nital etchant)	76
4.23	Multidirectional forged sample at 200 °C up to three passes and post aging at 100 °C for one hour (a) optical micrograph (500X Magnification) (b) SEM micrograph (3% Nital etchant)	76
4.24	Multidirectional forged sample at 200 °C up to six passes and post aging at 100 °C for one hour (a) optical micrograph (500X Magnification) (b) SEM micrograph (3% Nital etchant)	77
4.25	Bar chart showing Rockwell microhardness after MDF processed at 100 °C up to three passes and 200 °C up to three and six passes with aging	78
4.26	Engineering stress versus engineering strain graph from tensile test for solutionized and aging and after post-aging of MDF processed at 100 °C up to three passes and 200 °C up to three and six passes	79
4.27	Bar chart showing ultimate tensile strength and percentage of elongation after post-aging of MDF processed at 100 °C up to three passes and 200 °C up to three and six passes with aging	80
4.28	True stress versus true strain graph from compression test for solutionized and aging and after post-aging of MDF processed at 100 °C up to three passes and 200 °C up to three and six passes	81
4.29	Strength coefficient (K) and strain hardening exponent (n) obtained from compression test for aging at 100 °C for one h, MDF processed at 100 °C up to three passes with post-aging and 200 °C up to three and six passes with post-aging	83
4.30	SEM images of the fracture surfaces of alloy after tensile tests of (a) Solutionized and aging at 100 °C for one hour (b) MDF at 100 °C up to three passes with post-aging (c) MDF at 200 °C up to three passes with post-aging and (d) MDF at 200 °C up to six passes with post-aging	85

4.31	(a) Schematic view of deformed structure, (b) TEM micrograph of MDF at 100 °C up to three passes and (c) TEM micrograph of MDF at 200 °C up to three passes	86
4.32	(a) Schematic representation of lamellar boundaries (b) TEM micrograph of MDF at 200 °C up to six passes and (c) enlarged image of (b) showing grain subdivision at large strain (d) TEM micrograph of MDF at 200 °C up to six passes with aging	87
4.33	Typical impression creep curves of the materials tested under constant load of 2 kg at 30 °C for solutionized sample	88
4.34	Typical impression creep curves of the materials tested under constant load of 2 kg and temperature range of 30 – 150 °C: (a) solutionized (b) MDF at 100 °C for three passes (c) MDF at 200 °C for three passes and (d) MDF at 200 °C for six passes	90
4.35	Typical impression creep curves of the materials tested under constant load of 2.5 kg and temperature range of 30 – 150 °C: (a) solutionized (b) MDF at 100 °C for three passes (c) MDF at 200 °C for three passes and (d) MDF at 200 °C for six passes	92
4.36	Comparison of steady state creep rate obtained at different temperatures for the materials tested at: (a) 2 kg load and (b) 2.5 kg load	93
4.37	Double linear plot for $\dot{\epsilon}^{1/2}$ versus stress at different temperatures (a) solutionized, (b) MDF at 100 °C up to three passes, (c) MDF at 200 °C up to three passes and (d) MDF at 200 °C up to six passes	96
4.38	Semi-logarithmic plot for normalized threshold stress (σ_0/E) versus reciprocal of absolute temperature for solutionized sample	98
4.39	Bright field TEM micrograph of (a) MDF at 100 °C for three passes (b) MDF at 200 °C for six passes reveals large number of dislocations and (c) images showing nano-crystalline dispersion particles inside the α phase shown in (b)	101
4.40	X-Ray diffraction patterns of the different processed conditions after creep test at 150 °C; enlarged view showing τ' phase peak	102

4.41	Main effect plot of S/N ratio on specific wear rate	105
4.42	Variations of specific wear rate for different processing conditions	108
4.43	SEM micrographs showing the appearance of worn surfaces of (a) solutionized, (b) MDF at 100 °C up to three passes and (c) MDF at 200 °C for six passes	109
4.44	SEM micrographs showing enlarged images of worn surfaces (a) of brittle fragmentation in MDF at 100 °C up to three passes, (b) with ϵ particles in η phase for MDF at 100 °C up to three passes and (c) with migrated particles for MDF at 200 °C up to six passes	110
4.45	Results of EDS analysis on the worn surface of the Zn-24Al-2Cu alloy (a) MDF at 100 °C up to three passes (see Figure 4.39b) and (b) MDF at 200 °C up to six passes	110
4.46	SEM micrograph showing the subsurface regions of (a) solutionized, (b) MDF at 200 °C up to six passes and (c) MDF at 200 °C up to six passes with post-aging tested for 1.15 h corresponding to a sliding distance of 4500 m at a load of 88.25 N and a sliding speed of 1 m.s ⁻¹	111

LIST OF TABLES

<u>Table No.</u>	<u>Contents</u>	<u>Page No.</u>
2.1	Thermodynamic data for Zn and Al	24
2.2	Summary of creep data for various Zn-Al alloy	26
2.3	Taguchi's L ₉ orthogonal array	35
3.1	Chemical composition of the Zn alloy used in the present work	37
3.2	Levels of variables used in the experiment	51
3.3	Taguchi's L ₉ orthogonal array	52
4.1	Strength coefficient (K) and strain hardening exponent (n) values for various processing without aging conditions	62
4.2	Strength coefficient (K) and strain hardening exponent (n) values for various processing with aging conditions	82
4.3	Ultimate tensile strength, ductility and average grain size for various processing conditions	84
4.4	Variations of stress exponent with temperature for different processing conditions	94
4.5	Apparent activation energy (Q _a) values	95
4.6	Threshold stress (σ_0) values	97
4.7	Variations of stress exponent by considering effective stress	98

4.8	True activation (Q_i) values	99
4.9	Experimental layout using the L_9 orthogonal array and performance results for dry sliding wear test for Zn-24Al-2Cu alloy under solutionized condition	104
4.10	Response table of S/N ratios on specific wear rate	105
4.11	Analysis of variance for S/N Ratio	106
4.12	Parameters and values used in the confirmation test and their comparison with a regression model	107

NOMENCLATURE

ARB: Accumulative Roll Bonding

ECAP: Equal Channel Angular Pressing

EDAX: Energy Dispersive X-Ray

HCP: Hexagonal Close Packed

HPT: High Pressure Torsion

HV: Vickers Microhardness

MDF + A: Multi Directional Forging Combined with Aging

MDF: Multi Directional Forging

OM: Optical Microscopy

SEM: Scanning Electron Microscopy

SPD: Severe Plastic Deformation

TEM: Transmission Electron Microscopy

UFG: Ultrafine Grain

UTS: Ultimate Tensile Strength

XRD: X-Ray Diffractometry

α : Al rich FCC phase

η : Zn rich HCP phase

ε : CuZn₄ HCP phase

β : Zn rich FCC phase

τ' : Distorted BCC structure, $\text{Zn}_{10}\text{Al}_{35}\text{Cu}_{55}$

k: Boltzmann constant = $1.38064852 \times 10^{-23} \text{ m}^2 \text{ kg s}^{-2} \text{ K}^{-1}$

K: Strength coefficient

n: Strain hardening exponent

T_m : Melting temperature

CHAPTER 1

INTRODUCTION

In recent years, ultrafine or nanostructured materials processed by severe plastic deformation (SPD) methods are growing in demand and find applications in many fields of industry (Valiev et al., 2000). These processes offer the possibility for the production of ultra-fine grained microstructures in bulk quantities. In ultra-fine grained microstructures, grain sizes are in between 0.1 - 1 μm . In the process of severe plastic deformation, suitable materials are subjected to the imposition of very large strains without the introduction of any concomitant changes in the cross-sectional dimensions of the sample. The main advantage of SPD processes is that high strain can be imparted to a specimen by repeatedly processing the material several times using the same die. This leads to the accumulation of plastic strain in the material. Conventional methods of materials processing such as cold rolling or drawing do not provide such high levels of strain to the material without failure. Materials processed by SPD methods have resulted in overcoming a number of difficulties associated with residual porosity for compacted samples, impurities in the case of ball milling. SPD processed materials are sufficiently large for use in real commercial structural applications. Several SPD processing methods are developed. These methods are as follows: (i) High pressure torsion (HPT) (Zhilyaev et al., 2008), (ii) Equal channel angular pressing (ECAP) (Valiev and Langdon, 2006), (iii) Accumulative roll bonding (ARB) (Saito et al., 1998), (iv) Cyclic extrusion and compression (CEC) (Korbel et al., 1985) and (v) Multi directional forging (MDF) (Salishchev et al., 1995). The ultra-fine grained materials processed by the above methods are found to have excellent super plasticity, high wear resistance, enhanced high cycle fatigue life and good corrosion resistance. The superior properties of these materials are derived from their unique microstructures which control the deformation mechanisms and

mechanical behavior. These characteristics of SPD processes make themselves a novel technique in materials processing.

In MDF process, materials are subjected to very large strains without the introduction of any concomitant changes in the cross sectional dimensions of the samples. High strain can be imparted to a sample by repeatedly processing the material several times using the same die. This leads to the accumulation of plastic strain in the material. The homogeneity of strain provided by MDF is lower than that by ECAP and torsion straining. However, the method allows one to obtain a nanostructured state in rather brittle materials because processing starts at elevated temperature and specific loads on tooling are low. Based on the classical MDF techniques, more exotic methods were developed. Some of them are cyclic closed die forging (CCDF) and cone-cone method (CCM), cyclic expansion-extrusion CEE - a modified CEC process (Estrin and Vinogradov, 2013).

MDF process is the focus of the present study because of its simplicity where conventional forging machine is sufficient to deform the material by using channel dies in plane strain condition. MDF processing of metals with cubic crystals such as aluminum, copper and steel are well studied and documented. However, MDF processes on hexagonally crystal packed (HCP) structured materials, most of its effects on microstructures and mechanical properties are still to be understood. One of the difficulties in the processing of HCP materials such as zinc, magnesium and titanium is that the rate of strain hardening is lower in these metals than that in cubic metal where higher number of slip systems is active at any instant of time. Based on this reason, fundamental experiments are carried out on the Zn-24Al-2Cu alloy to understand the microstructures and mechanical properties after MDF process and heat treatment.

Zn-Al based alloys were developed in a number of grades such as (i) ZA 8 (Zn-8 wt. % Al), (ii) ZA12 (Zn-12 wt. % Al), (iii) ZA22 (Zn-22 wt. % Al) and (iv) ZA27 (Zn-27 wt. % Al) (Zhu and Islas, 1997). These alloys exhibit excellent castability and wear resistance, making it widely used in general engineering applications and as a replacement of their conventional counterparts like aluminum cast alloys, copper-based

alloys and cast iron (Prasad, 1998). In particular, ZA alloys are used in bearings where higher strength with lower density is needed. The high plasticity of Zn-22 wt. % Al alloy is advantageous to the forming process, but its low hardness has limited its application. In the real casting conditions the zinc-aluminum alloys have the typical dendritic structure, wherein the dendritic size and inter-dendritic spacing depends on the casting process parameters. The cooling rate imposes a strong influence on the grain size. But, controlling the cooling rate during casting process is tedious and offers limited advantages particularly in thick sections. In addition, the dendritic structure exhibits lower ductility, as well as relatively high level of heterogeneity in mechanical properties (Babic et al., 2010). Copper in 1 - 3 weight percentages are added to improve its strength which results in another problem like dimensional instability due to the formation of the meta-stable phase ϵ (CuZn_4) during the solidification of the alloy. The ϵ phase, then tends to transform to the stable τ' phase ($\text{Al}_5\text{Cu}_4\text{Zn}$) (Babic et al., 2007). For overcoming these deficiencies, possible measure is through the heat treatment of as-cast material. In this regard, the detailed evaluation of the transformation of phases during thermomechanical treatment of Zn-24 wt. % Al-2 wt. % Cu alloy and the mechanism behind the deformation need to be investigated. Therefore, understanding the precipitation hardening combined with severe plastic deformation of the Zn-24Al-2Cu alloy is important to determine the applicability in the structural engineering field. Particularly for bearing applications at elevated temperatures, wear and creep properties are important which need to be considered. Hence, creep and wear behavior of MDF processed Zn-24Al-2Cu alloy are studied.

1.1 Objectives of the Present Work

The objectives of the present work are stated below:

- 1 To process Zn – 24 Al – 2 Cu alloy through severe plastic deformation by the technique of multi directional forging (MDF).
- 2 To study the influence of precipitation hardening on the mechanical properties of MDF processed material.

- 3 To establish structure-property correlations with the purpose of understanding the possible enhancement in mechanical properties using optical microscope, SEM, TEM and XRD.
- 4 To study the creep behavior of MDF processed Zn – 24 Al – 2 Cu alloy using the indentation creep technique, and to suggest the mechanism of creep under different conditions.
- 5 Wear study of solutionized Zn - 24 Al - 2 Cu alloy and wear study of Zn - 24 Al- 2 Cu alloy processed by multi directional forging and aging, using Taguchi method of optimization.

1.2 Contribution of the Present Work

In the present investigation, zinc alloys were taken for improving their mechanical properties through the study of reduction in grain size combined with heat treatment. Precipitation hardening heat treatment studies have been performed to evaluate the peak aging temperature and time. MDF processed at 200 °C up to six passes combined with aging sample results in a 40 % increase in ultimate tensile strength and 32 % increase in ductility as compared to initial solutionized sample. A very good microstructural stability was observed after impression creep test on MDF processed at 200 °C up to six passes alloy as compared to other MDF processed alloys. Wear resistance of MDF processed samples is improved and mechanism behind is explained. Hence, in the present work, the MDF processed sample with total equivalent strain of 1.2 is having better mechanical properties as compared to total equivalent strain of 0.6 MDF processed samples. Hardness, tensile strength, ductility and wear properties have been improved after MDF processing and reasons behind are explained in detail.

1.3 Organization of the Thesis

A brief chapter wise description of the thesis is as follows:

Chapter 1 gives the introduction of the multi directional forging process and about zinc based alloys. The broad objectives of the present research work are prescribed through the literature review gap.

Chapter 2 provides a literature review on severe plastic deformation (SPD) processing, multi directional forging process, principles of operation, experimental factors influencing MDF process, about Zn-Al-Cu alloy, effect of SPD on Zn-Al binary alloy, creep and its mechanisms, wear and its mechanisms and Taguchi method. The gaps existing in the areas of ongoing research are noted.

Chapter 3 covers the details about the as-received Zn-24Al-2Cu alloy, solutionizing heat treatment, MDF process setup and explains the experimental procedure for multiple passes at different temperatures. Characterization techniques have been informed and impression creep behavior of MDF processed samples for two different loads and different temperatures from 30 to 150 °C is explained. Further, wear study of solutionized and MDF processed samples using the Taguchi technique is described.

Chapter 4 reports the results and discussion of the experiments carried out and inferences drawn from the MDF processing of Zn-24Al-2Cu alloy combined with precipitation hardening heat treatment. Further, microstructural characterization of the materials, mechanical properties of the alloy, fracture topography, impression creep behavior and dry sliding wear behavior of solutionized and MDF processed material are stated.

Chapter 5 provides the conclusions drawn from the current study and scope for future work.

CHAPTER 2

REVIEW OF LITERATURE

Conventional metal forming processes such as extrusion, rolling and forging are the plastic deformation processes which alter the structure for improved mechanical properties. In order to improve grain refinement, it is necessary to impose an exceptionally high strain to introduce high density of dislocation which in turn forms an array of grain boundaries. Conventional metal forming limits the amount of strain that can be produced and there exists a lower limit of grain size that can be achieved by these processes.

In recent years, bulk ultrafine grains (UFG) or nanocrystalline materials processed by severe plastic deformation (SPD) methods are the focus of interest for many researchers. This research interest is not only limited to physical and mechanical properties inherent to UFG or nanocrystalline materials, but also to the ease of processing compared to other methods. UFG materials can be produced from bottom up approach such as ball milling, inert gas condensation method or by electro deposition. But, SPD processed materials can overcome a number of drawbacks such as porosity in compacted samples, lack of complete bonding and impurities derived from ball milling (Valiev and Langdon, 2006).

2.1 Severe Plastic Deformation

Severe plastic deformation process is defined as “Technique of metal forming in which higher strain is imposed on the bulk material without the introduction of any concomitant changes in the overall dimensions of the sample and having the ability to produce exceptional grain refinement” (Valiev et al., 2006). The formation of ultrafine grains or nanostructures in bulk materials has been achieved by SPD method through the introduction of high density of dislocations and these dislocations rearrangements for the formation of grain boundaries under lower processing temperatures. Different types of SPD processing methods are available today which include: (i) High Pressure Torsion

(HPT), (ii) Equal Channel Angular Pressing (ECAP), (iii) Cyclic Extrusion and Compression (CEC) and (iv) Accumulative Roll Bonding (ARB) (Zehetbauer and Zhu, 2009). One more process later added to the list is Multi Directional Forging or Multi Axial Forging (MDF/MAF) in which plastic deformation takes place under extensive hydrostatic pressure. These processes alter the properties by changing the grain size and structure to ultrafine or nanocrystalline structures in various metals and alloys. Technique of MDF has received little attention when compared with other SPD processes such as ECAP, ARB and HPT.

2.2 Multi Directional Forging Process

Multi directional forging (MDF) is an advanced metal forming process capable of producing plastic deformation in a variety of materials. It is the simplest method to achieve larger strains with minimum dimensional changes and allows processing of bulk materials. Simple plane strain condition is used for the deformation of material and to alter its mechanical properties. Salishchev et al. (1995) and Kaibyshev (2001) developed an MDF process in the early 1990s and used it to refine the grains in bulk materials. In MDF process, materials are imparted to very large strains without the introduction of any concomitant changes in the cross-sectional dimensions of the samples. High strain can be imparted to a sample by repeatedly processing the material several times using the same die. This leads to the accumulation of plastic strain in the material.

MDF process involves plane strain deformation condition that is achieved by compressing the work piece through the split type die. In this process, the sample is forged to a predetermined strain in the MDF die then forged sample is removed and rotated to another direction. Subsequently the sample is reinserted into the die and pressed to the same strain as in previous passes which is shown in Figure 2.1. Along with deformation strain, processing temperature plays a critical role in refining the grain structure (Miura et al., 2012).

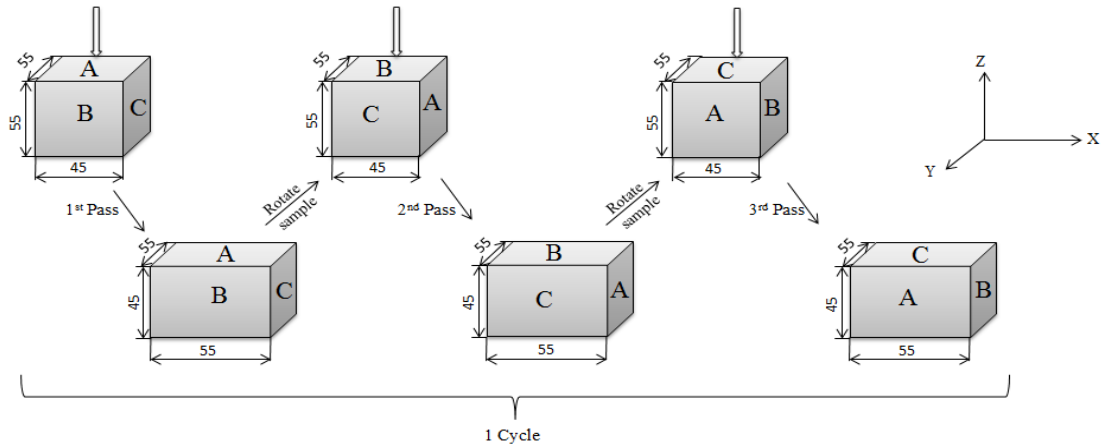


Figure 2.1 Schematic diagram of MDF processing along the three directions of the sample.

2.3 Process Parameters of MDF Process

Many factors influence the properties of the materials during MDF process. They are (i) Strain imposed, (ii) Pressing speed, (iii) Pressing temperature and (iv) Friction and lubrication.

2.3.1 Strain Imposed

Estrin and Vinogradov (2013) have given the expression for total effective strain (ϵ_{eff}) imparted on the MDF sample and it is given by,

$$\epsilon_{\text{eff}} = N \frac{2}{\sqrt{3}} \ln \left(\frac{h_i}{h_0} \right) \quad \text{Equation 2.1}$$

Where N is number of passes and h_i , h_0 are the initial height and width of the specimen.

As the number of MDF pass increases which leads to reduction in grain size of the material and increase in the fraction of high angle grain boundaries.

2.3.2 Strain Rate

At slow pressing speeds, the microstructure of the MDF processed materials showed more equilibrium structure. Since the pressing speed is directly related to the strain rate imposed on the material, it is reasonable to expect a more equilibrium structure at a slow

speed due to longer time available for the recovery process. Miura et al. (2016) carried out a study on the effects of strain rate during MDF on AZ80 Mg alloy. MDF was carried in the range of 3×10^{-3} to $3 \times 10^{-1} \text{ s}^{-1}$ under the same temperature. Less homogeneous microstructure was evolved for a strain rate of $3 \times 10^{-1} \text{ s}^{-1}$ as compared to $3 \times 10^{-3} \text{ s}^{-1}$.

2.3.3 Pressing Temperature

In general, materials can be deformed easily at high processing temperatures. If the pressing operation is carried out at the lowest possible temperature without any significant cracking in the specimen, it is possible that finer grain size with higher fraction of high angle grain boundaries can be obtained. In MDF process, the upper limit of processing temperature is well below the recrystallization temperature ($0.5 T_m$, where T_m is melting point of the material) (Sakai et al., 2014). Al based alloys were processed under cryogenic temperature by Rao et al., (2014) which resulted in equiaxed subgrain structures.

2.3.4 Friction and Lubrication

In MDF process, lubrication reduces the friction between the die and workpiece. Subsequently, the amount of redundant shear strain is reduced and plane strain compression conditions are expected throughout the sample.

2.4 Advantages and Disadvantages of MDF

Compared to conventional metal working operations such as rolling, extrusion or forging MDF process has many important features, uniqueness and benefits.

2.4.1 Advantages of MDF

The multi directional forging process is the simplest plastic deformation process for the following reasons.

- i. Conventional forging machine is sufficient for MDF processing of large scale samples which does not require installing advanced apparatus/tools. Thus, this

process has much more potential usage for both small and large scale industry applications.

- ii. Materials which are hard to deform such as brittle ones and materials possessing high yield strength can be deformed effectively in MDF processing. MDF process is carried out at higher temperatures and the specific load on the tool is low compared to cold deformation.
- iii. As nature of loading in MDF process is simple compression type, data concerning the flow stress and microstructural changes that take place during processing can be recorded simultaneously and correlated to varying strain rate.

2.4.2 Disadvantages of MDF

Compared to other SPD processes such as ECAP and HPT, strain homogeneity attained is poor in the case of MDF process. It is a time-consuming process as this process is not a continuous one because the sample has to be removed and rotated for each subsequent pass.

2.5 Zinc-Aluminium Alloys

Zinc-aluminium (Zn-Al) based alloys were also called as ZAMAK alloys which were developed in the early 1970s at North America and China. The zinc based alloys were developed in a number of grades like ZA8 (Zn-8 wt. % Al), ZA12 (Zn-12 wt. % Al), ZA22 (Zn-22 wt. % Al) and ZA27 (Zn-27 wt. % Al). These alloys exhibit excellent castability and wear resistance, making it widely used in general engineering applications like bearings. These materials are candidate materials for replacement of their conventional counterparts such as aluminum cast alloys, copper based alloys and cast iron (Prasad, 1998). The zinc-aluminum alloys have the typical dendritic structure in the as-cast conditions. The dendritic size and inter-dendritic spacing depends on the casting process parameters. The dendritic structure exhibits lower ductility and high level of heterogeneity in the mechanical properties (Babic et al., 2010). Copper is added in the range of one to three weight percentages to improve the strength of Zn-Al alloys. This would lead to the formation of ϵ (CuZn_4) phase during the solidification which imparts

dimensional instability to the material. The ϵ phase, then tends to transform to the τ' phase (distorted BCC structure, $Zn_{10}Al_{35}Cu_{55}$) (Babic et al., 2007) by which all the advantages of presence of ϵ phase would disappear. To overcome these deficiencies, one possible measure is to provide proper heat treatment.

Along with zinc and higher weight percentage of aluminum, small amount of copper, silicon or iron is added which enhances the elastic modulus, yield strength, wear resistance and corrosion resistance without disturbing the superplastic behavior during the production of components (Villegas et al., 2014).

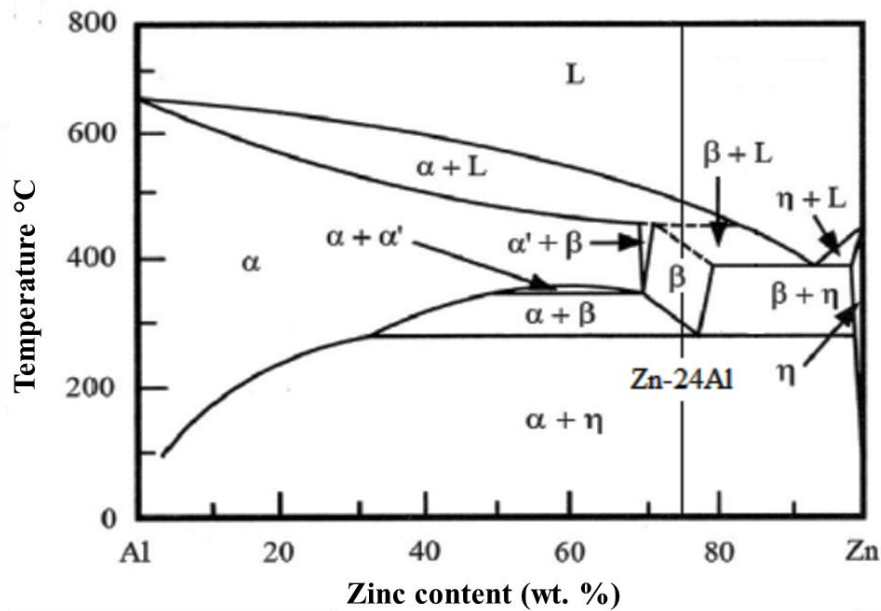


Figure 2.2 Phase diagram of Zn-Al binary alloy system (Zhu, 2004).

Figure 2.2 displays the Zn-Al binary phase diagram initially presented by Presnyakov et al. modified by Goldal and Parr, where α is Al rich phase having face centered cubic (FCC) structure, β is Zn rich phase with FCC structure, η is Zn rich phase having hexagonal close packed (HCP) structure, α' is supersaturated Al rich phase with FCC structure (Zhu, 2004). In the binary phase diagram, three important invariants are observed and it is presented as,

(i) Peritectic transformation at 443 °C with 28.4 wt. % of Al, $\alpha + L \rightarrow \beta$

(ii) Eutectic transformation at 382 °C with 5.1 wt. % of Al, $L \rightarrow \beta + \eta$ and

(iii) Eutectoid transformation at 275 °C with 22 wt. % of Al, $\beta \rightarrow \alpha + \eta$

Microstructural evolution during solidification of hypoeutectic alloy is observed as follows:

(i) Primary dendrites of η phase having 98.86 wt. % of Zn with HCP structure is formed at 382 °C.

(ii) Further cooling the alloy below 382 °C, remaining liquid in between the dendrites gets transformed into eutectic structures namely, η phase and β phase with solute segregation. Here, β phase is having 22 wt. % of aluminum and possess an FCC crystal structure.

(iii) After reaching 275 °C, eutectoid phase transformation occurs and microstructure is having lamellar mixture of $\alpha + \eta$ phase. In the process of eutectoid transformation, decomposition affects only the β phase leaving behind the pro-eutectoid η -phase.

Figure 2.3 shows the Zn-Al-Cu ternary alloy phase diagram referred from the ASM handbook volume 3 Alloy phase diagram (1992). The phase transformations observed in ternary Zn-Al-Cu alloy by Zhu (2004) are represented as follows:



Where β is Zn rich phase (FCC crystal structure), τ' ($\text{Cu}_{55}\text{Al}_{35}\text{Zn}_{10}$) is distorted BCC structure, α is an Al rich phase (FCC crystal structure), ε (CuZn_4) is intermetallic compound having HCP crystal structure and η is Zn rich phase (HCP crystal structure).

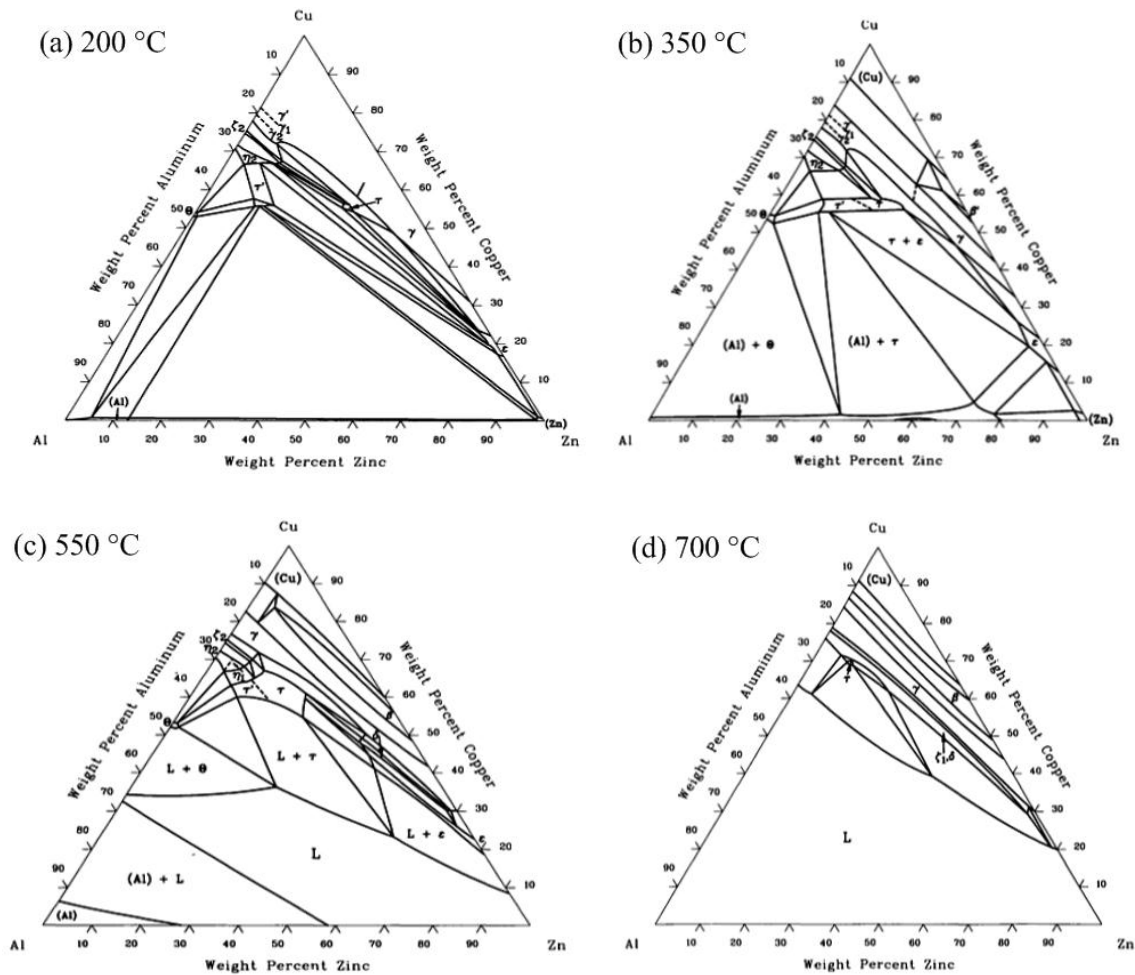


Figure 2.3 Isothermal sections of Zn-Al-Cu ternary alloy phase diagram at (a) 200 °C, (b) 350 °C (c) 550 °C and (d) 700 °C (ASM handbook – Alloy phase diagram).

A few drawbacks are observed in the as-cast ZA alloy for the usage in commercial applications. One such drawback is the presence of dendritic structure which is mainly influenced by solidification mechanism. Microstructural refinement is mainly dependent on the cooling rate of the molten metal in the mold. Because of the presence of dendrites in the as-cast structure, they possess inferior mechanical properties such as ductility and chemical inhomogeneity.

2.6 Precipitation Hardening in Zn-Al Alloy

Resistance to plastic deformation of materials can be improved by refinement of grains, solid solution strengthening and precipitation hardening. In recent times, high strength alloys are produced by a combination of either two or more processes. Hence, precipitation hardening characteristics of Zn-Al alloy is important to understand in particular to severe plastic deformed condition.

For successful precipitation hardening, essential condition is solute atoms in the material must show a substantial decrease in the solid solubility of atoms with decrease in temperature. Precipitation hardening processes of Zn-Al have been expressed in terms of reaction as follows: $\beta \rightarrow \alpha + \eta$. Supersaturated metastable β phase transforms into stable solid solution of α phase and metastable solid solution of η' . From binary phase diagram of Zn-Al alloy as shown in Figure 2.2, alloy consists of a mixture of α and η at room temperature. During solutionizing heat treatment, alloys are heated to certain temperature say above 300 °C (T_1) and then alloy becomes supersaturated metastable β phase. After holding these alloys for sufficiently long time at temperature T_1 for complete homogenization they are rapidly quenched in liquid (water or oil) at room temperature to suppress the formation of metastable supersaturated η' phase. This metastable η' phase is at high energy state with potential driving force for the precipitation of new equilibrium phases. By heating the alloys at certain temperature say T_2 ($T_2 < T_s$, where T_s is solvus temperature) which provides the essential activation energy for the formation of new stable equilibrium α and η phases. This can occur in single transition or may require two or more transitions of phases. The transitions of phases in the precipitation process are dependent on many factors such as alloy composition, solutionizing temperature, cooling rate, aging temperature and time and presence of defects in the alloys.

Earlier studies made on the precipitation hardening heat treatment behavior of Zn-Al binary alloys are presented below.

Zhu and Lee (2000) investigated the precipitation hardening characteristics of furnace cooled Zn-22Al alloy using a tensile mode of deformation. They observed that by holding the samples for 40 min at 150 °C aging temperature, phase transformation took place

with α phase appearing inside the η matrix. The τ' phase was observed after sufficiently long aging period of 5 h. Four phase transformations were revealed after 30 h of aging time without any aid of external deformation. Decomposition of the metastable η phase continued for 15 h at 150 °C.

Dorantes-Rosales et al., (2002) examined the microstructural changes during cold rolling with aging heat treatment of Zn-Al-Cu alloy. After cold rolling, grain size was in the range of about 1-2 μm . Decomposition of β phase into α and η phases occurred at room temperature. Samples which are deformed at 250-270 °C behave in superplastic manner. In the case of aged and rolled samples, α , η and ϵ phases were observed, whereas aging of rolled samples promoted the formation of τ' phase when aging heat treatment was carried out below 250 °C. They suggested that, cold rolled samples enhanced the process of phase transformation and supported the precipitation of τ' phase formation.

Structural coarsening during the aging of Zn-based alloys was investigated by Dorantes-Rosales et al., (2005). Samples were heat treated at 350 °C for a period of 120 h and were allowed to cool in the furnace. The τ' phase was formed by four stages of phase transformation after aging at 100, 200 and 250 °C for different intervals of time. Diffusion-controlled coarsening was followed by the LSW theory (Lifshitz-Slyozov-Wagner theory of Ostwald ripening) in the growth kinetics of τ' phase. Highest hardness occurred in the samples which were subjected to 250 °C aging temperatures with 1.5 h of aging time and lowest hardness was observed in the case of 100 °C aged samples as shown in Figure 2.4. From this study, it is inferred that by controlling the coarsening of the τ' phase hardness of the sample can be controlled.

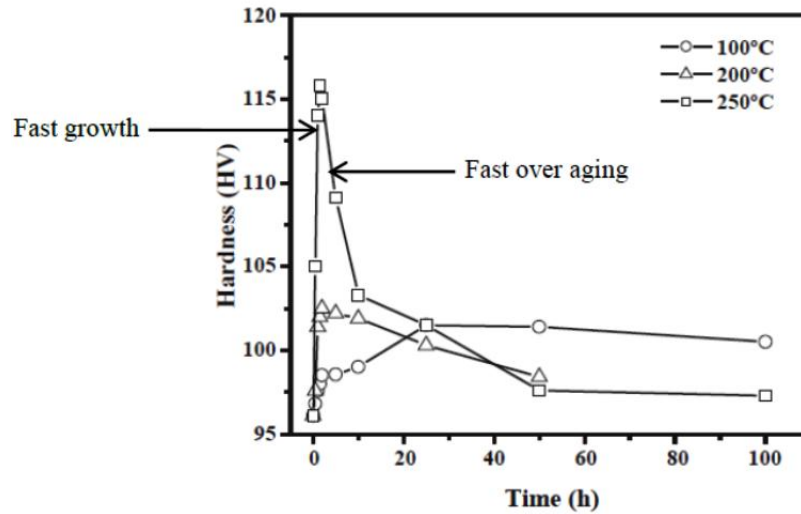


Figure 2.4 Hardness versus time profiles of aging heat treated samples at 100, 150 and 250 °C (Dorantes-Rosales et al., 2005).

Studies on the decomposition of β phase in Zn-22Al and Zn-22Al-2Cu alloys at room temperatures were carried out by Dorantes-Rosales et al., (2007). They observed that unstable β phase decomposed at the faster rate in the case of Zn-22Al alloys as compared to Zn-22Al-2Cu alloys. Slower rate of decomposition is observed in Cu containing alloy than the one without Cu. Hardness of both the alloys increased after aging heat treatment to a maximum of 108 Hv and 149 Hv for Zn-22Al and Zn-22Al-2Cu alloys respectively. Further, heat treatment for sufficiently long time reduces the hardness value of both the alloys due to coarsening of grains in later stages.

The literature survey on the precipitation hardening shows that by the addition of Cu to Zn-Al alloys forms the intermetallic compound called ϵ -phase. After aging heat treatment of Zn-Al-Cu alloy at above 100 °C for sufficient period of time ϵ -phase transforms into τ' phase. It is proposed that by controlling the size of the τ' phase hardness of the sample can be optimized.

2.7 Effect of Severe Plastic Deformation on Zn-Al Alloy

To enhance and achieve the desired mechanical properties of the material, grain refinement is one of the methods. Severe plastic deformation is the recently developed method for producing fine grain size through deforming the materials by large plastic strain imposed under different applied loads and speeds. In this section, the evolution of the mechanical properties and microstructure that have been produced through the SPD processes on Zn-Al alloys have been reported.

Cho et al., (2014) carried out high pressure torsion (HPT) on Zn-Al eutectoid alloy at room temperature. They observed that the strength of the alloy reduced after processing for several turns. It was due to a reduction of lamellar structure and loss of Zn precipitates in the Al rich phase which was observed in the as received material.

Choi et al., (2014) investigated the deformation mechanism of Zn-22% Al processed by HPT up to four turns. They concluded that deformation behavior was highly influenced by grain boundary sliding (GBS). Further, they noted that GBS was higher on the interfaces of Zn-Zn (sliding offset, $w = 0.053 \mu\text{m}$) region followed by Zn-Al ($w = 0.048 \mu\text{m}$) boundaries and minimum on the Al-Al ($w = 0.046 \mu\text{m}$) boundaries with a strain rate of 1 s^{-1} .

Purcek et al., (2010) studied equal channel angular extrusion (ECAE) on Zn-40Al-2Cu-2Si alloy at $250 \text{ }^\circ\text{C}$ for four passes which resulted in an increase in ductility but decrease in strength. They concluded that it was because of grain growth of the alloy that occurred as the processing temperature was sufficiently high. Recovery or recrystallization of the processed alloy had occurred during the processing. This suppressed the improvement in material strength which was supposed to be derived from grain refinement. Ductility of the processed alloy was improved which was due to finer and uniformly dispersed Si or Cu particles in the Zn matrix, which act as an obstacle for crack propagation.

Kawasaki et al., (2010) worked on the microstructural features of Zn-Al alloy processed by HPT. They observed that the initial grain size of $1.4 \mu\text{m}$ reduced to 450 nm at the edge and 600 nm at the center. Hardness value of the processed alloy decreased after one turn.

They confirmed that it was due to decrease in the uniformity in distribution of η precipitates. Earlier these precipitates were in rod shape and occurred inside the matrix of α phase in the annealed condition.

Al-Maharabi et al., (2010) experimented on two-phase ZA alloy for flow response after ECAE at 80-100 °C processing temperature. Results showed that after the first ECAE pass for alloys containing less amount of Al, strength was increased and effect of softening was lesser. They stated that it was due to decomposition of β phase upon cooling which forms mixture of lamellae $\alpha+\eta$ structure. After processing ZA 12 alloy, it contained a higher volume fraction of the fine lamellae structure than ZA 8 alloy. Subsequently, dendritic spacing was smaller in ZA 12. Dendritic spacing is smaller in size resulted in the formation of smaller particles by shearing and scattered more uniformly in eutectic structure. Elongation to failure of 8 pass ECAE processed sample was increased about 100 times as compared to the as cast sample. Higher value of percentage of elongation in the processed sample was due to grain refinement and reduced porosity. In addition, hard α -phase in the matrix was refined and distributed well uniformly. They concluded that the size and dispersion of the α -phase in the eutectic structure were the dominant factors controlling the strength and ductility of the ZA alloy.

Purcek et al., (2008) investigated the influence of ECAE on mechanical properties such as tensile and toughness of Zn-40 wt. % Al alloy. The percentage of elongation to failure increased significantly after four passes, but strength level increased after one pass later onwards it decreased with the higher imposed strain. Results revealed that, as the equivalent strain increased the composition of the phase changes continuously and deformation exhilarated homogenization of the microstructure. The amount of hard Al rich α phase in the matrix decreased with a higher strain owing to dissolution.

Chou et al., (2007) investigated the influence of cross-channel extrusion of Zn-22 wt. % Al eutectoid alloy. From their results it is observed that grain refinement takes place after processing at 100 °C and 200 °C for 10 passes. Microstructure contained lamellar structure in the annealed state, which was transformed into spherical shape after processing. They measured the average grain size of the sample and it was found to be in

the range of 0.3 to 1 μm . The tensile strength of the material decreased as the extrusion passes increased and it decreased with extrusion temperature.

Yeh and Chang, (2002) studied the microstructural features on the forgeability of Zn-based alloys. They carried out study through two types of microstructure viz., one with lamellar structure and the other one with fine grained structure. Their results showed the softening phenomenon in the lamellar structure alloy. Lamellar structure undergoes recovery or recrystallization at early stages as compared to the fine grained structure at elevated temperature. They concluded that fine-grained alloy possesses excellent forgeability than the lamellar structure.

It is clear from the literature that processing should be done at a minimum temperature for much finer grain size, spherical and uniformly spread Al-rich phase. Processed samples showed higher strength during initial passes and in subsequent passes strength decreased with improved ductility.

2.8 Creep

Brief literature studies have been carried out pertaining to the studies on the fundamentals and mechanism of creep.

Creep is defined as the time dependent progressive deformation of the material at constant load and at constant temperature. All metals experience creep if the service temperature of the samples surpasses 0.3-0.5 T_m , where T_m is the absolute melting temperature. The creep rate of the material depends upon many factors such as applied load, operating temperature, material properties and defects present in the material. Creep is a concern of structural engineers and metallurgists when selecting the components that are operating under high stresses or high temperatures.

Creep of metals and alloys is usually determined by a test in which constant load is applied to specimen at a given elevated temperature. As a function of time, the strain is measured. A schematic view of typical creep curve and its distinct features are presented in Figure 2.5.

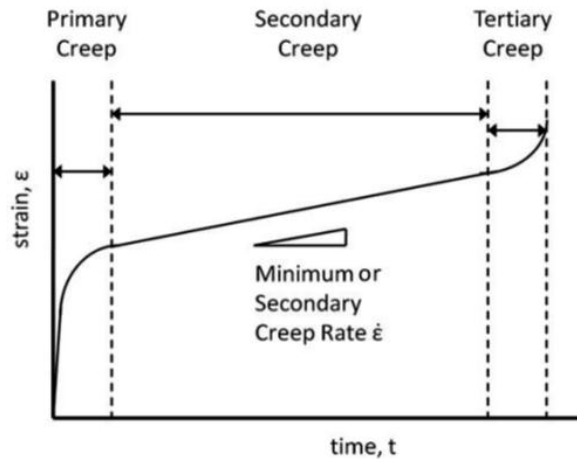


Figure 2.5 Schematic view of typical creep curve.

Impression creep test is a modified form of indentation creep technique. In impression technique, cylindrical flat bottomed punch is used as indenter whereas in the case of indentation creep tests, ball or conical indenter is used. The impression creep method is schematically demonstrated in Figure 2.6.

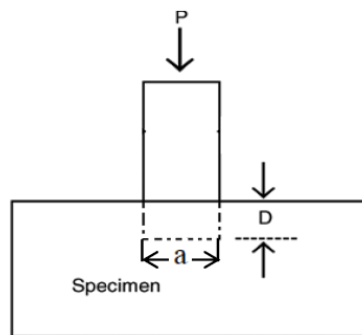


Figure 2.6 Schematic diagram of the indentation creep test (Sastry, 2005).

A cylindrical indenter which is having diameter of 'a' is impressed onto the surface of the sample with applied load (P). The stress in the indenter is called as punching stress and is constant for constant load and indenter diameter. Under this punching stress, the indenter sinks into the material to a depth D in time t. Over a period of time, depth of impression or penetration (D) is examined. Indentation strain is obtained from dividing impression depth (D) by indenter diameter (a) (Li, 2002).

Depending on the application, the punch diameter is varied, typically from a minimum of 0.5 mm diameter to a maximum of 2 mm diameter. The advantage of this elegant test is that very small piece of specimen is enough to assess the creep properties and thereby making it an economical and convenient technique for testing dissimilar weld materials and small sized severe plastic deformed materials. Further, creep properties can also be assessed under predetermined operating conditions. In impression creep test, tertiary stage is absent, which results in much more stable material deformation. Therefore, it is more appropriate to investigate the creep studies of brittle materials (Sastry, 2005).

2.9 Creep Mechanism

The following mechanisms occur during creep deformation of crystalline metals (Cottrell, 1953):

1. Diffusion creep: At low stress, $\sigma/G < 5 \times 10^{-6}$
2. Dislocation creep: At medium stress, $5 \times 10^{-6} < \sigma/G < 10^{-3}$
3. Dislocation glide: At high stress, $\sigma/G > 10^{-3}$
4. Grain boundary sliding

2.9.1 Diffusion Creep

Diffusion creep occurs in materials which involves diffusional mass transport. It becomes the controlling mechanism at high temperatures and at relatively low stresses. Based on the diffusion paths it is broadly classified into two types. They are: (a) Nabarro-Herring creep and (b) Coble creep. If diffusion paths are mainly through the grains and are favored at higher testing temperature, then they are called as Nabarro-Herring creep. Similarly, if diffusion processing paths are carried through the grain boundaries and are favored at lower testing temperatures, they are called as Coble creep.

Nabarro-Herring Creep is one of the forms of diffusion controlled creep. This creep is favored at higher temperature levels and lower stresses resulting in higher vacancy concentration. The creep strain is the ratio of change in the grain dimension to the original grain dimension.

The Nabarro-Herring creep rate equation is given by:

$$\dot{\epsilon}_s = 14\sigma \vec{b}^3 D_v/kTd^2 \quad \text{Equation 2.5}$$

Where, D_v is lattice diffusion coefficient with σ being applied stress at absolute temperature T , \vec{b} is burger vector, d is grain size of the material and k is material constant (Dieter, 1988).

Coble creep is another type of diffusion controlled creep. This type of creep usually occurs by the diffusion of atoms along the grain boundaries in the materials which results in changes in the flow of material by sliding of grain boundaries. The Coble creep rate equation is given by:

$$\dot{\epsilon}_s = 50\sigma \vec{b}^4 D_{gb}/kTd^3 \quad \text{Equation 2.6}$$

Where, D_{gb} is grain boundary diffusion co-efficient. From the above equations, it is clear that creep rate decreases with increasing grain size, but at a different rate for the two mechanisms.

2.9.2 Dislocation Creep

Dislocation creep involves movement of dislocations at relatively lower testing temperatures with higher applied stresses. Dislocation can glide or slide to another slip plane when they encounter obstacles with very little activation energy. Dislocation creep occurs by dislocation glide aided by vacancy diffusion. It involves diffusion of vacancies or interstitials by thermally aided mechanisms during movement of dislocations when they entangle with barriers (Reed-Hill, 2003). Nevertheless, the creep rate is influenced by the movement of dislocations to another slip plane by climb process and involves diffusion and it is a time-dependent process. Generally, climb of dislocation is favored by operating at high temperatures and when they come across defects such as grain boundaries or precipitates can lead to such situations.

2.9.3 Dislocation Glide

In dislocation glide process, plastic deformation takes place by movement of the dislocations by gliding along the slip plane. This is supported by thermal activation at higher applied stress ($\sigma/G > 10^{-2}$) when dislocations are impeded by solute atoms and other dislocations.

2.9.4 Grain Boundary Sliding

If the test temperature of creep is raised approximately to $0.5 T_m$, significant sliding action is observed after the test. At this temperature, the grain boundaries are considered as a source of weakening rather than strengthening (Conrod, 1961).

2.10 Creep Behavior of Zn and Zn-Al Alloy

The creep behavior of Zn alloys have been studied over the years, and most of the published creep data for these alloys are derived from the tensile creep test and/or simple limited extrapolation of experimental creep data.

Thermodynamic data for Zn and Al are shown in Table 2.1. Zn has a lower melting point than Al due to its lower bonding energy and shows lower activation energy for both lattice and boundary diffusion.

Table 2.1 Thermodynamic data for Zn and Al (Frost and Ashby, 1982).

	Zn	Al
Melting point (T_m , °C)	420	660
Lattice diffusion, D_{oL} (m^2/s)	1.3×10^{-5}	17×10^{-5}
Activation energy for lattice diffusion Q (kJ/mol)	92	142
Grain boundary diffusion, D_{oB} (m^2/s)	1.3×10^{-14}	5×10^{-14}
Activation energy for grain boundary diffusion Q (kJ/mol)	61	84

The creep deformation mechanism map for coarse grained polycrystalline pure Zn is reported by Frost and Ashby (1982) and as shown in Figure 2.7. At around room temperature, i.e., $T/T_m = 0.42$ and at normalized stress of 5×10^{-4} for coarse grained pure Zn, the creep rate was in the order of 1×10^{-8} and found to exhibit power law creep.

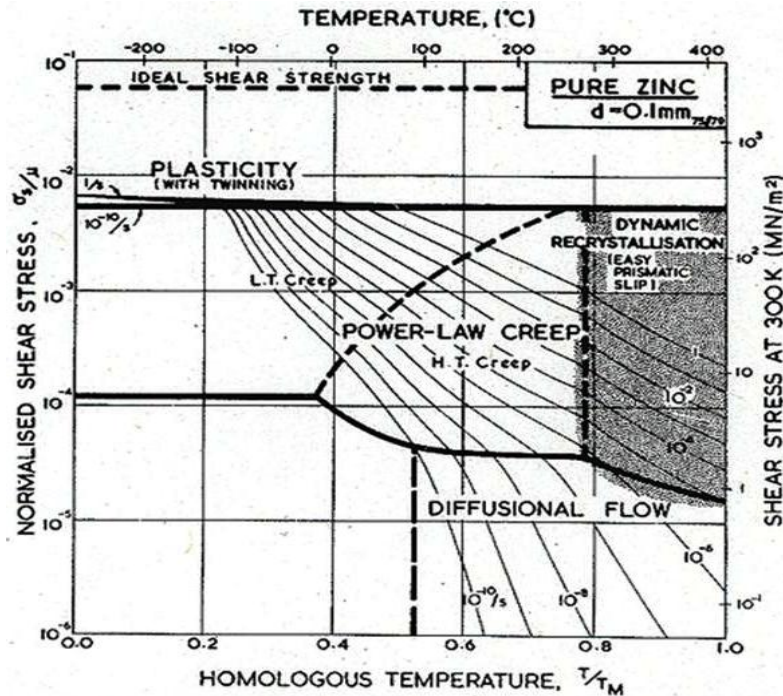


Figure 2.7 Creep deformation mechanism map for coarse pure Zn (Frost and Ashby, 1982).

The summary of creep data on Zn and its alloys is given in Table 2.2. ILZRO 16 alloy (Zn-1 wt. % Cu-0.2 wt. % Ti-0.15 wt. % Cr) exhibits several orders of magnitude of lower creep rate compared to the most commonly used zinc alloy 3 (Zn-3.5 wt. % Al-0.25 wt. % Cu) even at significantly higher testing temperatures as shown in Table 2.2. Alloy with minimum creep rate of 5×10^{-8} at elevated temperature of $T/T_m = 0.6$ with normalized stress of 3×10^{-4} was developed by Turk et al., (2007) by adding 0.5 wt. % of Mn to ZA-8 alloy which had creep rate of 14×10^{-8} at same operating conditions. This shows an improvement in creep resistance for Mn containing ZA-8 alloy as compared to the one without Mn. Zn-Al binary alloys possess low resistance to creep due to their

superplastic characteristics. Hence, these alloys have limited commercial applications (Mir, 1998). In order to improve their creep strength, the addition of alloying elements to Zn-Al alloys has been studied. Naziri and Pearce (1970) investigated the effect of Cu up to 1 wt. % addition on creep properties of hyper-eutectoid Zn-20Al alloys. They observed that the creep resistance of the alloy improved continuously at room temperature, but did not have a significant effect above 150 °C. Murphy et al., (2013), and Savaskan and Murphy (1983) investigated the creep behavior of one eutectoid and two nearly eutectoid Zn-Al alloys containing 3 and 4 wt. % Cu. They observed that creep resistance of these alloys was higher than the binary alloys. In the as-received condition, the alloy with 4 wt. % Cu exhibited a lower creep rate than 3 wt. % Cu alloy. These observed results were reversed for the heat treated condition for same alloy. It was due to the overall Cu content which increased the creep resistance of as-cast alloys as it was not uniformly distributed and fine particles were segregated along the grain and grain boundaries. In the case of heat treated alloys, creep resistance was decreased due to the incomplete dissolution of Cu precipitates into the Zn-Al matrix.

Table 2.2 Summary of creep data for various Zn-Al alloy (Porter, 1991).

Alloy	Grain size	T/T_m	σ/E	ε̇, min⁻¹
Pure Zn	Coarse	0.42	5x10 ⁻⁴	1x10 ⁻⁸
Zinc alloy 3	Coarse	0.46	5x10 ⁻⁴	2x10 ⁻⁸
ILZRO 16	Coarse	0.55	5x10 ⁻⁴	8x10 ⁻¹¹
Zn-4.5 Al	Ultra-fine	0.44	5x10 ⁻⁴	2x10 ⁻⁸

Creep behavior of nano-crystalline or ultrafine materials presents several complications when compared to conventional coarse grain materials. This is because the volume fraction of grain boundaries is more in the case of ultrafine materials. Nano-crystalline/ultrafine grain microstructures are inherently unstable; this restricts them to be studied at low homologous temperatures. Since the grain boundaries represent a large volume fraction and path for diffusion in comparison to crystalline lattice, it is most often

found that diffusion creep will dominate the deformation over a wider range of conditions of stress and temperatures in comparison to conventional coarse grain size materials (Gobien et al., 2010).

2.11 Wear

Wear behavior of severe plastic deformed material is important for more practical usage and industrial applications. In this regard, fundamentals of wear and its effects on wear characteristics of SPD processed materials were studied and presented.

Wear is the progressive damage which occurs when two contacting surfaces slide over each other. Simple theory for describing the severity of wear is proposed by Archard and it is given by (Archard, 1953)

$$W = K \frac{SL}{H} \quad \text{Equation 2.7}$$

Where, W is the volume loss (m^3), K is the dimensionless wear co-efficient, S is the total sliding distance (m), L is the applied load (N) and H is the hardness of the pin.

2.12 Wear Mechanism

During sliding, materials may show different wear behavior under different sliding conditions. Depending on the different sliding conditions, different wear mechanisms have been proposed which include (i) Adhesive wear, (ii) Abrasive wear, (iii) Corrosive wear, (iv) Erosive wear and (v) Delamination wear. In practice, more than one wear mechanisms may operate with the interaction of two bodies (Ashby and Lim, 1990).

2.12.1 Adhesive Wear

Adhesive type of wear mechanism occurs when two flat surfaces are in contact during sliding which involves the detachment of flakes or debris and attachment to the counter surface. No matter how perfectly the pin and disc surfaces are prepared, hills and valleys (high spots) will be present on both the surfaces. Initially, point contact of asperities leads to an extremely high contact pressure (Archard, 1953). These high spots have a tendency to stick to each other and upper layer of the softer material is

dragged away during sliding, this phenomenon is called material transfer. The transferred debris may directly drop off and cause mass loss or transfer back to the soft surface.

2.12.2 Abrasive Wear

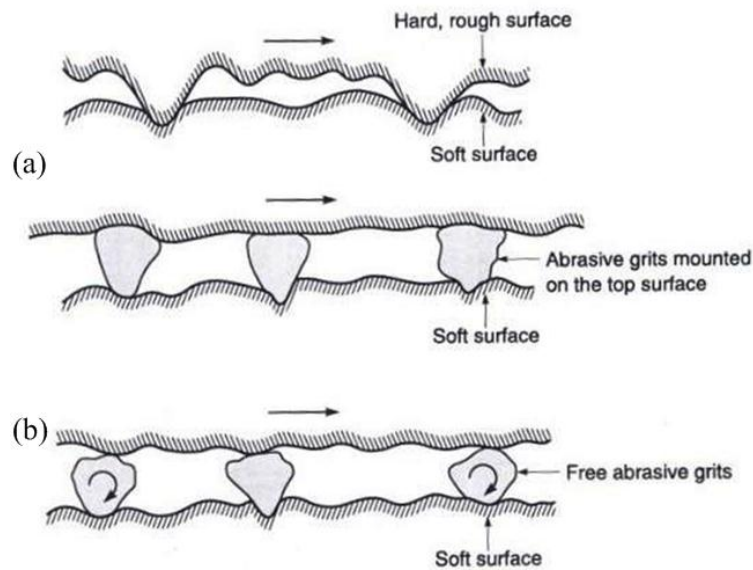


Figure 2.8 Illustration of (a) two body abrasive wear and (b) three body abrasive wear (Bhushan, 2002).

Abrasive wear is supposed to occur on a soft material surface when asperities of rigid and hard particles plough through it. Abrasive wear also occurs in the case of sliding between two similar materials if hard particles are formed through debris in between them during operation. There are two situations of abrasive wear, two-body abrasion as shown in Figure 2.8 (a) and three-body abrasion as illustrated in Figure 2.8 (b) (Bhushan, 2002). Generally, two body abrasion shows lesser wear rate as compared to three body abrasion. Typically, abrasive wear leaves sequences of grooves parallel to the sliding direction. Abrasive wear is divided into three modes depending on severity of contact such as ploughing mode, wedge forming mode and cutting mode. In the ploughing mode, ridges form along the sides of the grooves and not many wear particles are formed. In the wedge forming mode, the hard tip pushes the soft material and forms a wedge and the wedge will detach off when the soft material reaches its plastic limit. Cutting mode is

more like chip formation mode in which large chips of the soft material are removed when the attack angle is large (Hokkirigawa and Kato, 1988).

2.12.3 Corrosive Wear

Corrosive wear involves the removal of chemical layer on top of the material during sliding the process. The most common corrosive wear is oxidation dominated wear which happens when materials are sliding in the oxidizing or moisture environment. Corrosive wear involves two stages: formation of chemical layer and rubbing. Sometimes, the real situation may be more complicated as the worn surface has no time to be re-corrosive before rubbing off. After corrosion, the real contact normally changes from metal-metal contact to film-film contact, which changes the whole wear process (Giourntas et al, 2015).

2.12.4 Fretting Wear

Fretting wear occurs when there is cyclic motion with very small amplitude between two surfaces. Wear debris is produced by a combination of adhesion between asperities and the crack nucleation. Fretting wear happens when machines are subjected to vibration. Wear debris between the contacting surfaces were formed by adhesive process and it was believed to be dominating in the initial process (Stowers and Rabinowicz, 1973). Additional fretting cycles introduce more wear debris by plastic deformation which results in formation of micro cracks. These cracks grow and propagation of cracks to surface leads to additional debris.

2.12.5 Erosive Wear

Erosion involves generation of wear debris and the debris or particles strike the surface of material with a high speed which results in more damage and material loss. Erosive wear is classified into three types: cavitation erosion, solid particle erosion and liquid impingement erosion. Cavitation erosion occurs for materials which are in direct contact with liquid and it is in comparative motion. Froths or lathers in the fluid explode as temperature is increased or pressure is dropped, in contrary to the inner

surface of the containers that forms cavitation erosion on the surface. High energy particles impacted onto the surface of the material cause solid particle erosion. Wear debris is formed as a result of repeated impact. When a solid surface is struck by small liquid drops at high speed (more than 300 m/s), it will result in damage to the solid surface, it is termed as liquid impingement (Prozhega et al., 2014).

2.12.6 Delamination Wear

When a hard rough surface is sliding repeatedly on a softer component under a high load the protective residual stresses may be developed in the subsurface of the softer material and form a thin work hardened layer. This work hardened region improves the shear strength of the material. After thousands to millions of loading cycles, much more deformation is introduced to the surface region. For brittle materials, micro cracks are formed in the subsurface of material and grow parallel or at an angle to the surface; for ductile materials, it is more likely that ductile failure results from an accumulation of plastic strain close to the contact surface. The wear debris in the form of thin sheet is formed leading to the introduction of delamination wear (Suh et al., 1973).

2.13 Wear Studies on SPD Processed Materials

Severe plastic deformed (SPD) materials possess higher strength than their coarse grain structure. It is attributed to the finer grain size and strain hardening. It is anticipated that fine grain structured materials have better wear resistance. However, earlier investigations made on the wear behavior of severe plastic deformed materials revealed contradictory results. Hence, overview of the latest progress in the wear behavior of SPD processed materials is important to be reviewed.

Gao et al., (2008) carried out preliminary wear test on the equal channel angular pressing (ECAP) of aluminum bronze alloys. More homogeneously distributed second phase particles were observed in the material after six ECAP passes. They observed that the coefficient of friction of ECAP processed alloys decreased continuously with increasing

applied load. The wear rate of ECAP processed samples increased as compared to the unprocessed samples.

Another wear study by Kucukomeroglu (2010) on the ECAP processed Al-12 wt. % Si alloy indicated higher mass loss with increasing applied load. The wear resistance of the as-cast alloy was better when compared to ECAP processed alloy for six numbers of passes particularly for higher applied load and longer sliding distance. Further, they carried microstructural characterization on both the as-cast and ECAP processed samples which revealed that wear surfaces of both samples contain thick oxide layers. They concluded that the observed oxide layers were formed by the tribo-chemical reactions which played a significant role in wear behavior of the material. Furthermore, ECAP processed sample surface oxidized more rapidly as compared to the as-cast samples. This oxidation process reduced the effect of strengthening acquired by the grain refinement on the wear resistance.

Wang et al., (2011) carried dry sliding wear tests on as-received and ECAP processed Al 1050 alloy. Initially, they observed that average grain size of the as-received material was in the range of 44 μm and reduced to 1.3 μm by deforming through ECAP process up to eight passes. Microhardness of the ECAP processed material is higher than the as-received material and it increased continuously with increasing number of passes. Coefficient of friction of the both materials remains almost the same, but wear mass loss is higher in the case of ECAP processed samples.

Wear behavior of ECAP processed Al sample with addition of different amount of Cu was studied by Aal et al., (2010). This study shows that wear mass loss of ECAP processed sample reduced with increasing number of ECAP passes and wear mass loss was more affected by sliding distance followed by applied load. Hardness of the processed alloy showed improvement over the as-cast alloy. It is concluded that fine dispersion of Cu and refined grain structure improved the wear resistance of the processed alloy.

Similar type of wear study was experimented on Al samples processed by ECAP at room temperature containing small amounts of Mg and Si by Ortiz et al., (2011). The wear resistance of the processed alloy improved and they concluded that mass loss mainly depends upon the equivalent strain imposed and correspondingly on the microstructural features.

2.14 Taguchi Method

Taguchi method is used to determine the optimum values for the parameters of the process. When the process is more complex, fewer experiments are required to characterize in Taguchi method than usually required by the traditional methods.

Genichi Taguchi developed this approach in the 1950s and 1960s for attaining high quality products and his methods were practically used at Ina Tile Company in late 1950s (Phadke and Madhav, 1989). This method was initiated to control the quality of the product or process. According to Taguchi, the term quality is defined as “It is the loss incurred by the society from the time a product is shipped.” In this method, discrepancies associated with the sources are called as noise factors. Noise factors are divided into three types: (a) variations in the environment, called external noise, (b) variations involved in the manufacturing process, called unit to unit noise and (c) variations in the performance of the product, called deterioration noise (Suh, 1990). Input signals to a product or process are provided from these noise factors and output signals are referred as response of a product or process.

There are three different approaches in Taguchi technique: (a) system/concept design, (b) parameter design and (c) tolerance design. Generally, complete structure has to be designed in the case of system design, whereas in parameter design only the components associated with the system have to be designed. In tolerance design, acceptable variables linked with the particular components need to be designed for obtaining optimal results or to minimize the quality loss. Among the three approaches parameter design is the ideal one, since robust designs is achieved easily with low costs. In the case of system design, requires substantial advancements in the entire system that may or may not lead to

desired circumstances and it is a lengthy process. Tolerance design comprises supplementary cost to the developed process. Parameter design is the most convenient approach for optimizing the parameters associated with component quality evaluation. The steps for using Taguchi's method of parameter design are classified into three groups: (a) experimental planning, (b) conducting the experiment and (c) analyzing the data. The details of Taguchi method are given in Montgomery (2008). It is summarized as below:

(a) Experimental planning

- Defining the objective function.
- Selection of the factors to be evaluated.
- Selection of number of levels.
- Selection of appropriate orthogonal arrays by applying following condition: Degree of Freedom (DOF) of Orthogonal Array (OA) \geq Total Degree of freedom of factors and Interactions.
- Assignment of factors into the columns.

(b) Conducting the experiment

- Carrying out the experiment according to the generated table.

(c) Analyzing the results

- Determining the optimum parameters, analyze the acquired results.
- Conducting the confirmation test for validating the optimum parameters.

Orthogonal array (OA) selection for conducting the experiment is carried out by considering degree of freedom (DOF) of parameters.

- DOF of control factors is: Level - 1
- DOF of OA = Number of trials - 1

Let us consider three parameters of the experiment; each parameter is having three levels. Then, DOF of each parameter is two ($3-1=2$). Hence total degrees of freedom of three parameters are six. Taguchi method uses the term signal-to-noise (S/N) ratio for

evaluating quality characteristics. In S/N ratio, multiple data points are condensed to give the best performance of the process variables. Depending on the type of characteristics being estimated S/N ratio is divided into three groups. There are three S/N ratio characteristics: (a) Lower-the-better (b) Higher-the-better (c) Nominal-the-better. One of these characteristics will be selected based on the response function.

For reducing the performance characteristics, S/N ratio is calculated by using,

$$\frac{S}{N} = -10 \log 1/n \sum_{i=1}^n (y_i^2) \quad \text{Equation 2.8}$$

The term signal represents the desirable value for the output characteristics and the other term noise represents the undesirable value which are expensive to control or difficult to maintain such as humidity in wear experiment. The aim of any experiment is always to determine the highest possible S/N ratio for the result. A high value of S/N implies that the signal is much higher than the random effects of the noise factors or minimum variance. Therefore, the optimal level of the process parameters is the level with the greatest S/N ratio. The influence of control parameters such as (i) applied load, (ii) sliding distance and (iii) sliding speed in wear tests were evaluated using the response table for S/N ratio which shows the average of selected characteristics. Ranking of parameters were based on the delta statistics by comparing the relative value of the effects. Delta is the difference between the maximum and minimum mean response across the levels of a factor. S/N ratio is a response which combines iterations and the effects of noise levels into single optimum points.

Any experiment using Taguchi method is usually carried out by generating the orthogonal array. It gives the reduced variance for the experiments giving optimum setting of control parameters. For example, consider an orthogonal array (L_9) as shown in Table 2.3 which contains three control factors, namely, applied load, sliding distance and sliding speed with three levels that will be collective to form nine trails.

It is observed that by using orthogonal array only nine trials are required to carry out the wear experiment which is having three factors and varied for three levels when it comes

to the traditional way of testing it would have been $3^3 = 27$ trials. In the case of L_9 orthogonal array, control factors are assumed to be independent variables. In some cases, it is necessary to consider the interactions between the control factors and larger orthogonal array is essential for finding the effect of interactions.

Table 2.3 Taguchi's L_9 orthogonal array.

	Factors		
Trial	Applied load (A)	Sliding distance (B)	Sliding speed (C)
1	1	1	1
2	1	2	2
3	1	3	3
4	2	1	2
5	2	2	3
6	2	3	1
7	3	1	3
8	3	2	1
9	3	3	2

2.15 Taguchi's Approach on Wear Behavior

The use of Taguchi's method on dry sliding wear behavior of Al and its alloys was studied and it is presented below.

Basavarajappa and Chandramohan (2005) studied wear behavior on Al-Cu-Mg matrix composites using the Taguchi approach. They observed that wear rate is highly affected by sliding distance on the composites. Analysis of variance and multiple regression value shows satisfactory correlation with experimental results.

Taguchi approach was used for optimization of friction stir welding (FSW) parameter in polyethylene by Rezgui et al., (2010). The experimental tests were conducted using L_{27} orthogonal array for different control factors such as pin diameter, rotation and welding

speed and holding time. They observed that the results were matched with the experimental values and numerically analyzed values with a confidence level of 95 %.

Baskaran et al., (2014) investigated on metal matrix composite of Al 7075 alloy with 4 to 8 wt. % TiC as reinforcement for optimizing the effect of reinforcement on wear behavior using Taguchi L_{27} orthogonal array experimental design. Results presented from this method gave the optimum blend for minimum wear rate of 4 wt. % of TiC. Using analysis of variance (ANOVA) significant contributing factors for higher wear rates were noticed. The optimal condition obtained from the analysis was applied load of 9.81 N, sliding distance of 1500 m and sliding speed of 3 m/s. Confirmatory test results were associated with minimum error.

Therefore, it is observed from the above literature that Taguchi technique can be used effectively to optimize the parameters in order to obtain a minimum wear rate.

CHAPTER 3

EXPERIMENTAL PROCEDURES

In this chapter, experimental details related to multi directional forging (MDF) process of Zn-24Al-2Cu alloy combined with heat treatment are explained. Microstructural characterization and assessment of mechanical properties of solutionized and processed materials are briefly outlined in the following sections.

3.1 Material

The present research was conducted on Zinc based material (ZA 24 alloy). Material was procured from Asppice Engineering, Coimbatore, India. The chemical composition of this material was confirmed by atomic absorption spectroscopy and shown in Table 3.1. The as-cast material was used in the form of billets. The rectangular specimens of dimension 55 mm x 55 mm x 45 mm were machined from the billets. These rectangular specimens were homogenized for 5 hours at 365 °C by using electrical resistance muffle furnace and quenched in water at room temperature. Homogenization temperature was selected from binary phase diagram of Zn-Al alloy which is presented in Figure 2.2. This phase diagram reveals that for binary Zn-Al alloy single phase called β exists at above 365 °C temperature. The average grain size of as-quenched solutionized material was found to be 30 μm determined by linear intercept method. Solutionized materials were subjected to multi directional forging (MDF) process at 30, 100 and 200 °C temperatures.

Table 3.1 Chemical composition of the Zn alloy used in the present work.

Elements	Al	Cu	Fe	Mg	Zn
Weight percentage	24.4	2.55	0.38	0.02	Balance

Figure 3.1 shows energy dispersive X-Ray images of as-cast Zn-Al alloy. The elemental composition of the procured Zn-Al alloy was tested by using the energy dispersive X-Ray analysis (EDAX).

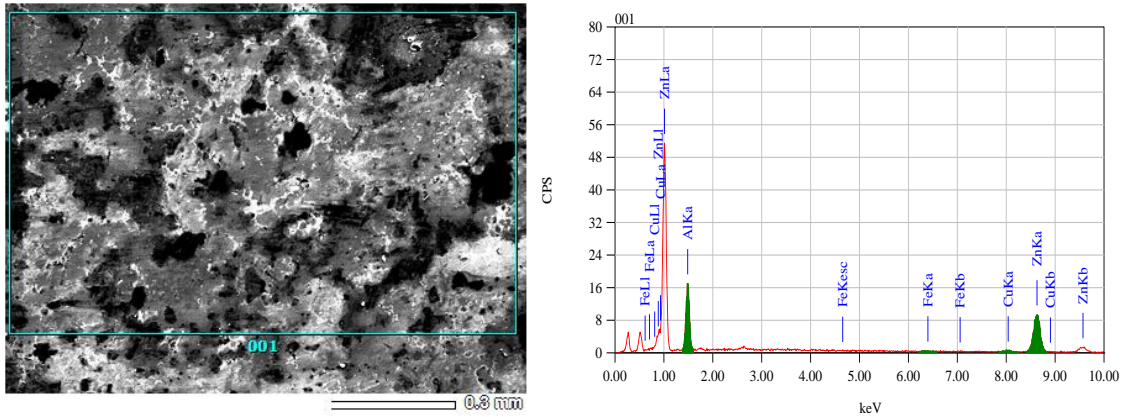


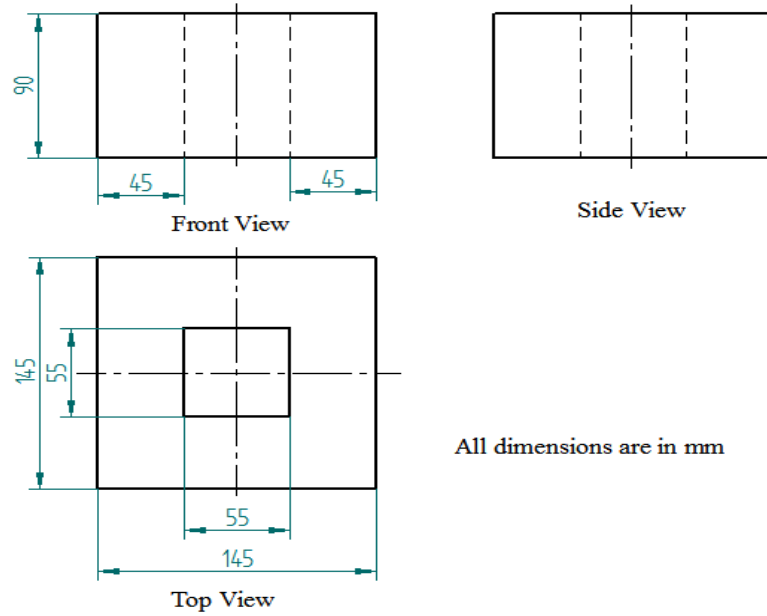
Figure 3.1 EDAX analysis of as-received Zn-Al alloy.

3.2 Multi Directional Forging

Grain refinement is the primary objective of this study and further understanding of the mechanical properties of refined Zn-24Al-2Cu alloy are studied. Figures 3.2 (a) and (b) show the two dimensional diagram of multi directional forging (MDF) die and base plate design along with dimensions. Figure 3.3 shows the schematic three dimensional diagram of the MDF die design which was used to refine grains of Zn-24Al-2Cu alloy. The MDF die was fabricated using H11 tool steel having chemical composition: C: 0.4, Cr: 5, Mn: 0.3, Mo: 1.3, Si 1, V: 0.5, Fe: 91.5 (wt. %). The die assembly consists of two split sections with channeling on the bottom base plate, which were assembled with pair of M12 bolts and nuts. The photograph of the die assembly is shown in Figure 3.4.

The solutionized samples were preheated and processed by MDF at room temperature, 100 °C and 200 °C in the designated split type die. The material was processed up to three passes at 100 °C and six passes at 200 °C with constant pressing speed of 0.4 mm/s using a 200 ton hydraulic press. The photograph of the hydraulic press is shown in Figure 3.5.

(a) 2D representation of MDF die



(b) 2D representation of base plate

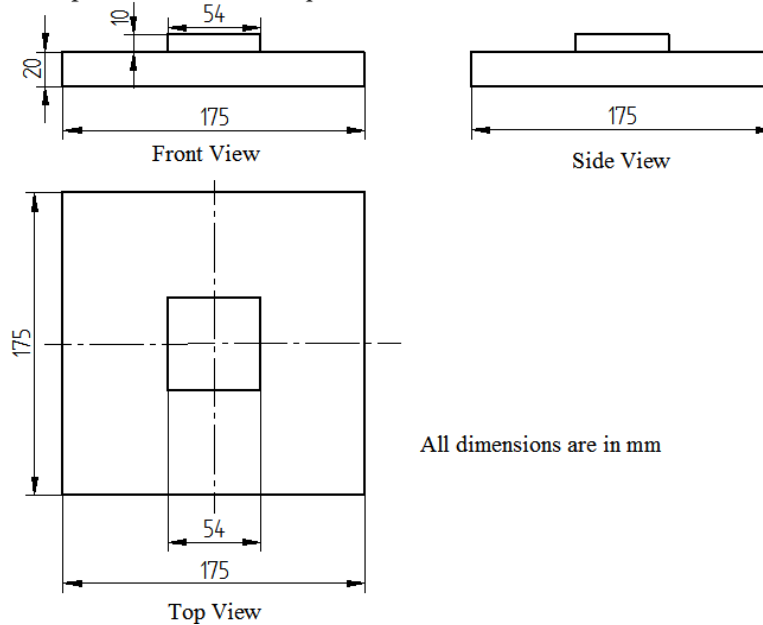


Figure 3.2 Two dimensional representations of (a) MDF die and (b) base plate.

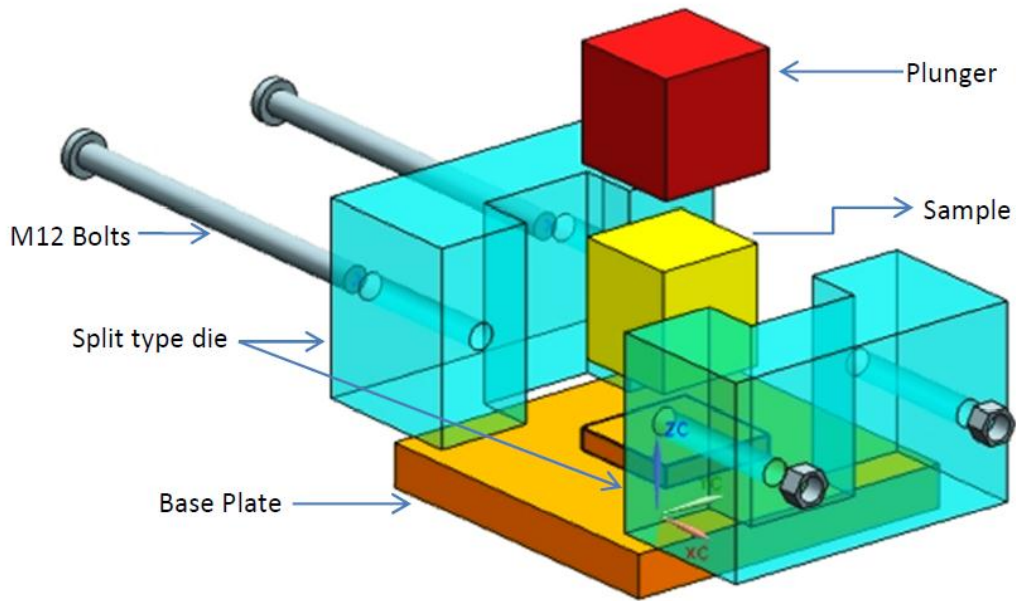


Figure 3.3 Schematic three dimensional representation of the MDF split type die with plunger.

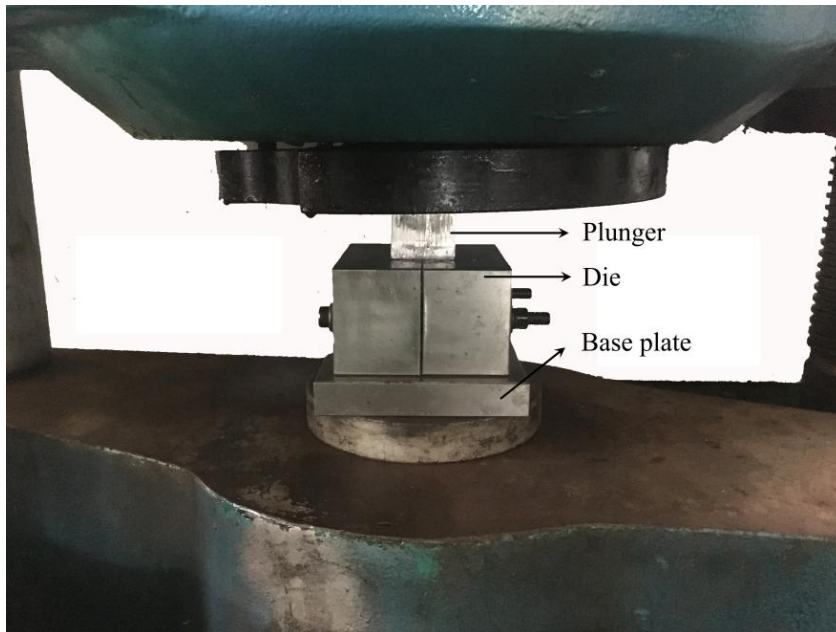


Figure 3.4 Photograph of multi directional forging die assembly.



Figure 3.5 Photograph of the 200 ton hydraulic press.

During the MDF process, samples were heated for 30 minutes in the furnace to the desired temperature. At first pass, the sample was inserted into the die and was forced downwards by pressing to an equivalent strain of 0.2.

Equivalent strain is determined according to the equation:

$$\epsilon_e = \ln \frac{h_o}{h_f} \quad \text{Equation 3.1}$$

Where, h_0 and h_f are initial and final height of the sample. Subsequently, reheating and processing for another pass was carried out by rotating the sample by 90° over the horizontal axis and pressing to the same strain as in previous passes. It is schematically shown in Figure 2.1. MoS_2 lubricant was used to reduce the friction between the die and specimen contact areas during processing. The total equivalent strain of 0.6 was applied in three passes at 100°C and 1.2 in case of six passes at 200°C .

Workpiece was plastically deformed by plane strain condition. Samples processed by MDF at room temperature, 100°C and 200°C are shown in Figure 3.6.

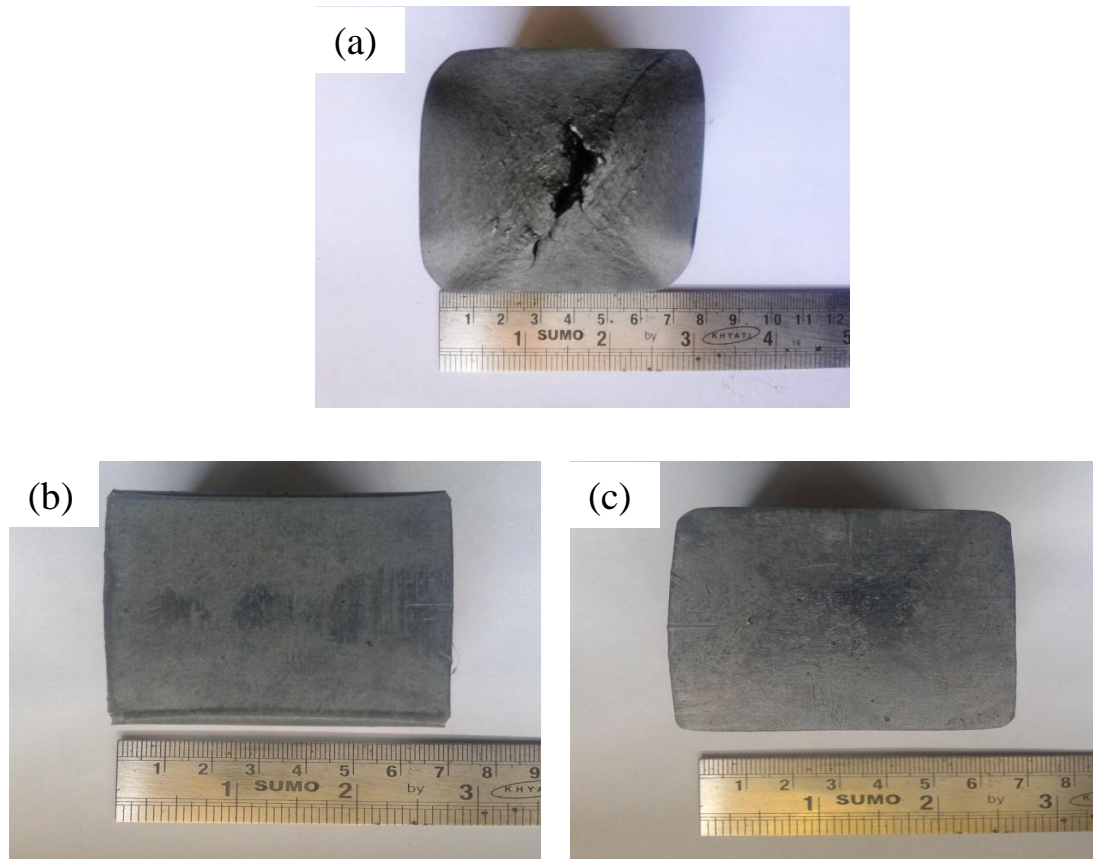


Figure 3.6 Zn-24Al-2Cu alloys after MDF processing at (a) room temperature, (b) 100 °C up to three passes and (c) 200 °C up to six passes.

3.3 Precipitation Hardening

Precipitation hardening heat treatment was carried out on the solutionized and water quenched coupons of size 10 mm x 10 mm x 15 mm. Solutionized coupons were aged at 100, 150, 200 and 250 °C for 0.5-24 hours and aging profiles were generated. From these profiles aging temperature and aging time were noted to derive the condition for highest hardness. Accordingly, MDF processed samples were given an aging treatment at 100 °C for one hour.

3.4 Microstructural Analysis

The specimens for microstructural analysis were taken from the central part of the sample parallel to the last forging axis.

3.4.1 X-Ray Diffractometry

The X-Ray diffraction (XRD) profile was generated using a computer controlled diffractometer (Make JEOL, Model-JDX 8P, Japan) with Ni filter operated at 30 kV and 20 mA with a Cu- α radiation with diffraction angle (2θ) range from 30° to 90° and at scanning speed of 1° per minute. From the literature, it was found that major peaks of the phases for Zn-Al alloy system is obtained within the above mentioned diffraction angle range from 30° to 90° (Zhu, 2004).

3.4.2 Optical Microscopy

A metallurgical microscope was used to observe the microstructure of materials under investigation before and after MDF process and also on the combined aging heat treatment with MDF processed sample. A conventional metallographic technique was used for the preparation of samples. The specimens were polished using sequence of silicon carbide (SiC) abrasive papers and alumina paste on cloth. Specimens were chemically etched using 3 % Nital (3 ml of Nitric acid with 97 ml of ethanol) for microstructural study.

3.4.3 Scanning Electron Microscopy

The microstructures of all the solutionized, MDF processed and MDF combined with post-aged samples were examined in a scanning electron microscope (Make JEOL, Model- JSM-6380LA). The energy dispersive spectroscopy or energy dispersive X-Ray spectroscopy (EDS/EDAX) analysis was used in the present work for additional qualitative and quantitative elemental composition.

3.4.4 Transmission Electron Microscopy

The refined grain structures in the MDF processed samples and MDF combined with post-aged samples were observed using transmission electron microscopy (TEM). The TEM specimens were prepared by the following procedures: (a) by metallographic polishing a thin slices of approximately 100 μm from the processed samples (b) 3 mm diameter discs were punched from those thinned slices (c) by using disc polishing, thickness of disc is further reduced to approximately 60 – 80 μm (d) dimpling were carried out on the thin disc upto 20 μm (e) dimpled specimens were subjected to ion milling with a beam angle of 6° operated at 5 keV until perforation (f) finally, milling operation was carried on perforated specimens with a beam angle of 3° at 2.5 keV. The thin foils were examined in a TEM microscope (Make JEOL, Model- JEM-2100).

3.5 Mechanical Property Evaluation

To assess the properties of the Zn-24Al-2Cu material following mechanical tests such as (i) hardness test, (ii) tensile test, (iii) compression test, (iv) creep test and (v) dry sliding wear test were conducted on (i) solutionized samples, (ii) aged samples, (iii) MDF processed samples and (iv) post-aging of MDF processed samples.

3.5.1 Hardness Measurement

Hardness of the sample was measured with the help of Zwick Vickers hardness tester. Vickers micro hardness measurements were carried out on solutionized and aged samples at room temperature under load of 1.961 N and dwell time of 20 seconds. The MDF samples were partitioned using an abrasive cutter and polished using a belt grinder. The conventional metallographic technique was used to get the flat surface. Hardness measurements were carried out in the plane perpendicular to the axis of the final MDF forged samples. Rockwell hardness was measured for MDF processed and post-aging of MDF samples under load of 588.4 N and dwell time of 30 s. According to ASTM E18, Rockwell scale of H is used in Zinc alloy.

3.5.2 Tensile Test

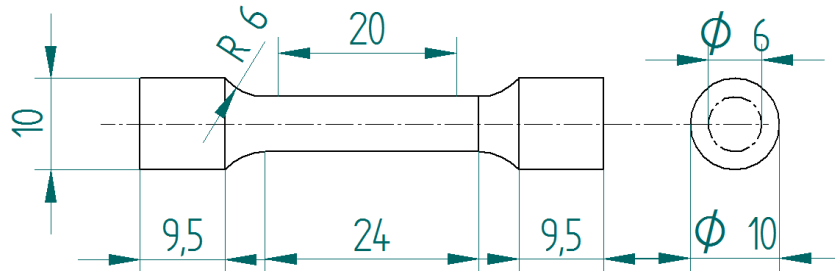


Figure 3.7 Schematic diagram of tensile test specimens in accordance with ASTM E-8 standard (all dimensions are in mm).



Figure 3.8 Photograph of tensile test specimen.

Tensile tests were carried out for solutionized, aged and MDF processed combined with post-aging samples. The specimens after MDF were machined into tensile specimens as per the ASTM E-8 standards. The dimension of the tensile specimens used in the present work is shown in Figure 3.7. Photograph of tensile specimen prepared from MDF processed sample is shown in Figure 3.8. MDF coupons were machined to cylindrical specimens with gauge length of 24 mm, gauge diameter of 6 mm and 55 mm as total length. Tensile testing was carried out using a Shimadzu AG-X plus™ with a capacity of 100 kN universal testing machine. Tests were conducted at room temperature at a strain rate of 0.05 1/s. Three specimens were tested to confirm the repeatability of the

results. The stress-strain curves obtained during each test were used to estimate tensile strength, whereas the percentage of elongation was estimated by measuring the dimensions of the samples before and after fracture.

3.5.3 Compression Test

Compression tests were conducted in order to determine the flow curve, strength coefficient and strain hardening exponent according to the ASTM standard E9-09. The dimension of the compression specimens used in the present work is shown in Figure 3.9. Shimadzu AG-X plus™ with a capacity of 100 kN universal testing machine was used. The cylindrical specimens of length to diameter ratio 1.25 were prepared from the unprocessed and MDF processed sample. Tests were conducted at room temperature at an average strain rate of 0.5 mm/ min. Three specimens were tested using MoS₂ as a lubricant. From the true stress (σ) and true strain (ϵ) curve material properties such as strength coefficient (K) and strain hardening exponent (n) were calculated by fitting the curve to Hollomon equation. It is described as given below,

$$\sigma = K \epsilon^n \quad \text{Equation 3.2}$$

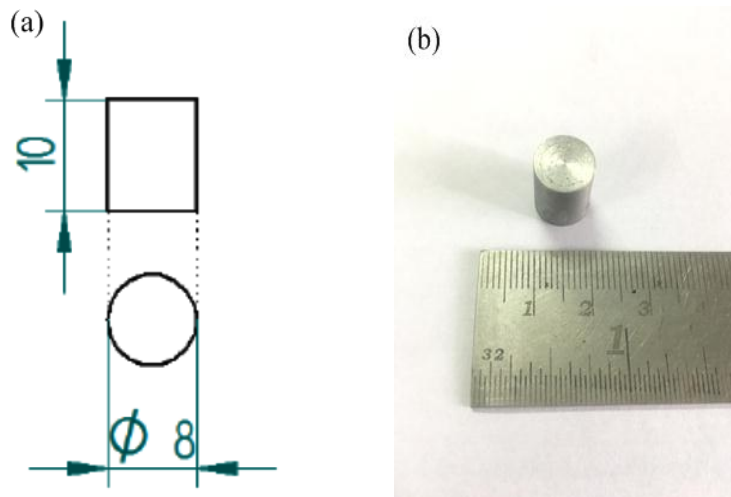


Figure 3.9 Compression test specimens in accordance with ASTM E9-09 standard (a) schematic view and (b) photographic image (all dimensions are in mm).

3.5.4 Impression Creep Test

Impression creep test is the most suitable for testing small sized samples. It enables to suggest creep mechanism interrelated with the microstructures of the material. By using a single specimen, temperature and stress dependence of the creep rate can be attained.

Impression creep test apparatus used for conducting the test is schematically presented in Figure 3.10. The cage arrangements are displayed in Figure 3.11, where the sample is mounted on the bottom of the cage which is movable and another cage is fixed where indenter is attached. Bottom cage is connected to the vertical rod. This rod is made of Nimonic 90 alloy having a chemical composition of 19 % Cr, 17 % Co, 2.5 % Ti, 1.5 % Al and balance Ni (wt. %). It is connected to the level arm. Weight is added to the other side of the lever arm. The sample presses against the indenter which is fixed to the top part of the cage and is loaded vertically downward. Indenter is made of tungsten carbide having circular indenting surface. Schematic diagram of the indenter and its dimensions are shown in Figure 3.12. Lever arm magnifies the load on the sample surface by 5.5 times. Hollow cylindrical electric furnace is used for maintaining the sample temperature. Variations in the temperature are maintained within the range of ± 5 °C using electronic controller. Linear variable differential transformer (LVDT) is used for measuring the depth of indentation with an accuracy of one micrometer.

The impression creep tests are carried out at 30, 50, 100 and 150 °C temperature levels with constant load of 2 kg and 2.5 kg carried up to 5600 s for MDF processed and solutionized samples. Depth of indentation divided by the indenter diameter gives the indentation strain values. Steady state creep rate (SSCR) is obtained by finding the slope of the curve at the secondary creep stage. Figure 3.13 displays the schematic creep curve for indentation strain versus time.

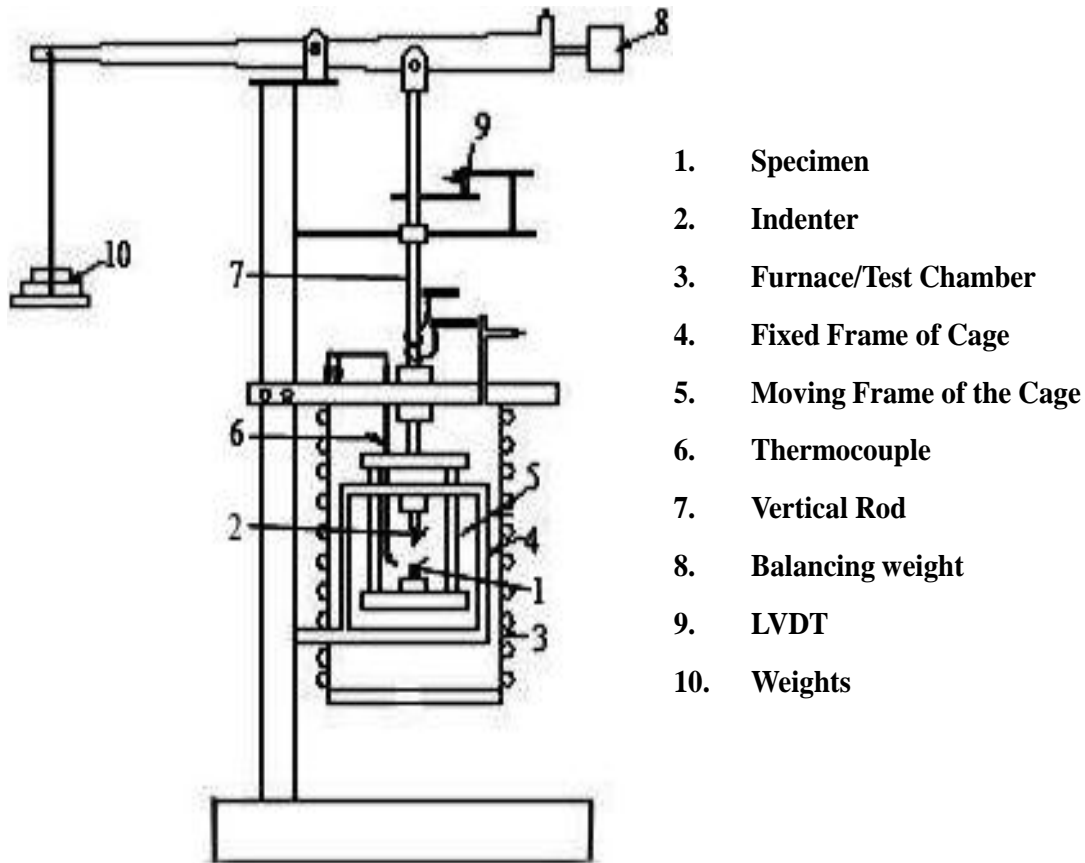


Figure 3.10 Apparatus used for the impression creep test.

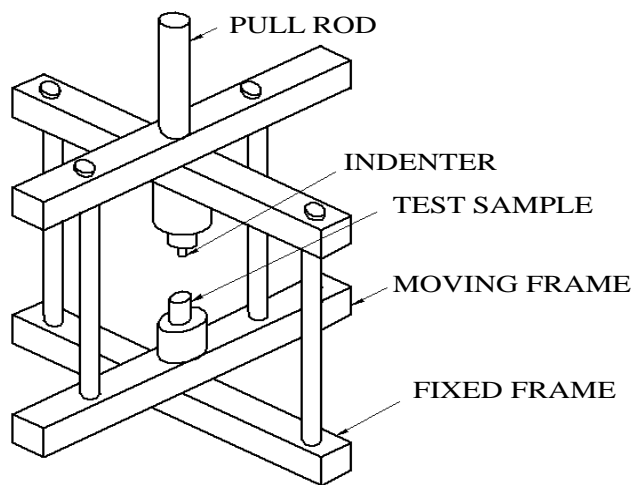


Figure 3.11 Split cage used in the impression creep test.

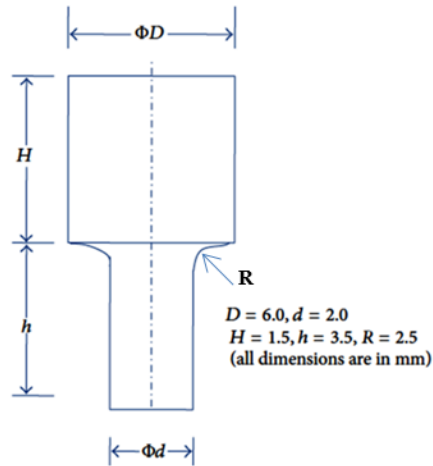


Figure 3.12 Indenter used in the impression creep test.

Using the creep profile, values of the stress exponent (n) and apparent activation energy (Q_a) can be determined.

Stress exponent (n): If creep tests are conducted at two different loads at the same temperature, assuming the relation

$$\dot{\epsilon} = k\sigma^n \quad \text{Equation 3.3}$$

Where creep rate $\dot{\epsilon}$ and stress σ and n being the stress exponent of creep, the same can be evaluated using the relation,

$$n = \frac{\log\left(\frac{\dot{\epsilon}_2}{\dot{\epsilon}_1}\right)}{\log\left(\frac{\sigma_2}{\sigma_1}\right)} \quad \text{Equation 3.4}$$

Apparent activation energy (Q_a): The apparent activation energy is obtained by using

$$\dot{\epsilon} = A \exp\left(\frac{-Q_a}{RT}\right) \quad \text{Equation 3.5}$$

Where A = constant, Q_a = activation energy (kJ/mol), R = universal gas constant, T = absolute temperature (K).

$$\ln \dot{\epsilon} = \left(\frac{-Q_a}{R}\right)\left(\frac{1}{T}\right) + \ln A \quad \text{Equation 3.6}$$

The apparent activation energy is calculated by plotting strain rate ($\dot{\epsilon}$) versus ($1/T$) using a semi-logarithmic scales at different stresses. The activation energy is obtained from the slope of the data points which is equal to $(-Q_a/R)$.

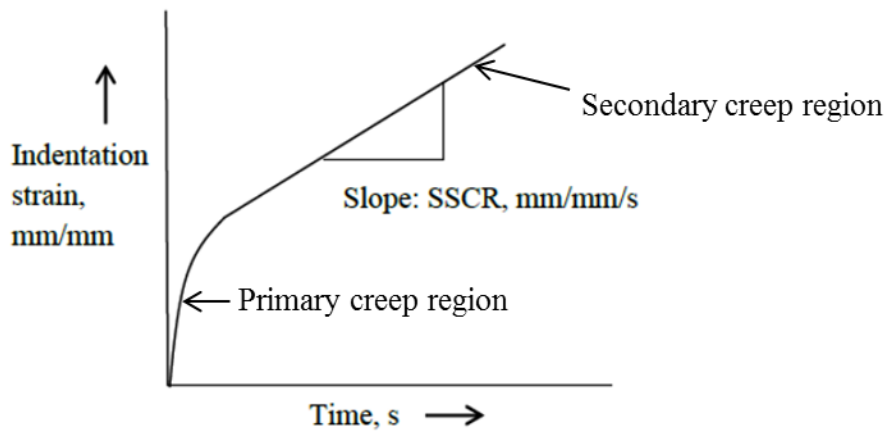


Figure 3.13 Schematic creep curve of indentation strain versus time.

3.5.5 Wear Test

The schematic diagram and the image of pin-on-disc used for assessment of wear behavior of the materials are shown in Figure 3.14. Cylindrical specimens with 28 mm length and 6 mm diameter, which were prepared according to ASTM G 99 standard used for the wear test. Prior to testing both the sides were made flat by polishing on SiC papers. EN31 hardened steel with an average hardness of 64 BHN was used as counter surface. The 120 mm of track diameter was kept constant throughout the experiment using a pin on disc tribometer (TR-20LE-PHM 400-CHM 600). Three levels (L_9) orthogonal array was used to conduct the experiment by varying applied load, sliding distance and sliding speed which is represented in Table 3.2. The volume loss occurred during the wear test was measured using digital weighing balance with an accuracy of 0.0001 grams. The specific wear rate (W_s) of the material was calculated by using the following relation,

$$W_s = \frac{V}{L \times D} \quad \text{Equation 3.7}$$

Where V is the volume loss in mm^3 , L is the applied load in N and D is the sliding distance in m .

Table 3.2 Levels of variables used in the experiment.

Factors	Level 1	Level 2	Level 3
(A) Applied load (N)	29.41	58.83	88.25
(B) Sliding distance (m)	1500	3000	4500
(C) Sliding speed (m/s)	1	2	3

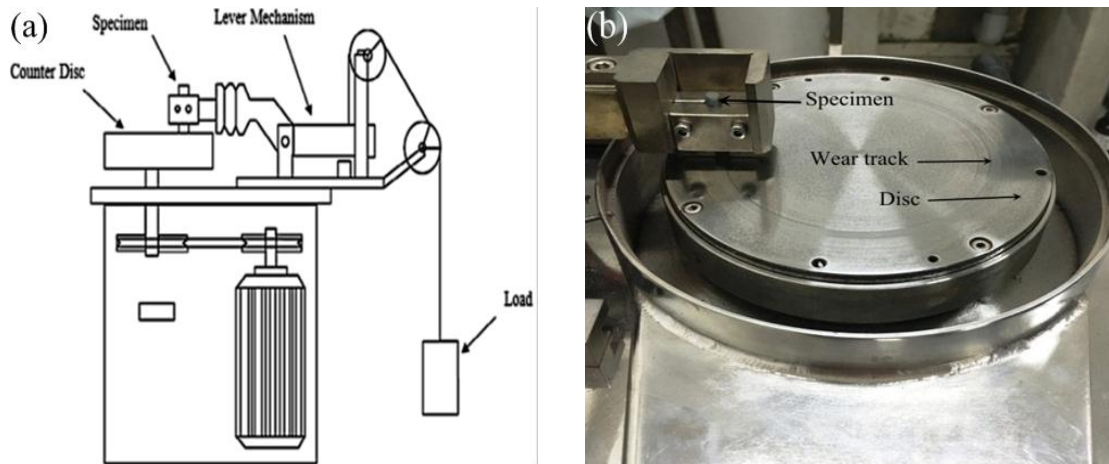


Figure 3.14 Pin on disc tribometer (a) schematic diagram and (b) photograph of pin on disc wear testing machine.

3.5.6 Design of Experiments for Wear Test

The standard L_9 orthogonal array is adopted for dry sliding wear test with three parameters such as applied load, sliding distance, and sliding speed by varying them for three levels. The three important factors play a prominent role in the selection of orthogonal array in order of priority viz., the number of factors, number of levels for the factors and the desired experimental resolution. The L_9 orthogonal array was selected from the standard condition that degree of freedom (DOF) for the orthogonal

array must be greater than or equal to sum of those wear parameters. DOF of control factors and DOF of orthogonal array are calculated as follows,

DOF of control factors is: level-1

DOF of orthogonal array: number of trials-1

From Table 3.2 it is shown that the total number of factors are three and total number of levels are three for each factor. Therefore, DOF of each control factors approach to two (i.e., DOF of control factors: $3-1=2$). Total DOF of all three control factors approaches to six and DOF of L_9 orthogonal array approaches to eight (i.e., DOF of orthogonal array: $9-1=8$). Therefore, DOF of orthogonal array is greater than DOF of control factors. Hence, it obeys the standard condition proposed by Taguchi.

A total of 9 experiments were performed based on the run order generated by the Taguchi model as shown in Table 3.3. The response for the model is on specific wear rate. The objective of the model is to minimize the specific wear rate.

Table 3.3 Taguchi's L_9 orthogonal array.

Experiment No.	Applied load (N)	Sliding distance (m)	Sliding speed (m/s)
1	29.41	1500	1
2	29.41	3000	2
3	29.41	4500	3
4	58.83	1500	2
5	58.83	3000	3
6	58.83	4500	1
7	88.25	1500	3
8	88.25	3000	1
9	88.25	4500	2

CHAPTER 4

RESULTS AND DISCUSSION

In the present work, Zn-24Al-2Cu alloys were multi directional forged (MDF) under two different temperatures: 100 °C and 200 °C for three and six number of passes. The MDF processed samples were subjected to post-aging heat treatment. The solutionized, MDF processed and MDF processed combined with aging heat treatment samples were characterized and their mechanical properties were evaluated. The details of the results and discussion are presented in this chapter.

4.1 Zn-24Al-2Cu Alloy

As-cast Zn-24Al-2Cu alloy was observed under optical microscopy and its microstructure is shown in Figure 4.1.

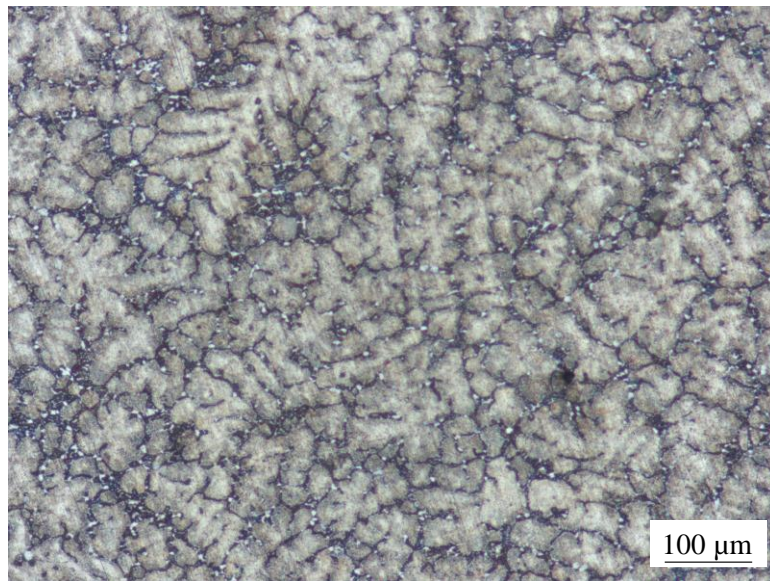


Figure 4.1 Optical micrograph of as-cast Zn-24Al-2Cu alloy (100X Magnification).

In the present study, as-cast material was solutionized at 365 °C for 5 hours by using muffle furnace and quenched in water at room temperature. Solutionizing temperature was selected from binary phase diagram of Zn-Al alloy. The phase diagram of Zn-Al binary alloy system and 350 °C isothermal section of the ternary Zn-Al-Cu alloy system

are shown in Figure 2.2 and 2.3 respectively. At 365 °C, the dissolution of Zn and Al takes place and as-quenched specimen was in the supersaturated β phase. Later β phase transformed to α , ϵ and η phases. The optical and scanning electron microscopy (SEM) images of the microstructure of solutionized and quenched alloys are shown in Figure 4.2 (a) and (b) respectively. The microstructure is observed to be consisting of three phases, viz., (i) White phase marked A (Cu-rich), (ii) Grey dendritic phase marked B (Al-rich) and (iii) Dark dendritic phase marked C (Zn-rich). The Al-rich α phase appearing as grey particles along with ϵ phase is shown in Figure 4.2. It was shown that appearance of α phase over the grain boundary of η phase is due to discontinuous precipitation (Dorantes et al., 1999). The average grain size was measured by linear intercept method and found to be approximately 30 μm on the solutionized and quenched sample.

MDF was initially carried out at room temperature, but it resulted in the fracture of the sample during processing. It should be noted that Zn is the major alloying element with hexagonal close packed crystal structure which possess limited slip systems, making it difficult to forge at room temperature (Purcek 2005). Hence, MDF was carried at 100 °C for three passes and 200 °C for six passes, as more number of slip systems become active at higher processing temperature.

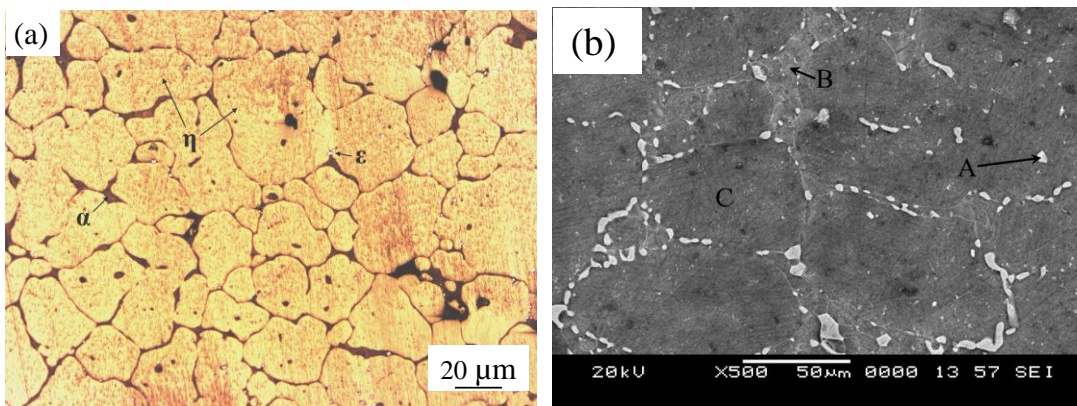


Figure 4.2 Solutionized sample (a) optical micrograph (500X Magnification) and (b) SEM micrograph (3% Nital etchant).

4.2 MDF of Zn-24Al-2Cu

Solutionized materials are further MDF processed at 100 °C up to three passes and at 200 °C up to three and six passes and they are characterized.

4.2.1 XRD Analysis

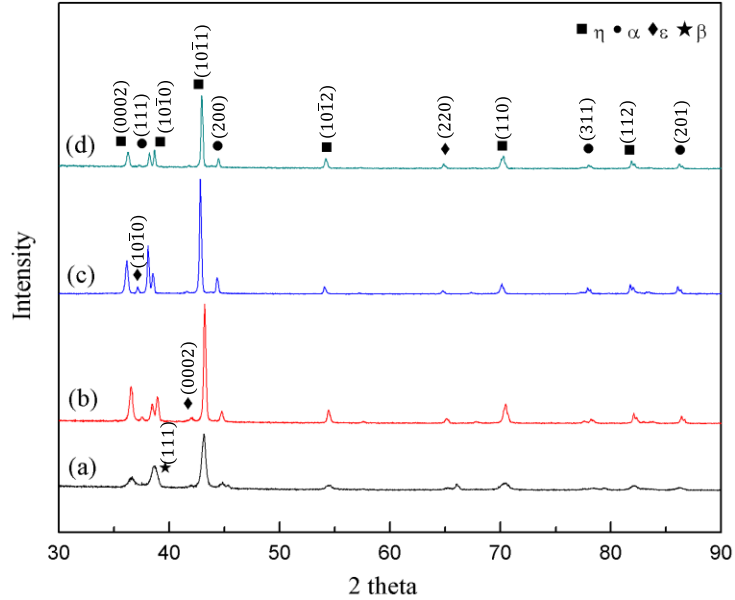


Figure 4.3 XRD patterns of (a) solutionized (b) MDF-100 °C-3P (c) MDF-200 °C-3P and (d) MDF-200 °C-6P.

The XRD analysis on the solutionized sample indicated the presence of (i) ϵ phase (CuZn_4), (ii) β phase, which is of Zn-rich FCC phase, later transformed into (iii) η (Zn-rich HCP phase) and (iv) α (Al-rich FCC phase) as shown in the profile (a) of Figure 4.3. This fact is confirmed by the SEM images presented in Figure 4.2. The plastic deformation due to subsequent MDF process has initiated the decomposition of β phase. Therefore, the peak intensities for the β phase in XRD profile decreases while those of α and η phases decrease after MDF processing at higher temperatures (profile b-d).

It was reported that η phase and α phase dissolved to a larger extent when the alloy was solution treated at higher temperature (Liu et al., 2013). It is observed in the XRD profile that η phase shifts slightly in the 2θ values from 43.3572 in solutionized sample to 43.2882 on processed sample at 100 °C for three passes. Similar peak shift to 42.9762 is

seen in the case of sample processed at 200 °C up to six passes. The peak shift of η phase to lower 2θ values is an indicative of conversion of unstable phase to stable one. In the case of sample MDF processed at 200 °C up to six passes, η phase peak intensity decreases as compared to sample MDF processed at 100 °C up to three passes. This may be due to the increased dislocation density in the MDF processed samples for higher number of passes. It is known fact that dislocations support the diffusion process leading to faster dissociation of β phase into α and η phases. This similar peak shift was observed earlier for cold working of binary Zn-Al alloy (Zhu 2004).

4.2.2 Microstructure

Figure 4.4 (a) and (b) shows the optical and SEM micrographs of MDF processed sample at 100 °C up to three passes. It can be seen from the optical images of microstructure that significant refinement of grains takes place during MDF process. The average grain size of the solutionized sample is 30 μm which is reduced to 2 μm after MDF processing at 100 °C up to three passes. Figure 4.5 (a) and (b) shows the optical and SEM micrographs of MDF processed at 200 °C after three passes. The average grain size is in the range of 1.5 μm . Figure 4.6 (a) and (b) shows the optical and SEM micrographs of MDF processed at 200 °C after six passes. After six passes of MDF processing, a homogeneous grain structure with an average grain size of approximately 1 μm is achieved.

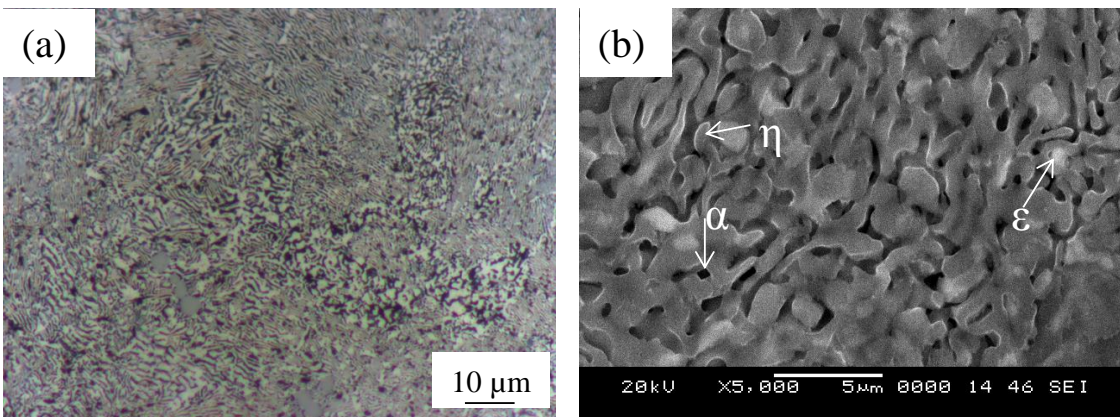


Figure 4.4 Multidirectional forged sample at 100 °C up to three passes (a) optical micrograph (1000X Magnification) and (b) SEM micrograph (3% Nital etchant).

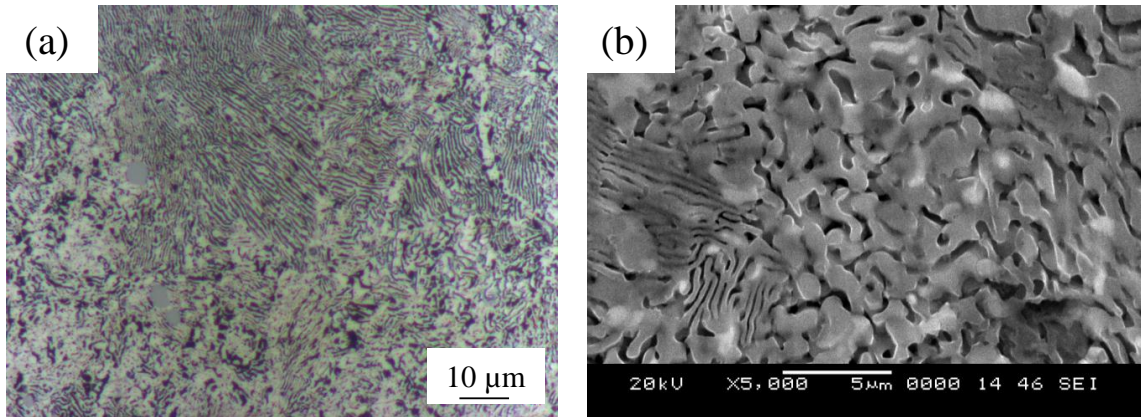


Figure 4.5 Multidirectional forged sample at 200 °C up to three passes (a) optical micrograph (1000X Magnification) and (b) SEM micrograph (3% Nital etchant).

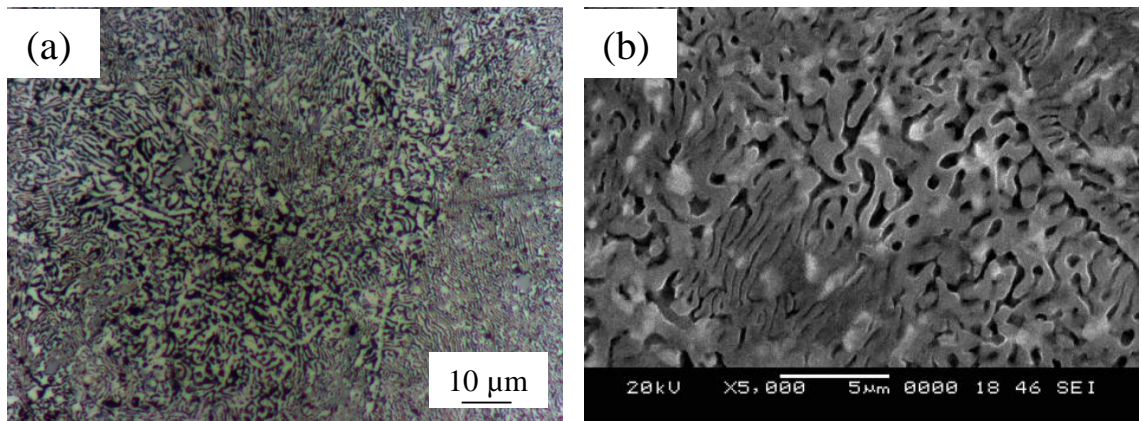


Figure 4.6 Multidirectional forged sample at 200 °C up to six passes (a) optical micrograph (1000X Magnification) and (b) SEM micrograph (3% Nital etchant).

After three passes of MDF processing at 100 °C the coarse grains are seen to be elongated illustrating a plastically deformed structure, whereas the Al-rich phase distributed uniformly as shown in Figure 4.4. It can be observed that as the number of passes increased the refined Al-rich α phase particles were distributed more uniformly and grain size decreased considerably. The microstructure of the alloy processed up to six passes at 200 °C revealed lamellae with a homogeneous array of equiaxed grains and agglomerates of Zn-rich and Al-rich grains. These features are discernible in Figure 4.6.

4.2.3 Mechanical Properties

The results of hardness measurements are shown in bar chart presented in Figure 4.7. The Rockwell hardness of the solutionized alloy is 56 HRH. Samples processed at 100 °C for three passes exhibit hardness to the level of 71 HRH. Processing the sample at 200 °C for three passes, hardness value increased to 74 HRH. The highest hardness is achieved to the level of 76 HRH when the sample is processed at 200 °C for six passes. The increase in hardness can be attributed to the grain refinement with increased volume of grain boundaries which occur during intensive plastic deformation.

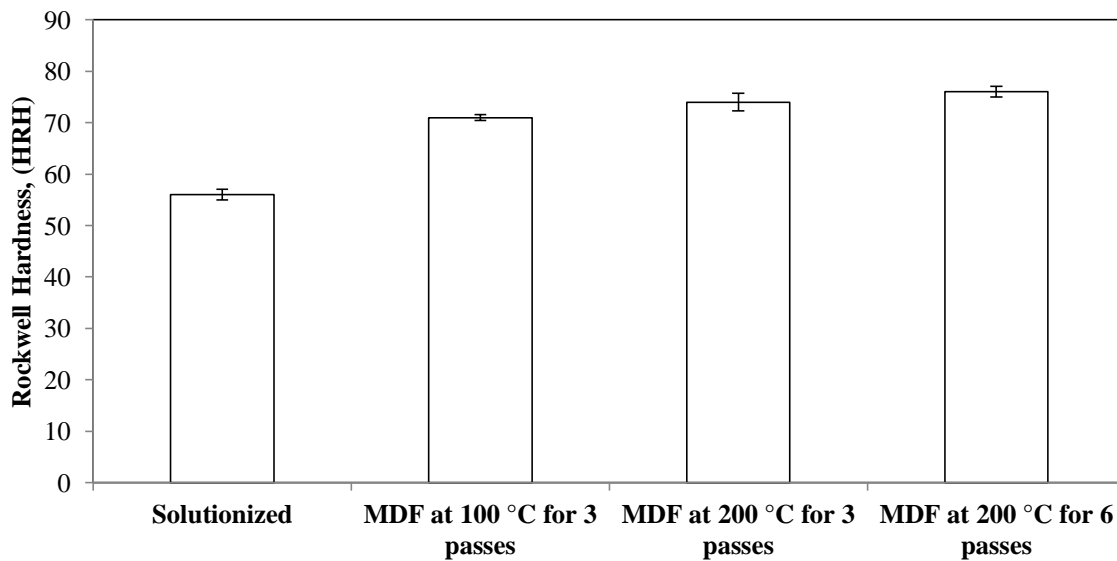


Figure 4.7 Bar chart showing Rockwell hardness variations for solutionized, MDF processed at 100 °C up to three passes and 200 °C up to three and six passes.

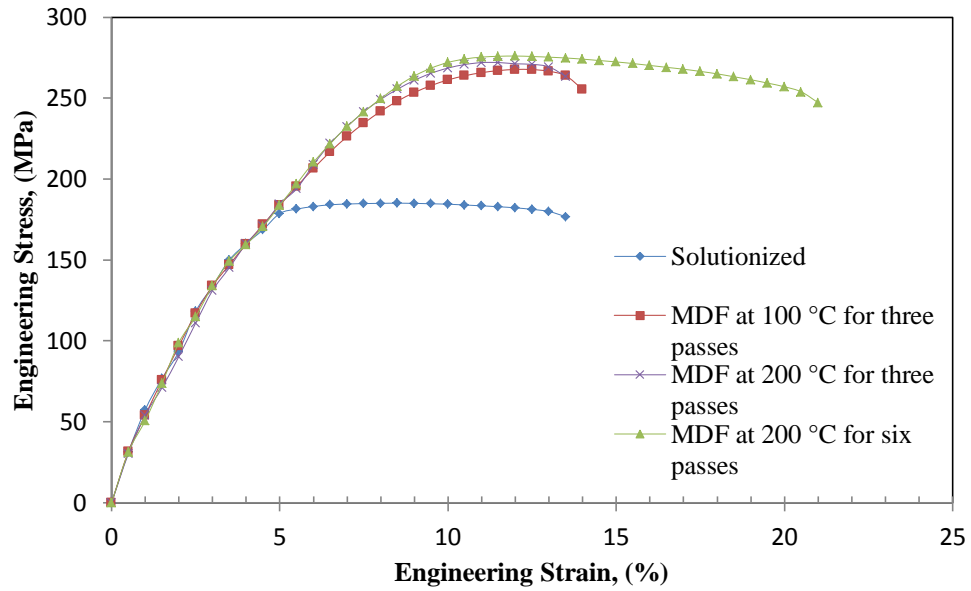


Figure 4.8 Engineering stress versus engineering strain graph from tensile test for solutionized, MDF processed at 100 °C up to three passes and 200 °C up to three and six passes.

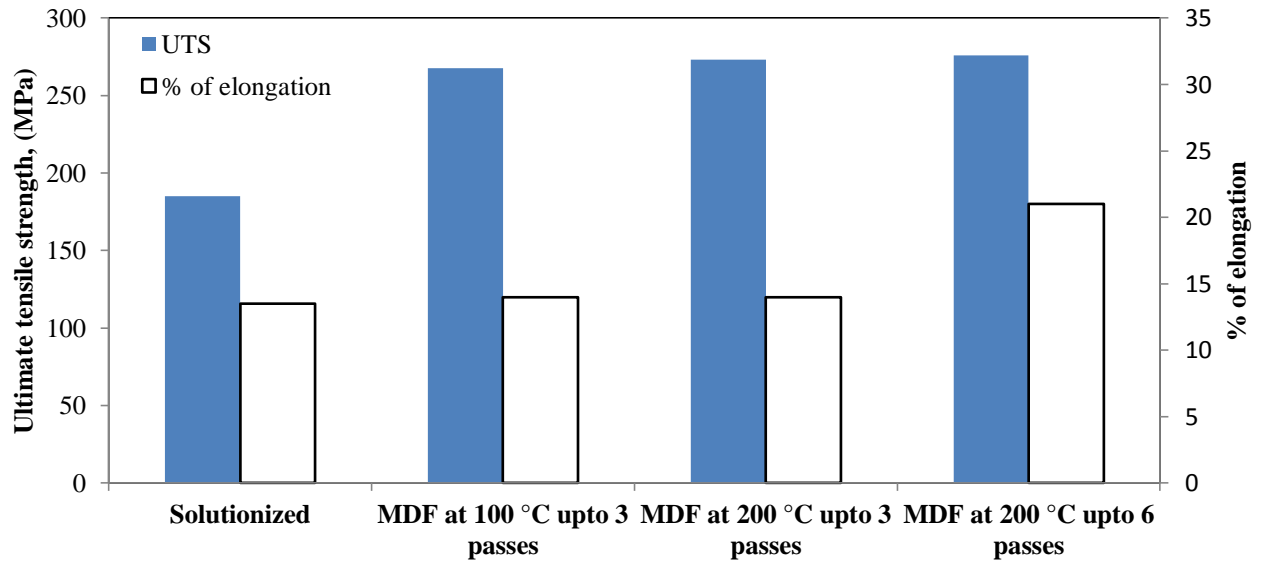


Figure 4.9 Bar chart showing ultimate tensile strength and percentage of elongation for solutionized, MDF processed at 100 °C up to three passes and 200 °C up to three and six passes.

Figure 4.8 shows the tensile test plots of engineering stress versus engineering strain for solutionized and MDF processed sample. Ultimate tensile strength (UTS) and percentage of elongation of Zn-24Al-2Cu alloys at different conditions such as solutionized, MDF at 100 °C up to three passes, MDF at 200 °C up to three passes and MDF at 200 °C up to six passes are presented in Figure 4.9. Solutionized sample shows UTS of 185 MPa and elongation of 13.5%. Further, it is found that strength can be increased to 267 MPa by processing the material at 100 °C up to three passes and can be increased further to 272 MPa and 276 MPa by processing at 200 °C up to three and six passes. In addition, material processed at 200 °C up to six passes exhibits a high level of percentage of elongation to the value of 21%. The large improvement in strength and ductility of MDF processed material can be attributed to many metallurgical factors such as: (i) grain refinement, (ii) reduction in density of porosity and (iii) reduced heterogeneity by way of improved uniform distribution of second phase particles (α) in the matrix of Zn-rich phase (η) as shown in Figure 4.4 (b) and 4.6 (b). In the case of the solutionized sample lower level of strength and ductility had been recorded as revealed in Figure 4.8 and 4.9. It could be attributed to the presence of copper rich ϵ intermetallic phase, which is basically hard and coarse. The ϵ phase greatly got refined when MDF process was carried out at higher temperatures. However, it is possible that the lamellae may block the sliding of equiaxed grains, leading to higher strength in the processed sample. The spherical and well spread Al-rich and Zn-rich phase obtained provides more equiaxed grains as seen in SEM micrographs presented in Figure 4.4 (b) and 4.6 (b).

Material properties such as strength co-efficient (K) and strain hardening exponent (n) were calculated using compression tests for solutionized and all MDF processed samples. All the tests were carried out at room temperature. The engineering stress-strain diagram obtained from the compression tests were used to study the strain hardening behavior after MDF processing. For this purpose, flow curves obtained were fitted to the power law equation:

$$\sigma = K \epsilon^n \quad \text{Equation 4.1}$$

Where, σ is the true stress, ϵ is the true plastic strain and K is the strength coefficient. According to this, double logarithmic plots of true stress against true strain result in a straight line with a slope of 'n'. The true stress and true strain obtained from compression testing are shown in Figure 4.10.

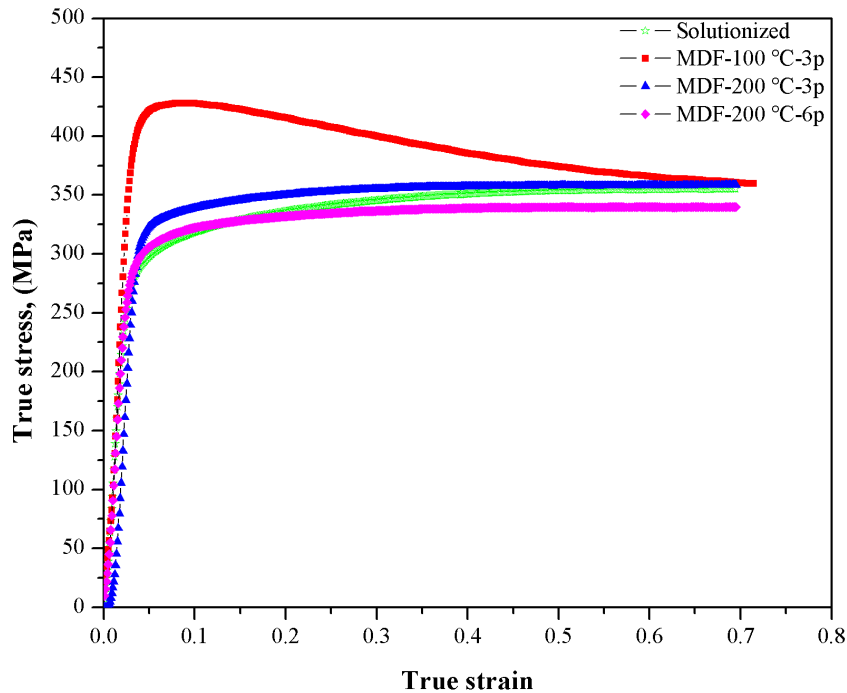


Figure 4.10 True stress versus true strain graph from compression test after solutionized, MDF processed at 100 °C up to three passes and 200 °C up to three and six passes.

From the results of the compression test, strength coefficient (K) and strain hardening exponent (n) values were determined and presented in Table 4.1. Average values of the strength coefficient (K) and strain hardening exponent (n) for different processing condition is presented in Figure 4.11. The material processed by MDF at 100 °C registers the value of n to 0.05, while that processed up to three passes at 200 °C registers it to 0.16. Further, the n value increases to 0.21 when material is processed for six passes at 200 °C whereas the n value of solutionized sample was 0.22. It exhibits considerable rise in K value after processing to different levels of strain The results presented in Figure

4.11 show that the value of K is 391.5 MPa for the materials processed by MDF up to three passes at 100 °C. The K value rises to 398.1 MPa for three passes at 200 °C and it further increases to 565.4 MPa for six passes at 200 °C whereas in the case of solutionized sample K value is 409.4 MPa.

Table 4.1 Strength coefficient (K) and strain hardening exponent (n) values for various processing without aging conditions.

Processing condition	Strain hardening exponent (n)		Strength coefficient (K), MPa	
	Values	Mean	Values	Mean
Solutionized	0.22	0.22	412.14	409.4
	0.22		405.78	
	0.23		410.51	
MDF-100 °C-3 pass	0.06	0.05	395.37	391.5
	0.05		380.91	
	0.05		398.23	
MDF-200 °C-3 pass	0.14	0.16	412.94	398.1
	0.16		385.71	
	0.17		395.51	
MDF-200 °C-6 pass	0.21	0.21	556.21	565.4
	0.21		574.02	
	0.23		566.16	

The n value is important in metal forming operation because it not only determines the material strength but also shows how the material behaves when it is being forged. Materials that have higher n values have better ductility than those with low n values. Hence, samples MDF processed for six passes at 200 °C shows higher ductility than with all other MDF processed samples.

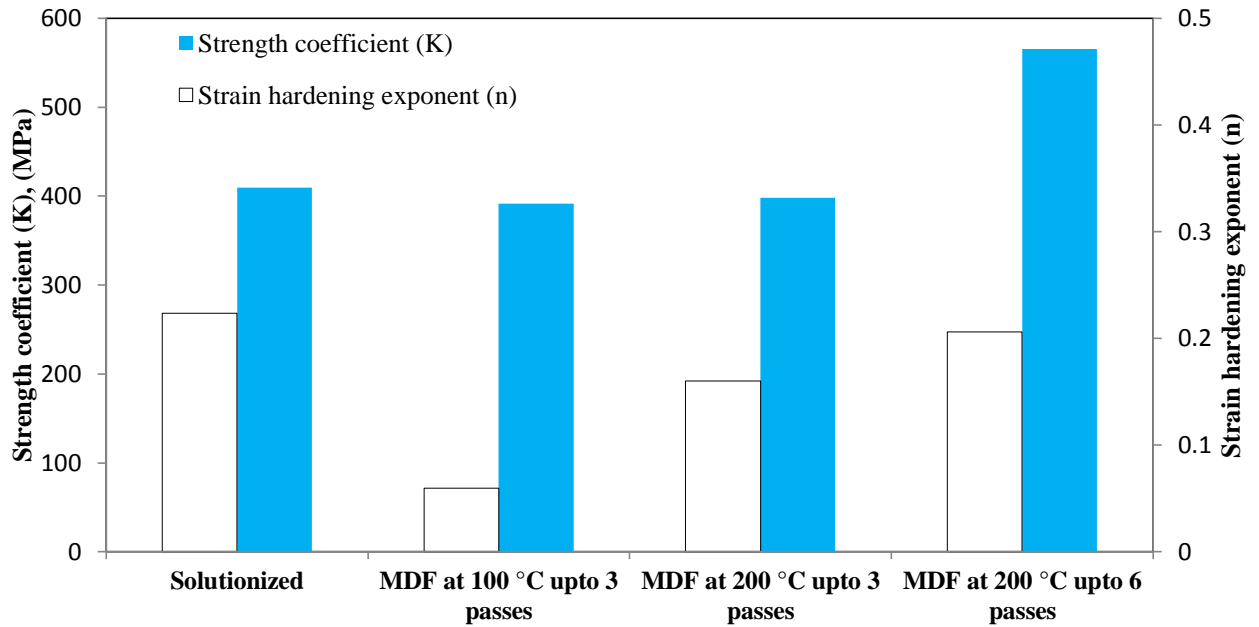


Figure 4.11 Bar chart showing strength coefficient (K) and strain hardening exponent (n) from compression test for solutionized, MDF processed at 100 °C up to three passes and 200 °C up to three and six passes.

Compression test results as presented in Figure 4.11 reveal that sample processed by MDF at 100 °C for three passes reached the early stage of recovery. Such materials exhibit lower strain hardening exponent (n) values. Those processed by MDF at 200 °C for six passes exhibit higher n value. Higher n value for these materials is indicative of a higher tendency to strain hardening. The recovered materials strain hardens considerably during compression, leading to higher values of n. Similar type of behavior was observed for commercial pure Ti subjected to ECAP at different temperatures (Preetham and Chakkingal, 2011). The value of the strength coefficient (K), increases with increasing number of passes. As number of passes increase, more dislocations get introduced which in turn increases the tendency for strain hardening.

MDF process involves large amount of plastic deformation. For plastic deformation to take place, it is essential that large amount of dislocations are generated and made to move. Grain boundaries can act as source and sink of dislocations as well as act as

barrier to dislocation movements. Huge number of dislocations generated by Frank-Reed source would disperse the dislocations present in the grain boundary during MDF processing. During the large application of strain, movement of dislocations need not move only on the conservative plane. Instead, their movement in the non-conservative plane is also possible. Dislocation-dislocation interaction can happen, which results in large amount of non-conservative segments such as jogs. If particles are present in the path of moving dislocations, they increase the length of the dislocations and promote more dislocation-dislocation interaction. All these activities will lead to increased dislocation density or formation of dislocation forest. A non-conservative movement of the dislocation creates huge amount of defects such as vacancies and interstitials. It is pictorially illustrated in Figure 4.12.

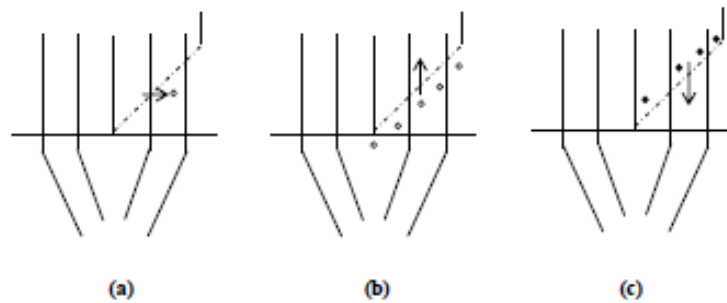


Figure 4.12 Movements of dislocation: (a) conservative (b) non-conservative and (c) non-conservative movements creating interstitials.

4.2.4 Fractography

Figure 4.13 (a) shows the SEM images of the fractured surface in the as-cast condition, in which features of brittle fracture are discernible. As-cast structures are inherently brittle because of the presence of interdendritic porosity in the matrix of highly segregated materials. Further, the precipitation of non-equilibrium hard ϵ phase also contributes to the brittleness of as-cast materials. The dendritic type structure contains interdendritic porosity during solidification due to incomplete filling of liquid melt and this is the reason for the brittle fracture in the as-cast alloy.

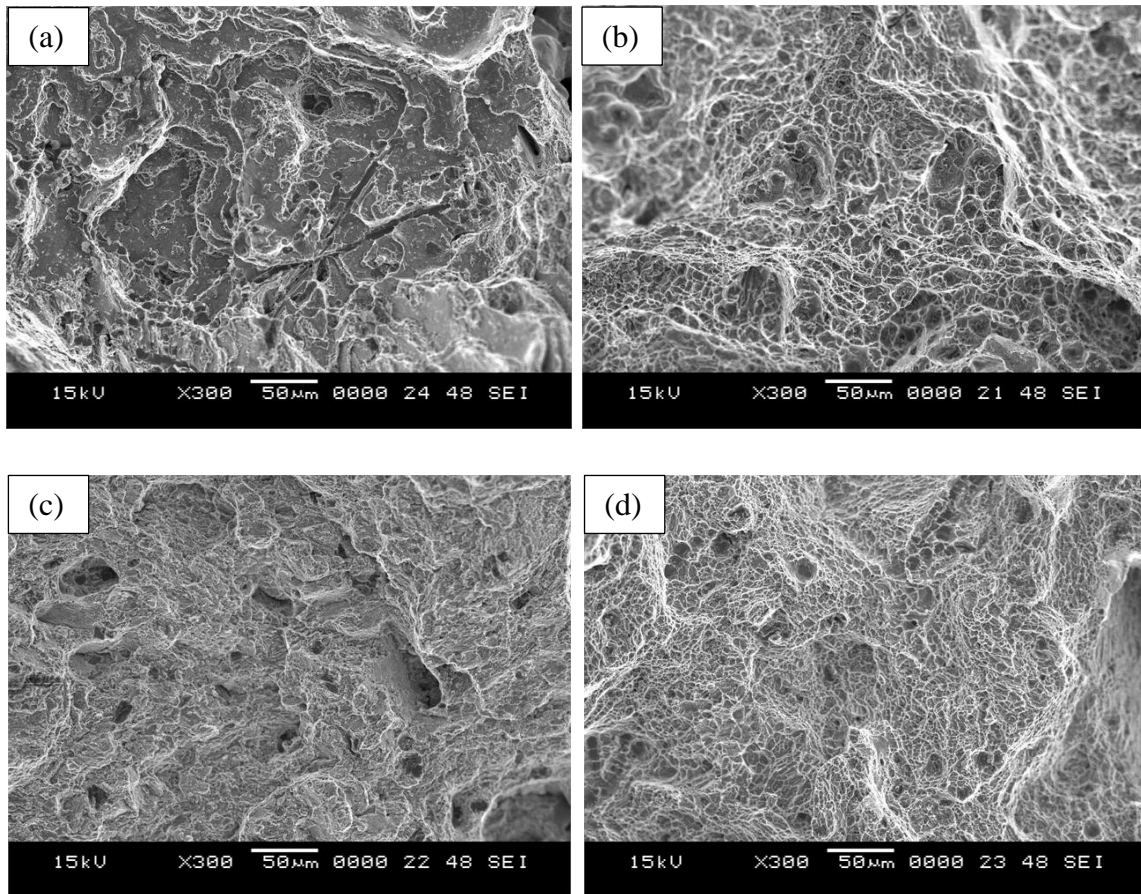


Figure 4.13 SEM images of the fracture surface of alloy after tensile tests in (a) as-cast (b) solutionized (c) MDF at 100 °C up to three passes and (d) MDF at 200 °C up to six passes.

In the case of solutionized fractured surface some dimples are seen in Figure 4.13 (b) which show the transformation of the brittle mode to ductile mode of fracture. In the processed sample after three passes at 100 °C and six passes at 200 °C as shown in Figure 4.13 (c) and (d), the fractured surfaces demonstrate many dimples which show that the brittle mode of fracture is completely transformed to ductile type. These micrographs reveal how microstructural evolution during processing influences the fracture behavior. It is observed in Figure 4.13 (b) that for solutionized condition, fracture surface was composed of micro-porosities and dimples were large. Hence, ductility is low. After MDF processing dimples size decreased and showed a homogeneous distribution across

the fracture surfaces as shown in Figure 4.13 (c) and (d). It resulted in improved ductility compared to solutionized material. It represents that the material was deformed uniformly in the equiaxed structure with fine grain boundaries.

4.3 Precipitation Hardening of Zn-24Al-2Cu

Samples were solution-treated at 365 °C for 5 hours and quenched in water at room temperature. These samples were subsequently aged at 100, 150, 200 and 250 °C for 0.5 to 24 hours. The heat treated samples were analyzed by X-Ray diffractometry and measurement of Vickers micro hardness of each sample.

4.3.1 Age Hardening Profile

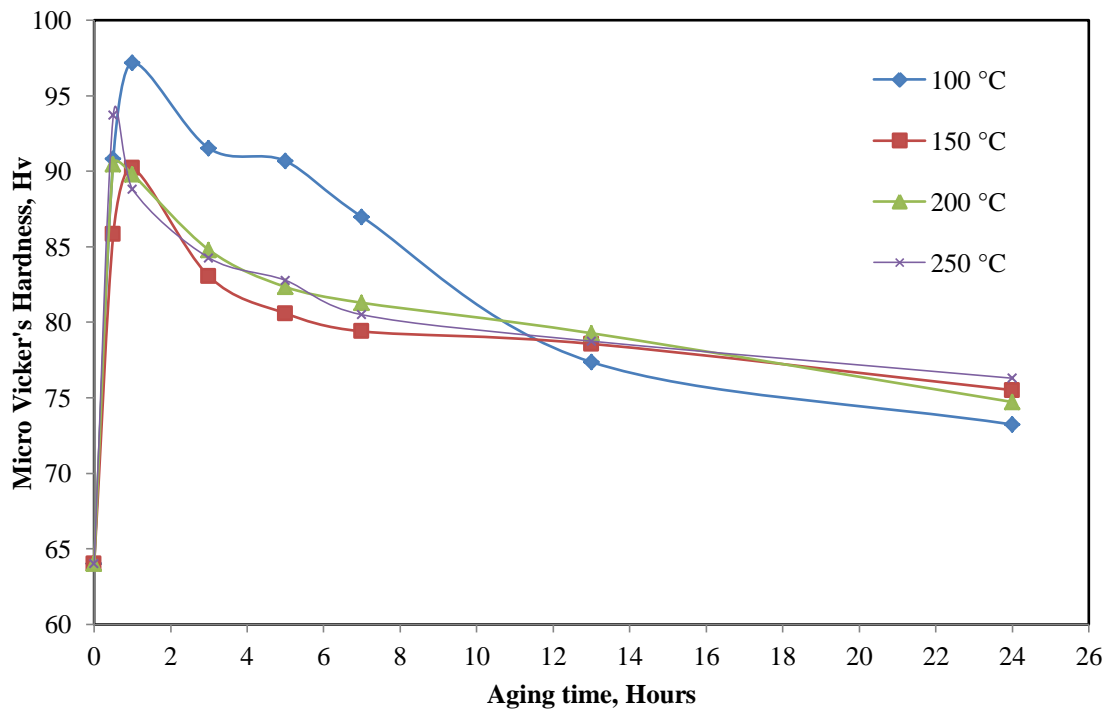


Figure 4.14 Hardness curves of the Zn-24Al-2Cu alloy aged at 100, 150, 200 and 250 °C for different times.

The hardness curves of the samples aged at 100, 150, 200 and 250 °C for different periods of time are shown in Figure 4.14. The high hardness occurred in the

sample aged at 100 °C for one hour. Nevertheless, the over aging process occurred faster in the samples aged at 250 °C and 200 °C than those aged at 100 and 150 °C. The fastest over aging of the samples aged at 250 °C can be attributed to the fast coarsening process of τ' phase at this temperature. At any temperature of aging, hardness decreases if aging is carried out for a long duration of time which is shown in Figure 4.14. Many factors are operating in its effect. Formation of the τ' phase is one of them. The formation of τ' phase is noted for long aging durations in the present investigation. This fact is also supported by the work carried out by Prasad (1996). It is known fact that aging process relieves the internal stress across the phase boundary by permitting local rearrangement of atoms. This reduces the resistance to the movement of the dislocation by the second phase particles (α phase) which in turn reduce the hardness. One more reason for decrease in hardness is the depletion of Al solute atoms from the matrix of Zn during the growth of η phase whereby the solid solution hardening of the matrix is effective to a lesser extent. At low aging temperature of 100 °C, the precipitated phases are very fine, which result in a relatively high hardness. At high aging temperature of 250 °C, they may coarsen less number of distantly placed α phase surrounded by η phase. As a result hardness decreased significantly (Dorantes et al., 2005). Hence, in the present work 100 °C aging temperature and one hour aging time is selected for post-aging heat treatment of MDF samples, which are required to be studied for improved mechanical properties.

4.3.2 XRD Analysis

The XRD patterns of samples aged for different time durations are shown in Figure 4.15-4.18. It is observed that the supersaturated β phase is decomposed at the early stage of aging. After aging at 100 °C for 0.5 hours, peaks of the β phase disappeared accompanying with the formation of α , η and ε phases.

The diffraction peak of τ' phase was detected in the samples which had been aged at 100 °C for 3 hours, accompanied by the decrease in the intensity of ε phase. It has been proved by Zhu (2004) that τ' is rhombohedral phase showing formula Al_4Cu_3Zn . Decreased intensity of ε phase after 3 hours of aging with increased intensity of τ' phase

is clear from Figure 4.15 with enlarged image. In addition, with the increase in aging temperature from 100 °C to 200 °C and 250 °C as shown in Figure 4.17 and 4.18, the diffraction intensity of the ϵ phase started to decrease earlier. Correspondingly, that of τ' phase started to increase. This shows that ϵ phase gradually transformed into τ' phase at elevated temperature with shorter periods of aging. It is evident from XRD plots that the rate of transformation is faster in the case of 250 °C compared to those of 100 °C, 150 °C and 200 °C temperatures.

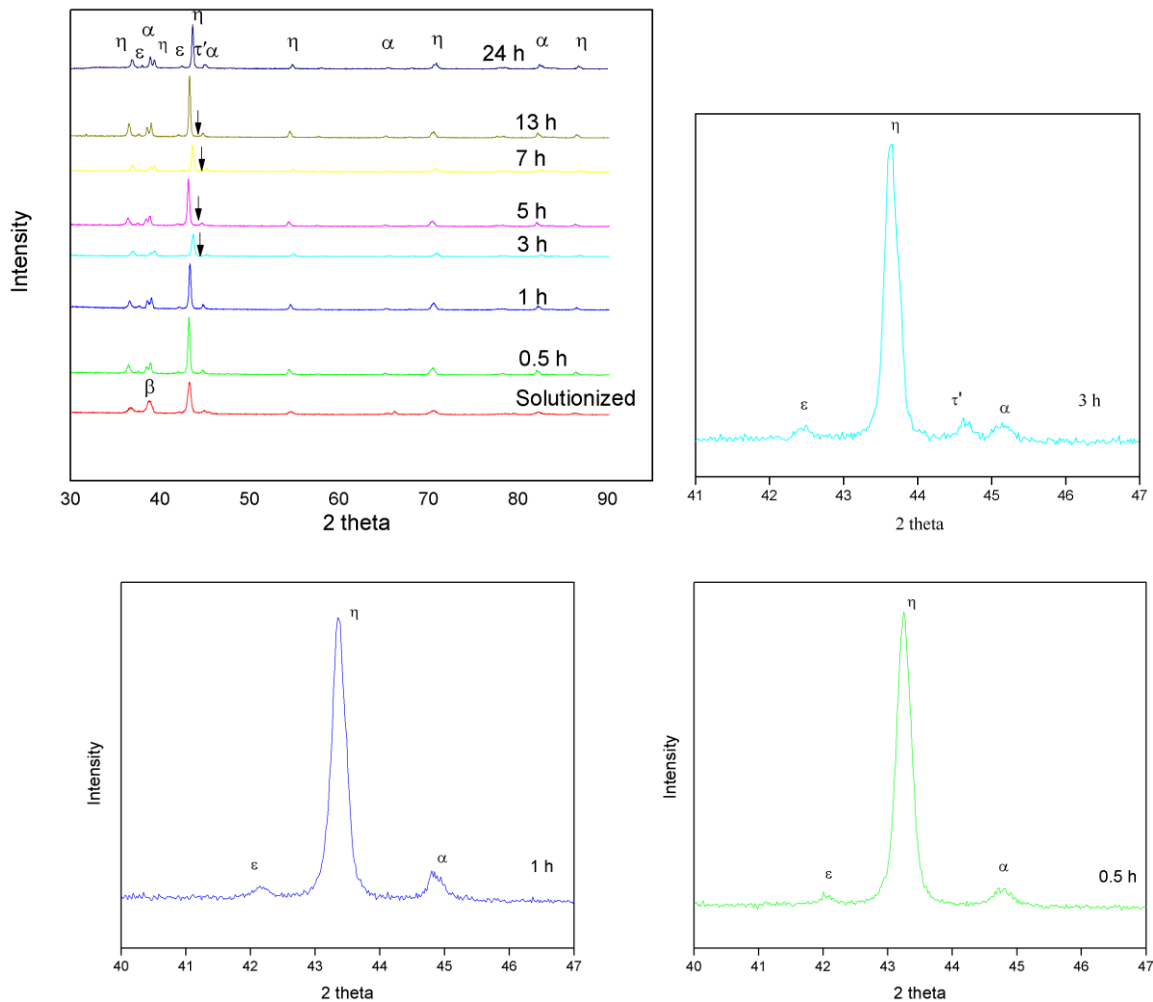


Figure 4.15 XRD patterns of sample solution treated at 365 °C for 5 hours water quenched and aged at 100 °C for different durations; with enlarged view showing τ' phase after three hours of aging.

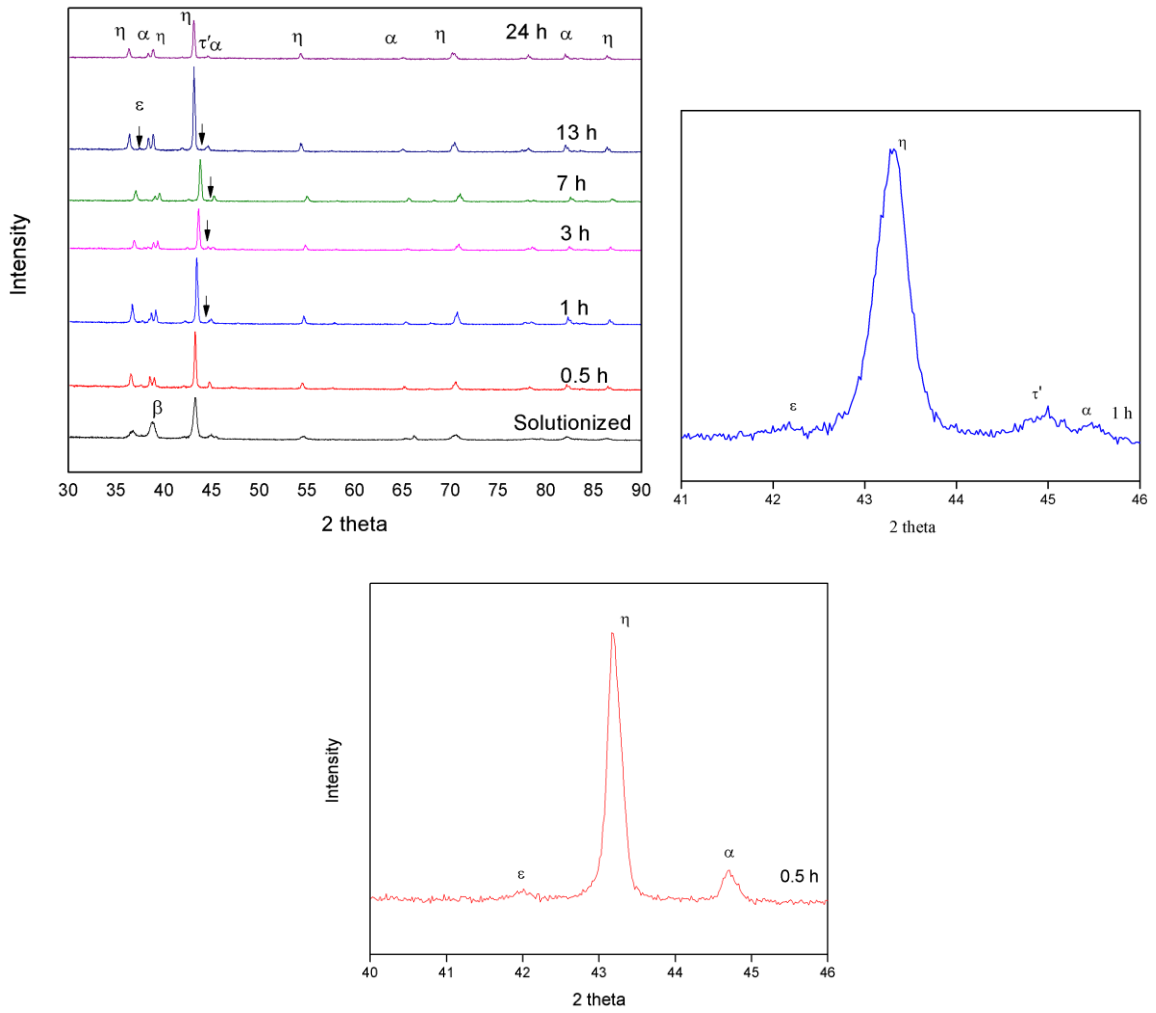


Figure 4.16 XRD patterns of sample solution treated at 365 °C for 5 hours water quenched and aged at 150 °C for different durations; with enlarged view showing τ' phase after one hours of aging.

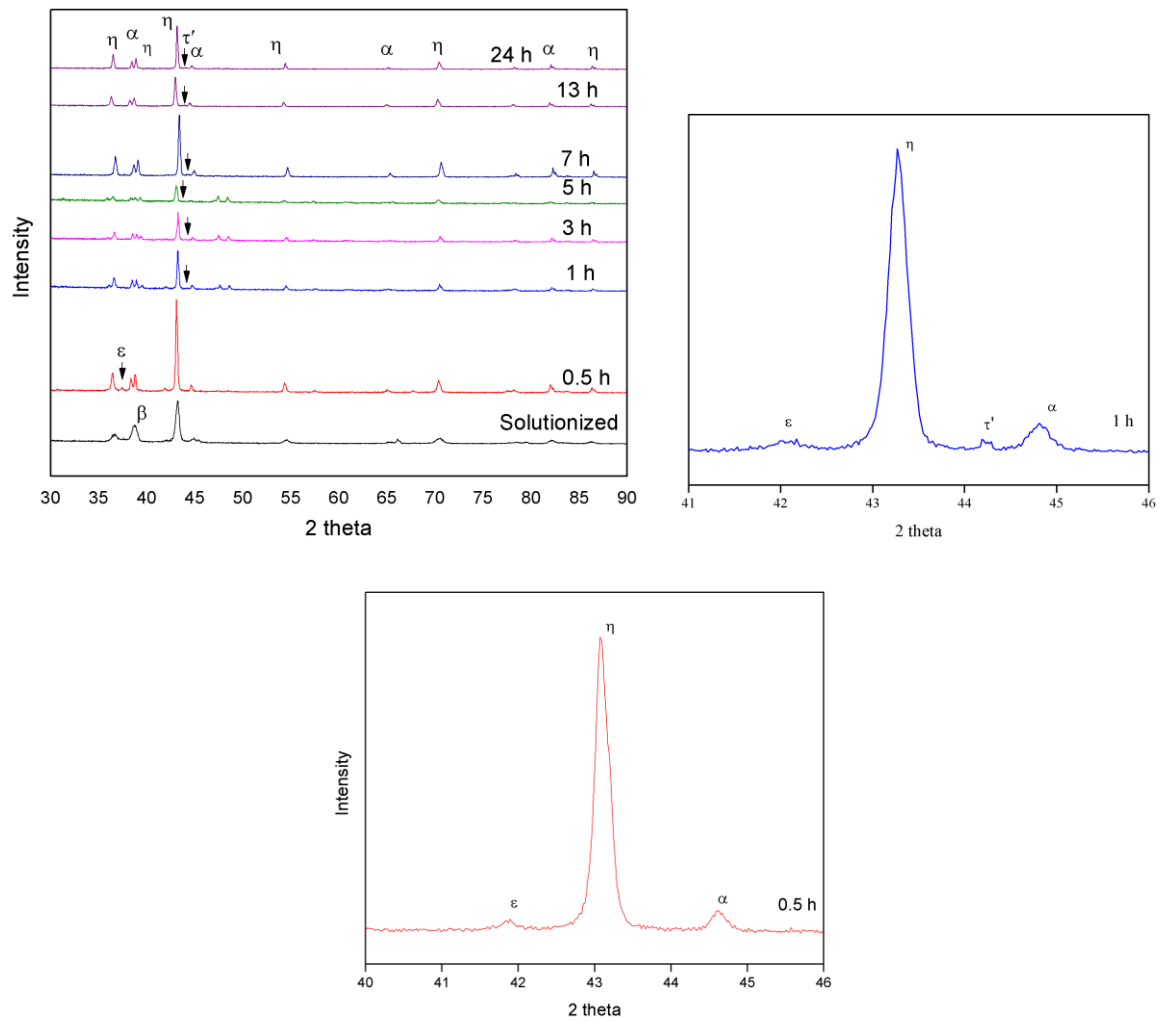


Figure 4.17 XRD patterns of sample solution treated at 365 °C for 5 hours water quenched and aged at 200 °C for different durations; with enlarged view showing τ' phase after one hours of aging.

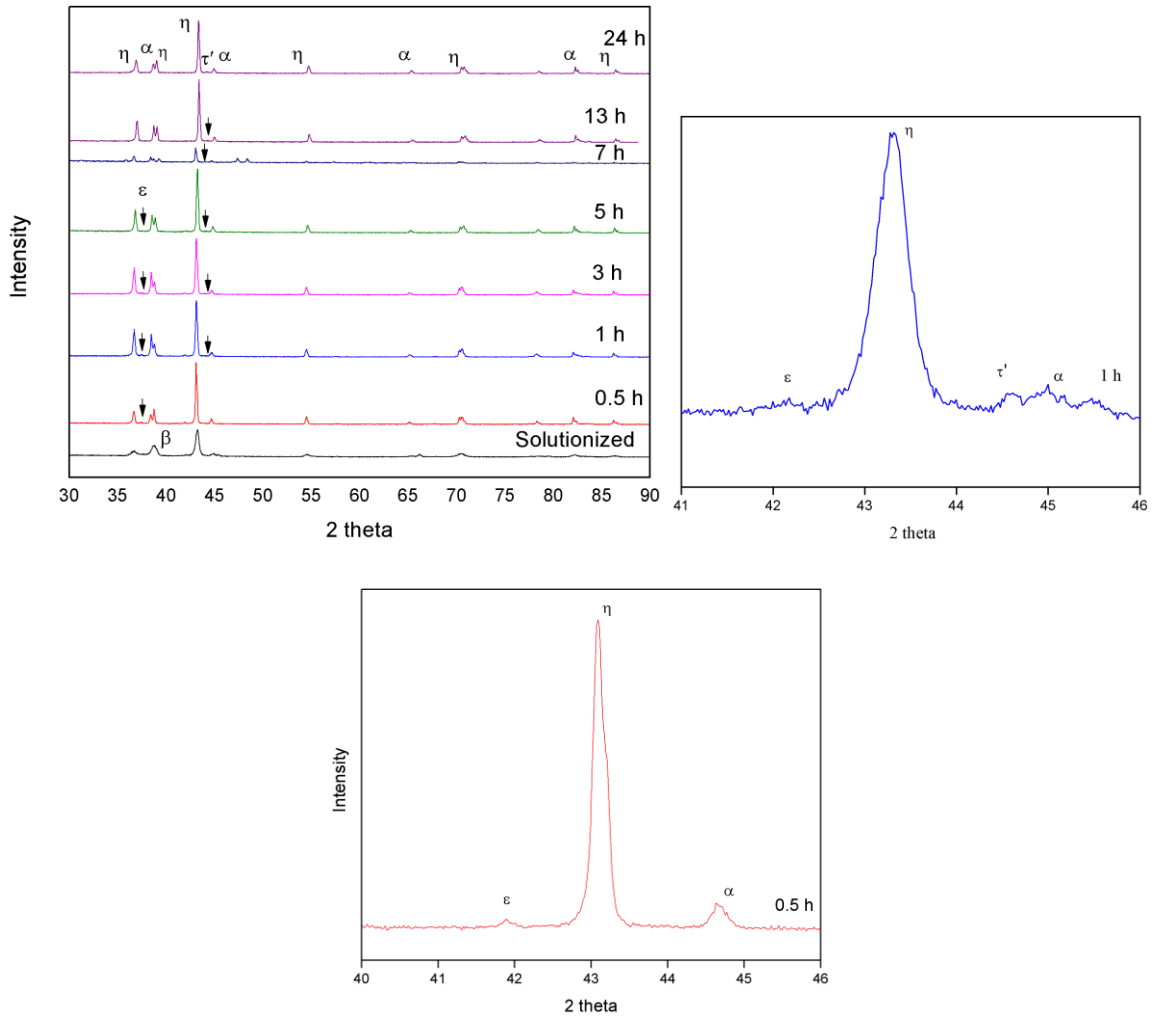


Figure 4.18 XRD patterns of sample solution treated at 365 °C for 5 hours water quenched and aged at 250 °C for different durations; with enlarged view showing τ' phase after one hours of aging.

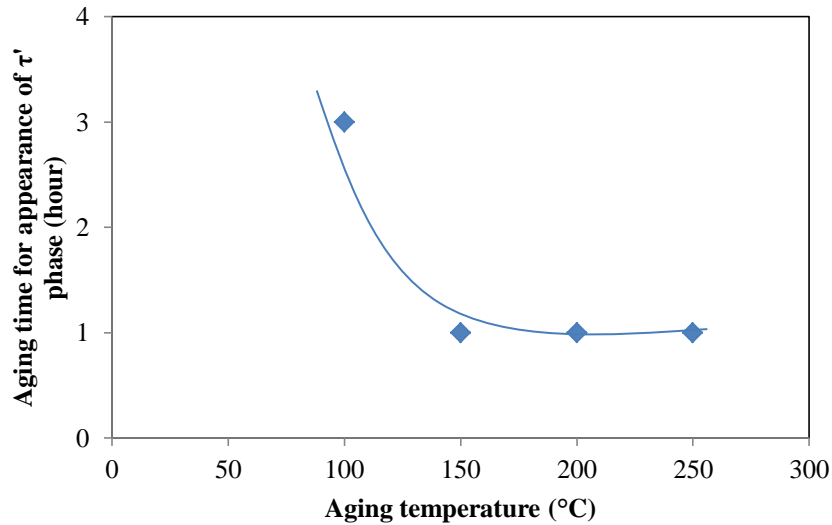


Figure 4.19 Aging time for appearance of τ' phase versus aging temperature from XRD analysis.

The XRD analysis of aged samples at 100, 150, 200 and 250 °C for 30 minutes to 24 hours are presented in Figure 4.15-4.18. This shows that aging at 100 °C for 30 minutes cause diffraction peaks of the β phase to disappear and simultaneously causing the formation of α , η and ε phases. Obviously, the formation of α , η and ε phases is one of the characteristics of the decomposition of the β phase. Aging for the longer time, it is seen that the diffraction intensity of the ε phase continuously decreased, while the intensity of the τ' phase increased. This confirms that phase transformation has been occurred by the conversion of ε phase to τ' phase for a longer time of aging. This observation is supported by earlier work that suggested a four-phase transformation: $\alpha+\varepsilon \rightarrow \tau'+\eta$, for aging of Zn-Al material at 250 °C (Savaskan et al., 1990). For aging at 200 °C and 250 °C, phase transformation started to occur at shorter time of one hour. The higher thermal energy available at these temperature regimes enhances the formation of the new phase and diffusion. Therefore, the decomposition of the τ' phase is accelerated at higher temperature for a shorter period of time. Similar types of observations were made and reported earlier (To et al., 2006).

From the analysis of XRD peaks, a graph is plotted with aging time for the appearance of τ' phase versus aging temperature. The plot is shown in Figure 4.19. It is observed that τ' phase will occur more rapidly at higher aging temperature because of the faster diffusion process.

4.3.3 Solutionized and Aging at 100 °C for One Hour

The optical and SEM images of the microstructure of the solutionized and aged sample for one hour at 100 °C and subsequently water quenched at room temperature are shown in Figure 4.20 (a) and (b) respectively. The microstructure is seen to be consisting of Al-rich α phase, Zn-rich η phase and ϵ phase. The average grain size measured by linear intercept method was found to be in the range of 30.2 μm on the solutionized and quenched sample with aging at 100 °C for one hour.

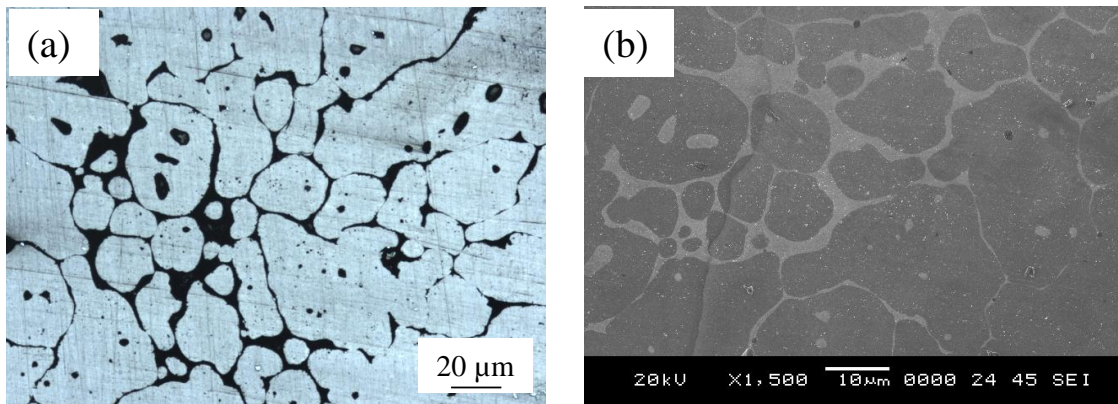


Figure 4.20 (a) Optical micrograph (500X Magnification) (b) SEM micrograph of solutionized and aged at 100 °C for one hour (3% Nital etchant).

4.4 MDF with Aging at 100 °C for One Hour

MDF processed at 100 °C up to three passes and at 200 °C up to three and six passes were further heat treated at 100 °C for one hour and they were characterized.

4.4.1 XRD Analysis

The X-Ray diffraction patterns of the samples solutionized and MDF processed for three passes at 100 °C, three and six passes at 200 °C and then post-aged at 100 °C for one hour are shown in Figure 4.21. A mixture of η , α and ε phases were present in the case of MDF processed sample as shown earlier in Figure 4.3. It can also be observed from Figure 4.21 that the solutionized and quenched sample later, MDF processed and post-aged one promote the formation of α , η , ε phase only. It is clear that aging of MDF processed sample will not enhance the formation of τ' phase during aging at 100 °C for one hour as revealed by the XRD results.

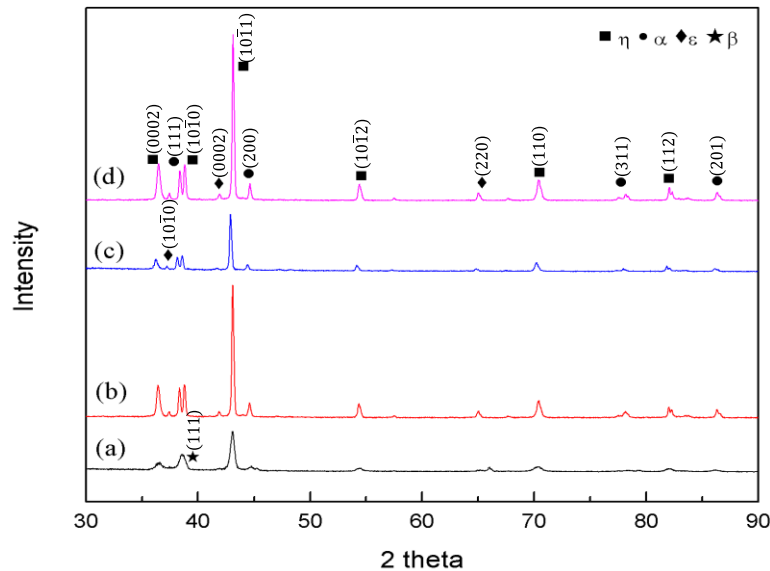


Figure 4.21 XRD patterns of (a) solutionized (b) MDF-100 °C-3P+aging, (c) 200 °C-3P+aging and (d) 200 °C-6P+aging.

It was observed that the β phase decomposed at the early stage of aging. It is confirmed by the fact that the XRD intensity of the β phase decreased, accompanying the formation of three phases α , ε and η , i.e., $\beta \rightarrow \alpha + \varepsilon + \eta$, after aging. A similar result was declared by Zhu (2004). After aging at 100 °C for one hour the β phase decomposed at the grain boundaries and this discontinuous precipitation of α was developed along the grain boundaries as shown in SEM images in Figure 4.20 (b). But ε phase is much

dispersed in aged sample as compared to solutionized sample. In addition, during aging more precipitates of α phase were observed in the regions of η phase.

From the XRD results it can be suggested that post-aging of MDF processed sample will not encourage the formation of τ' phase during aging at 100 °C for one hour. As it was shown from XRD analysis in Figure 4.15 that formation of τ' phase is possible only after three hours of aging at 100 °C. Because of the external stress, the specimens are already deformed, a high density of dislocations are introduced both at grain boundaries and inside the grains that provide effective nucleation sites for the formation of the new phases and enhance the diffusion. In addition to diffusion through the bulk of a solid, atoms may migrate along external and internal paths that afford lower energy barriers to motion. Thus, diffusion can occur along dislocations and grain boundaries. The rate of diffusion along such short-circuit paths are significantly higher than volume diffusion. However, most cases of mass transport are due to volume diffusion because the effective cross-sectional areas available for short-circuit processes are much smaller than those for volume diffusion (Paul et al., 2014). Lower aging temperature (100 °C) and short duration of aging (one hour) kinetically might not being favourable for the decomposition of α and ϵ phase in the formation of τ' phase. Similar types of observations were recorded by To et al., (2006) for Zn-Al based alloy.

4.4.2 Microstructure

Figure 4.22 (a) and (b) shows the optical and SEM micrographs of MDF processed sample at 100 °C up to three passes with post-aging at 100 °C for one hour. The average grain size is in the order of 2.3 μm . After processing at 100 °C up to three passes grains are seen to be mixture of lamellar, fragmented and non-uniformly distributed Al-rich phase. Figure 4.23 (a) and (b) shows the optical and SEM micrographs of MDF processed sample at 200 °C after three passes with post-aging at 100 °C for one hour. The average grain size measured is in the range of 1.8 μm . Figure 4.24 (a) and (b) shows the optical and SEM micrographs of MDF processed sample at 200 °C after six passes with post-

aging at 100 °C for one hour. The average grain size recorded from these images is around 1.3 μm .

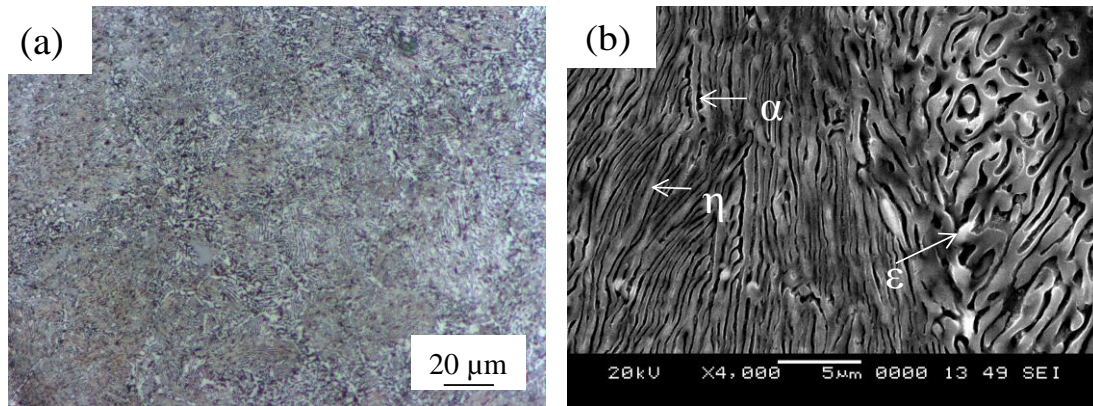


Figure 4.22 Multidirectional forged sample at 100 °C up to three passes and post aging at 100 °C for one hour (a) optical micrograph (500X Magnification) and (b) SEM micrograph (3% Nital etchant).

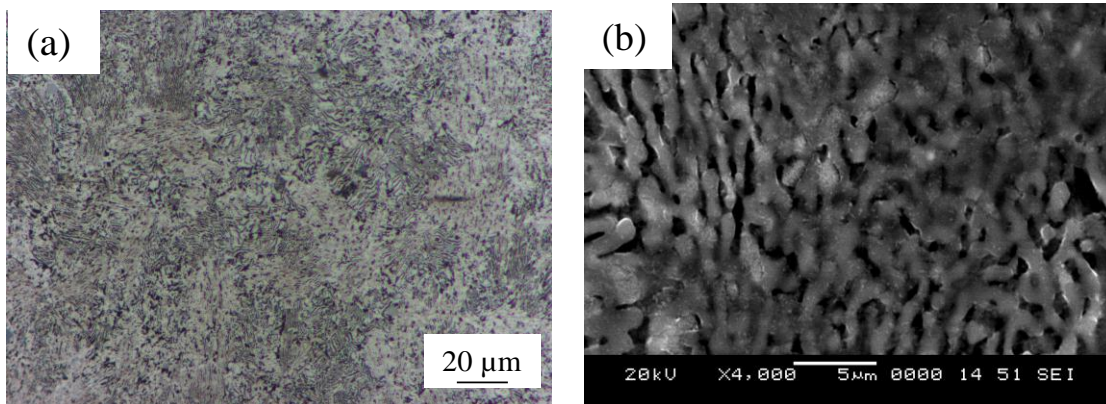


Figure 4.23 Multidirectional forged sample at 200 °C up to three passes and post aging at 100 °C for one hour (a) optical micrograph (500X Magnification) and (b) SEM micrograph (3% Nital etchant).

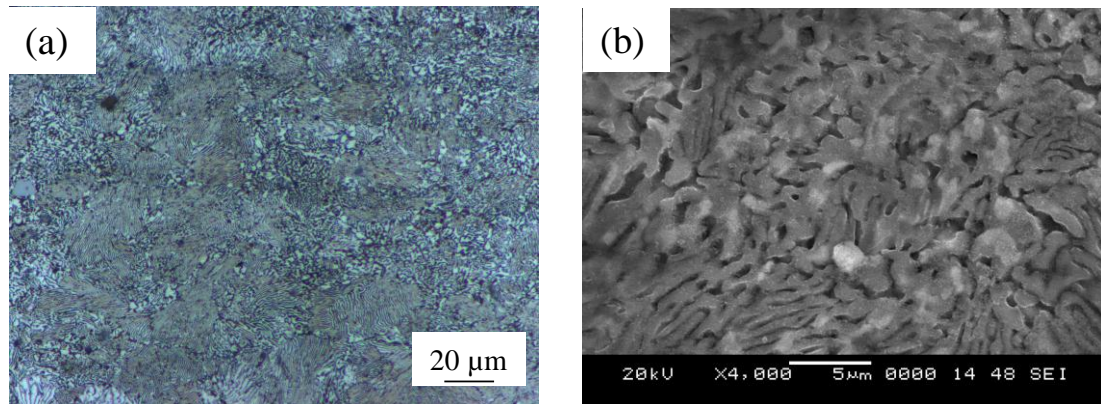


Figure 4.24 Multidirectional forged sample at 200 °C up to six passes and post aging at 100 °C for one hour (a) optical micrograph (500X Magnification) and (b) SEM micrograph (3% Nital etchant).

It is confirmed from the microstructural observations for post-aging of MDF processed sample that average grain size remains almost same as that of MDF processed material. Many of the elongated grains formed during MDF processing fragmented into fine grains. Figure 4.22 shows duplex type of microstructure with lamellar and nodular grains for MDF processed sample at 100 °C up to three passes. The microstructure of the MDF sample processed at 200 °C for three passes and other for six passes exhibits more uniformly distributed ϵ phase accompanied by breaking out of elongated grains into α and η phases as shown in Figure 4.23 and Figure 4.24.

4.4.3 Mechanical Properties

Figure 4.25 shows the hardness values of samples processed at different number of passes at different temperatures combined with aging of the MDF materials. Solutionized and aged sample show hardness value of 69 HRH. Post-aging of MDF sample show the hardness values of 74, 78 and 81 HRH at 100 °C up to three passes, 200 °C up to three and six passes respectively.

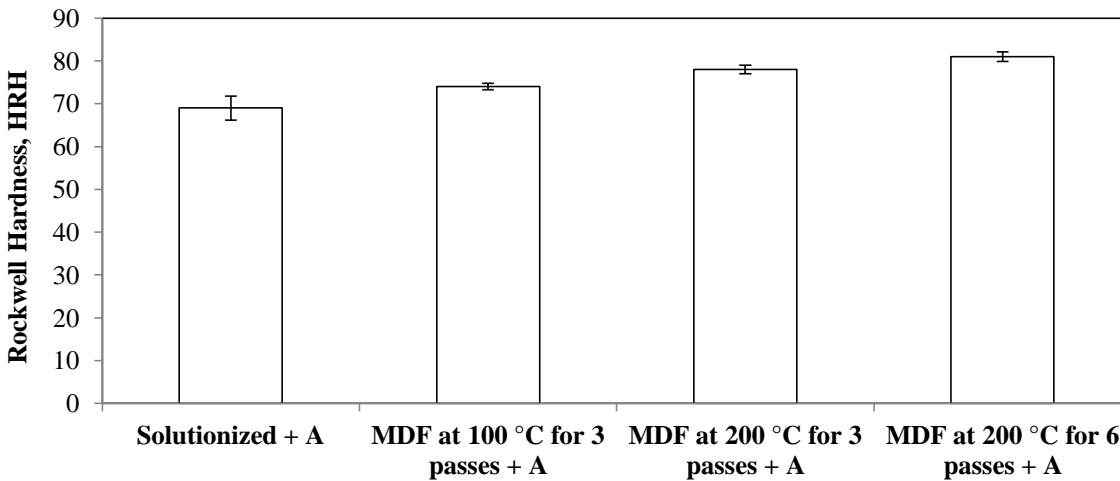


Figure 4.25 Bar chart showing Rockwell microhardness after MDF processed at 100 °C up to three passes and 200 °C up to three and six passes with aging.

Comparing with MDF processed material it could be inferred that aging of MDF material increased the hardness marginally. Sample MDF processed at 100 °C up to three passes register's hardness value of 71 HRH while the one aged at 100 °C for one hour registers the hardness value of 74 HRH. The hardness values of MDF processed and post-aged samples are slightly higher than those of MDF processed and non-aged ones. This small increase could be attributed to the fine precipitation and grain refinement achieved by application of MDF and subsequent aging. High density of lattice defects such as dislocations and grain boundaries generated by the SPD processing, accelerated atomic diffusion and thus enhanced precipitation kinetics (Lee et al. 2015). In the case of pure Zn recrystallization temperature is around 75 °C. By addition of small amounts of elements such as Al, Fe, Cu and Mg to pure Zn, recrystallization temperature has been improved (Farge, 1965). In the case of Zn-24Al-2Cu-0.005Cd-0.07Fe-0.02Mg alloy (ZA27 alloy), recrystallization temperature is approximately 240 °C but, small amount of recovery and grain growth may have occurred at an aging temperature of 100 °C in MDF processed material. It relieves the residual stresses which is the reason for not showing much higher hardness values as shown in Figure 4.25.

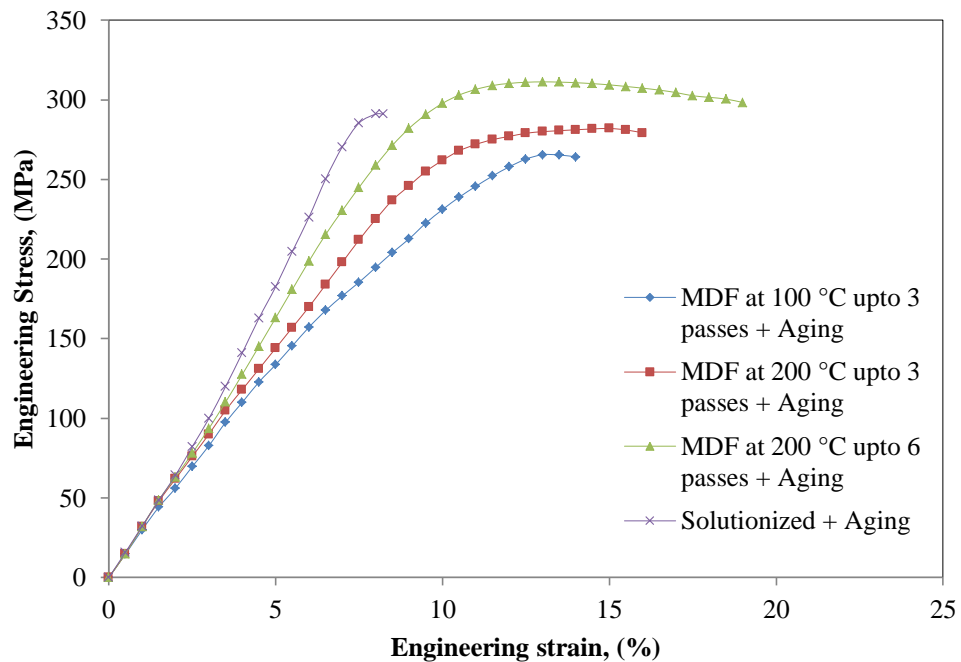


Figure 4.26 Engineering stress versus engineering strain graph from tensile test for solutionized and aging and after post-aging of MDF processed at 100 °C up to three passes and 200 °C up to three and six passes.

Figure 4.26 shows the engineering stress versus engineering strain curve for solutionized and aged sample and post-aged MDF sample for various processing conditions. Figure 4.27 shows the variation of ultimate tensile strength (UTS) and percentage of elongation. Initially, solutionized and aged sample shows UTS of 290 MPa and elongation of 8 %. From the MDF combined with post-aging, strength has been increased to 265.9 MPa by processing the sample at 100 °C up to three passes and increased further to 282.7 MPa and 311.2 MPa by processing the sample at 200 °C up to three and six passes with post-aging heat treatment. In addition, material processed at 200 °C up to six passes exhibits a high level of ductility to a value of 20 %. Comparing these values with those for MDF processed materials, it would be inferred the aging treatment resulted in large improvements in strength and maintaining good ductility level. Example: MDF processed at 200 °C up to six passes without post-aging show ultimate tensile strength of 276 MPa

and 21 % ductility. This aspect is important in the field of bearing application because the process of MDF combined with aging causes improvement in both strength and ductility. Because of grain refinement, bimodal structure and ϵ phase spread more uniformly through out the region.

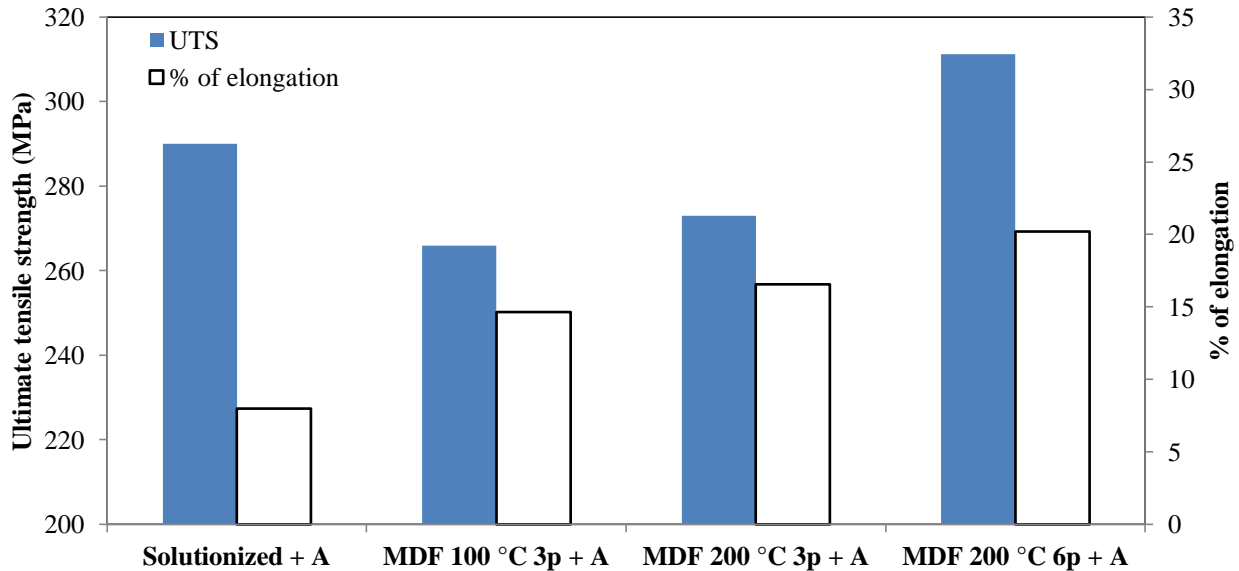


Figure 4.27 Bar chart showing ultimate tensile strength and percentage of elongation for solutionized and aged, MDF processed at 100 °C up to three passes and 200 °C up to three and six passes with aging.

Solutionized and aging at 100 °C for a one hour without MDF processing show high strength but poor ductility. It may be due to non-uniform distribution of α phase in the η phase matrix. In addition, copper rich ϵ phase being coarse and hard limits the ductility of the solutionized and aged sample. Comparing MDF processed samples with post-aging of MDF processed one at 200 °C for six passes there is an increase in the ultimate tensile strength by 11.3 %, maintaining good ductility. After aging, the microstructure was found to be an equiaxed and fine α phase surrounded by η phase. Further, the distribution of the ϵ phase over the grain boundaries of α phase resulted in high strength. Therefore, post-aging of the MDF specimens at 100 °C for one hour seems to have maintained the strength of the alloy along with good ductility.

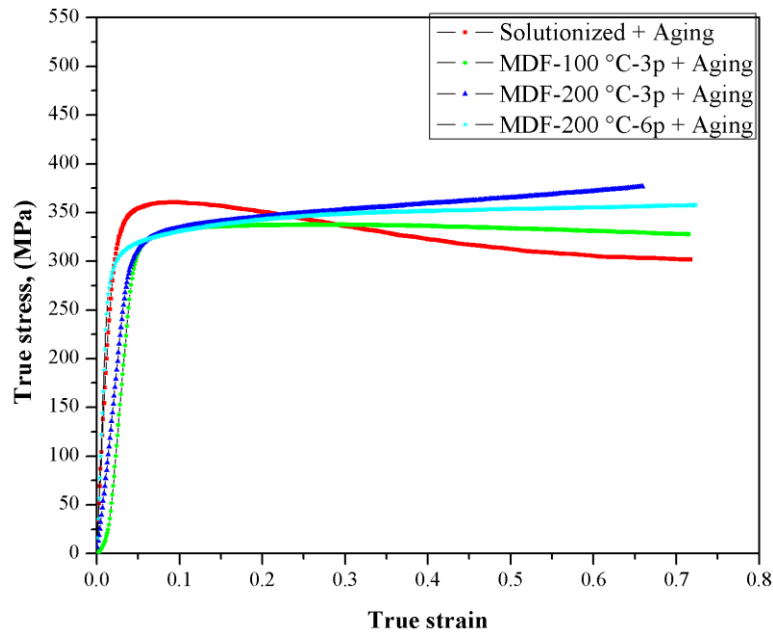


Figure 4.28 True stress versus true strain graph from compression test for solutionized and aging and after post-aging of MDF processed at 100 °C up to three passes and 200 °C up to three and six passes.

From the compression test, true stress versus true strain diagram of solutionized with aging and MDF processed material combined with aging were determined and presented in Table 4.2. Average values of the strength coefficient (K) and strain hardening exponent (n) for different processing condition with aging condition is presented in Figure 4.28. The strength coefficient (K) and strain hardening exponent (n) values were determined by fitting the curves to Power law equation and are presented in Figure 4.29. The value of K after solutionized and aging at 100 °C for one hour was 331.1MPa. For three passes of MDF sample at 100 °C with post-aging, the value of K was 380.3 MPa. After three passes at 200 °C with post-aging, K value was found to be 507 MPa. MDF up to six passes at 200 °C sample with post-aging resulted in K value to 603.5 MPa. The strain hardening exponent (n) values were 0.13, 0.16 and 0.24 for MDF processed samples at 100 °C up to three pass, 200 °C up to three and six passes along with post-aging respectively. The n value of solutionized and aged sample was 0.08. The n value is much higher for 200 °C MDF processing up to six passes with post-aging

sample when compared to MDF processing at 100 °C up to three passes with post-aging sample. This suggests more extensive recovery after deformation at 200 °C to the higher number of passes compared to 100 °C for lesser number of passes. The strain hardening exponent value indicated that solutionized and aged sample is having less ductility. MDF processing at 200 °C up to six passes showed n value in the order of 0.24, which is high as compared to all the other MDF processed samples.

Table 4.2 Strength coefficient (K) and strain hardening exponent (n) values for various processing with aging conditions.

Processing condition	Strain hardening exponent (n)		Strength coefficient (K), MPa	
	Values	Mean	Values	Mean
Solutionized + Aging	0.07	0.08	318.53	331.1
	0.09		338.62	
	0.08		336.12	
MDF-100 °C-3 pass + Aging	0.15	0.13	389.45	380.3
	0.11		367.54	
	0.13		383.83	
MDF-200 °C-3 pass + Aging	0.15	0.16	494.19	507.0
	0.17		512.09	
	0.18		514.75	
MDF-200 °C-6 pass + Aging	0.25	0.24	592.34	603.5
	0.24		615.65	
	0.24		602.56	

These n and K values are important in sheet metal forming and it is also the measure of increase in hardness and strength caused by plastic deformation. It is believed that the ductility of a material increases with increase in the strain hardening exponent (n) value and so does the resistance to neck formation. This co-relation can be observed by comparing the variation in ‘n’ values with engineering stress-strain curves presented in

Figure 4.26 in the current investigation. The ductility increases with increasing number of MDF passes.

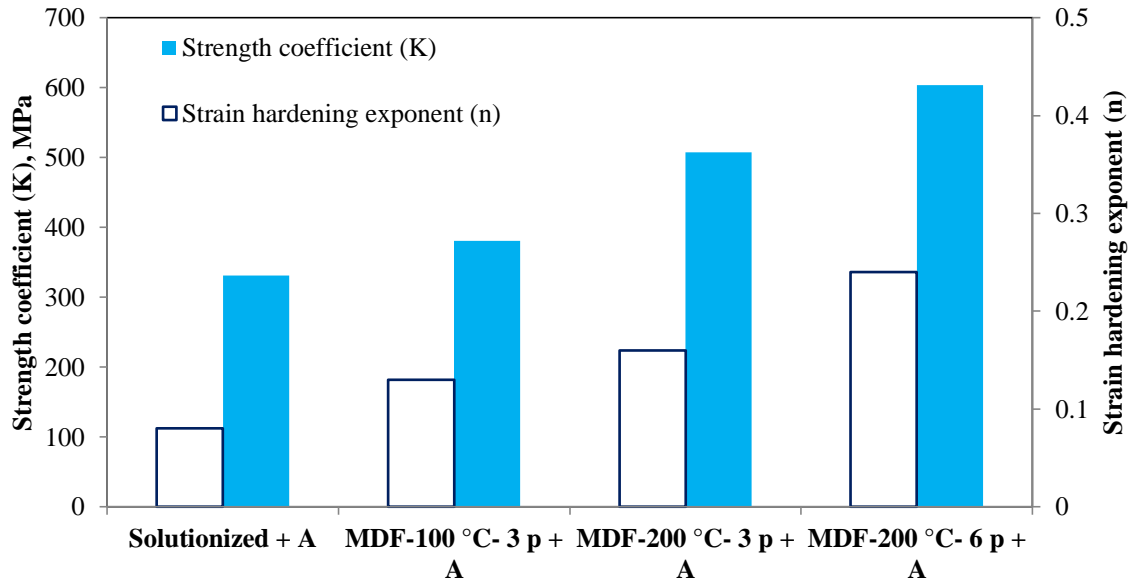


Figure 4.29 Strength co-efficient (K) and strain hardening exponent (n) obtained from compression test for solutionized and aging at 100 °C for one hour, MDF processed at 100 °C up to three passes with post-aging and 200 °C up to three and six passes with post-aging.

The improvement in strength and ductility with decreasing grain size has been established in Table 4.3. The highest strength with good ductility have been achieved for MDF processed at 200 °C for six passes material combined with post-aging at low temperature of 100 °C for a shorter period of one hour. As observed from the SEM images in Figure 4.24 (b), α and η phases were well distributed along with finer ϵ phase which leads to increased strength and higher ductility.

Table 4.3 Ultimate tensile strength, ductility and average grain size for various processing conditions.

Processing condition	Average grain size (μm)	Ductility (%)	Ultimate tensile strength (MPa)
Solutionized	30	13.5	185
Solutionized + aging at 100 °C for one hour	30.2	8	290
MDF at 100 °C up to 3 passes	2	14	267
MDF at 200 °C up to 3 passes	1.5	14	272
MDF at 200 °C up to 6 passes	1	21	276
MDF at 100 °C for 3 passes + Aging at 100 °C for one hour	2.3	15	266
MDF at 200 °C for 3 passes + Aging at 100 °C for one hour	1.7	17	273
MDF at 200 °C for 6 passes + Aging at 100 °C for one hour	1.2	20	311

4.4.4 Fractography

The images of the samples fractured under tensile mode for solutionized and aged at 100 °C for one hour are shown in Figure 4.30 (a). It predominantly illustrates the brittle mode of fracture which occurred due to the presence of globular like ϵ particles precipitated over the grain boundaries. It may be the origin for the micro crack formation and leads to lower elongation for solutionized and aged sample. If adhesion between the ϵ particles and grain boundary is good and if ϵ particle is not weak and brittle, the mode of fracture will not be brittle. Fractured images of MDF sample at 100 °C up to three passes with

post-aging is shown in Figure 4.30 (b) which is consisting of dimples. After 0.6-1.2 strain, MDF processed at 200 °C up to three passes and six passes with post-aging sample shows many dimples. These dimples refined into much finer dimples with increased number of passes and ductile mode of fracture are seen in Figure 4.30 (c) and (d). Once again, it drives a point that the studies on the fracture surface corroborate the studies on the mechanical properties which had indicated that processing by MDF and post-aging improves the ductility of the materials to a large extent.

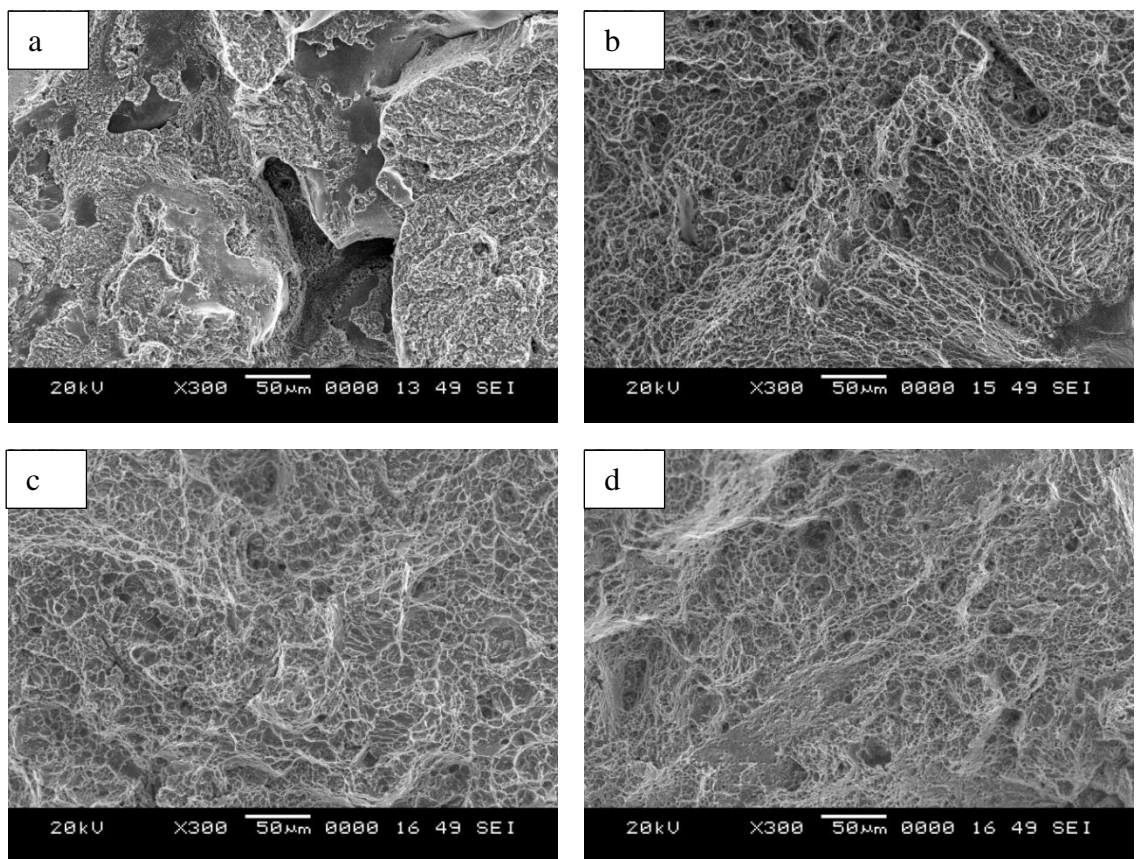


Figure 4.30 SEM images of the surface of alloy fractured under tensile mode in (a) solutionized and aging at 100 °C for one hour (b) MDF at 100 °C up to three passes with post-aging (c) MDF at 200 °C up to three passes with post-aging and (d) MDF at 200 °C up to six passes with post-aging.

4.5 Formation of Fine-Grained Structure by MDF Process: TEM Studies

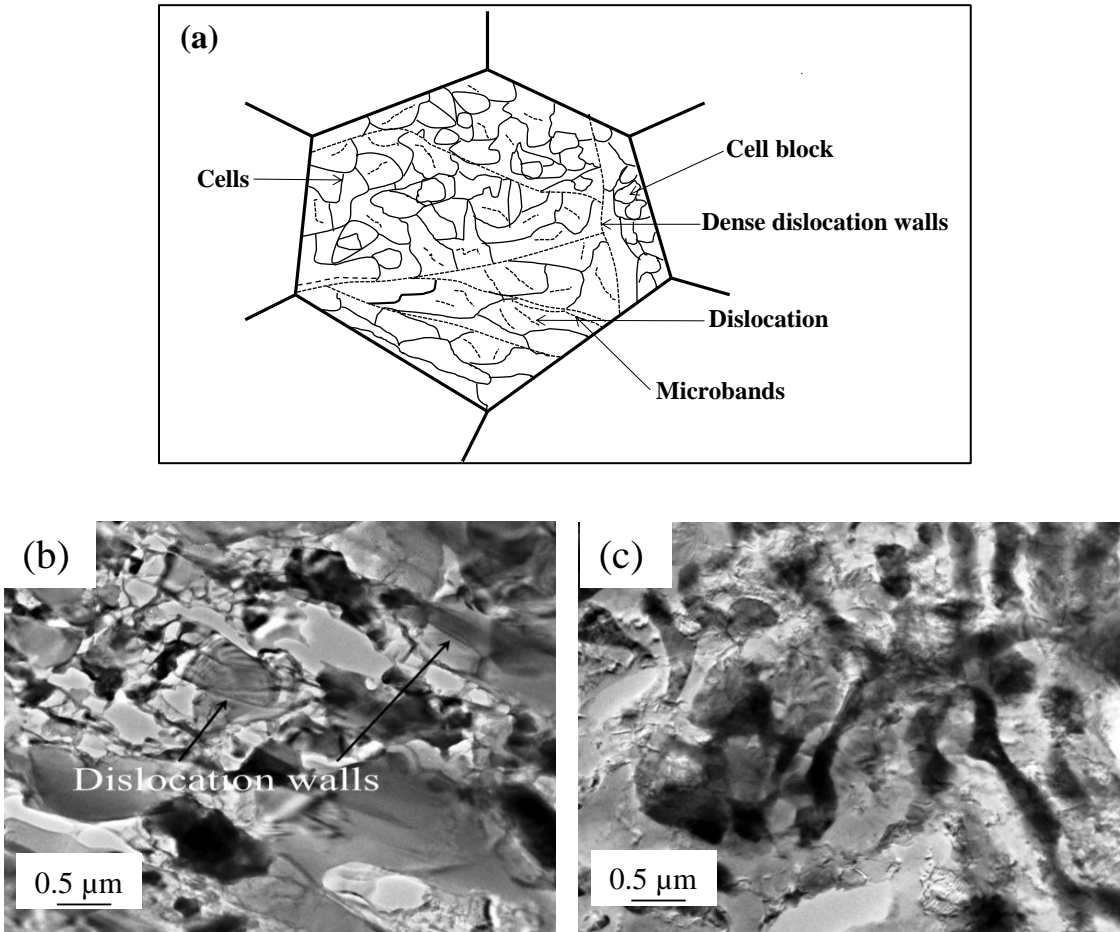


Figure 4.31 (a) Schematic view of deformed structure, (b) TEM micrograph of MDF at 100 °C up to three passes and (c) TEM micrograph of MDF at 200 °C up to three passes.

Processing of Zn-24Al-2Cu alloy material by multi directional forging at a moderately low temperature introduces dislocation substructure in the grain interiors. During the early stages of deformation, high densities of dislocations are introduced into the material which forms the cellular substructure. Cell blocks are evolved from dislocation cells, which are earlier formed by subdivision of dense dislocation walls (DDW) which is schematically shown in Figure 4.31 (a). TEM micrograph of grain subdivision and

formation of cell blocks in MDF processed material at 100 °C up to three passes and MDF processed material at 200 °C up to three passes with a total equivalent strain of 0.6 are displayed in Figure 4.31 (b) and (c). These dislocation sub-boundaries are having larger misorientations than initial cell walls. By further increase in strain during later stages, deformation bands form with higher misorientations. Original coarse grains are subdivided into smaller and heavily misoriented fractions of grains by the applications of huge amount of total equivalent strain into the material.

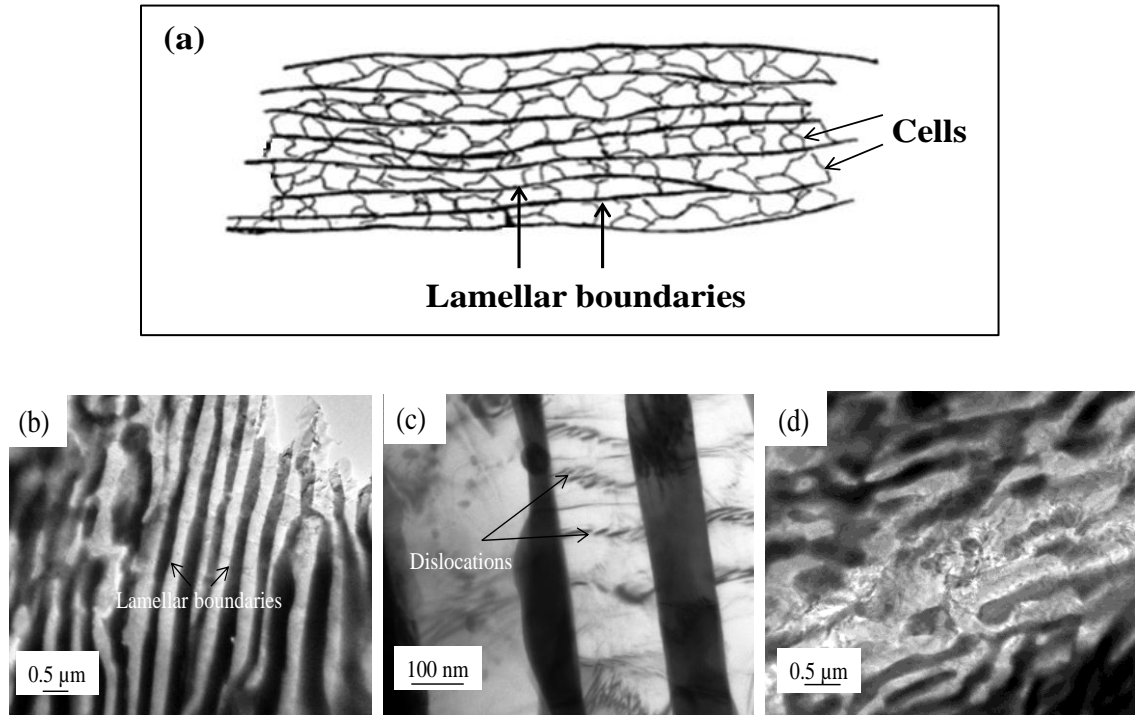


Figure 4.32 (a) Schematic representation of lamellar boundaries (b) TEM micrograph of MDF at 200 °C up to six passes and (c) enlarged image of (b) showing grain subdivision at large strain (d) TEM micrograph of MDF at 200 °C up to six passes with aging.

The schematic representation of lamellar grain boundaries with cells are shown in Figure 4.32 (a). TEM micrograph of MDF processed material at 200 °C up to six passes with total equivalent strain of 1.2 is presented in Figure 4.32 (b) and enlarged image of processed sample showing grain subdivision at higher magnification is presented in Figure 4.32 (c). TEM micrograph of MDF processed material at 200 °C up to six passes with aging is shown in Figure 4.32 (d). It shows that dense dislocations are entangled with each other inside the Al rich phase.

4.6 Impression Creep Behavior of Zn-24Al-2Cu

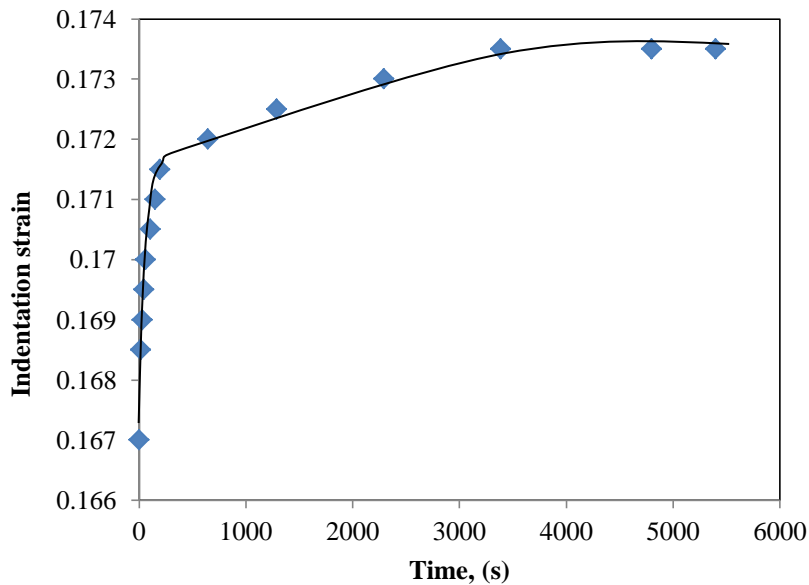
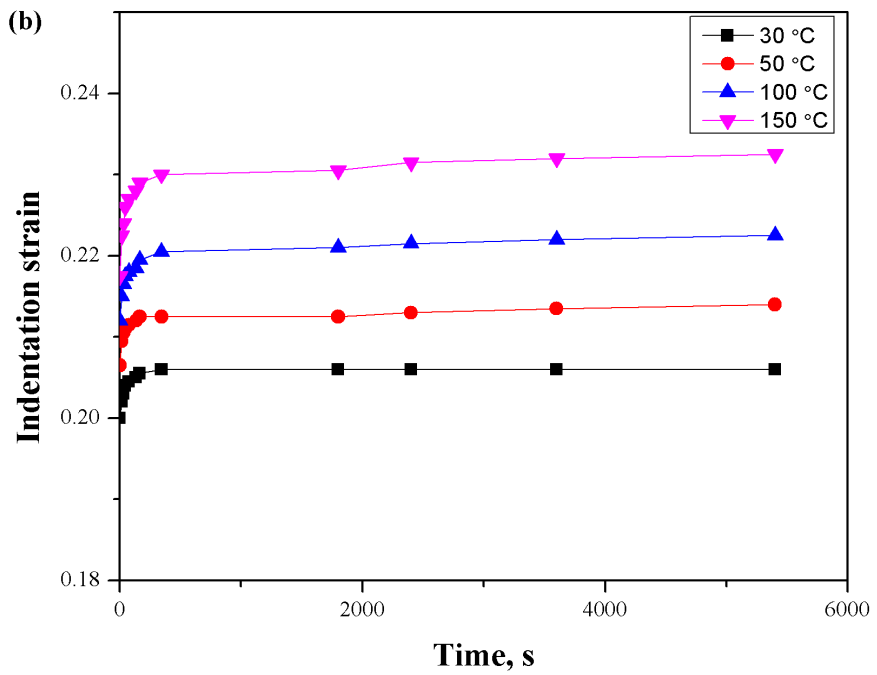
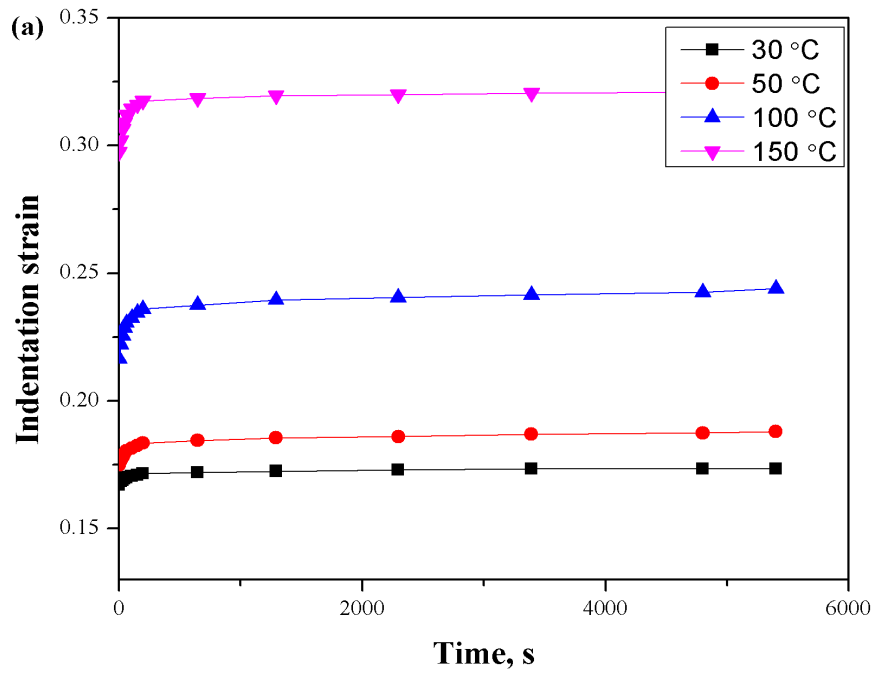


Figure 4.33 Typical impression creep curves of the materials tested under constant load of 2 kg at 30 °C for solutionized sample.

Impression creep testing was carried out on the samples using 2 mm diameter cylindrical tungsten carbide indenter. Tests were carried out at 30, 50, 100 and 150 °C with normal load of 2 kg and 2.5 kg. Figure 4.33 displays typical creep curve expressed as indentation strain versus dwell time at the testing temperature of 30 °C under load of 2 kg for solutionized material. Impression creep strain (ϵ) is obtained for each curve at different instants of time, following the approach presented by Sastry (2005).

Various stages in creep were identified and steady state creep rate (SSCR) values were calculated by finding slope of the straight line which was observed in secondary stage of creep.



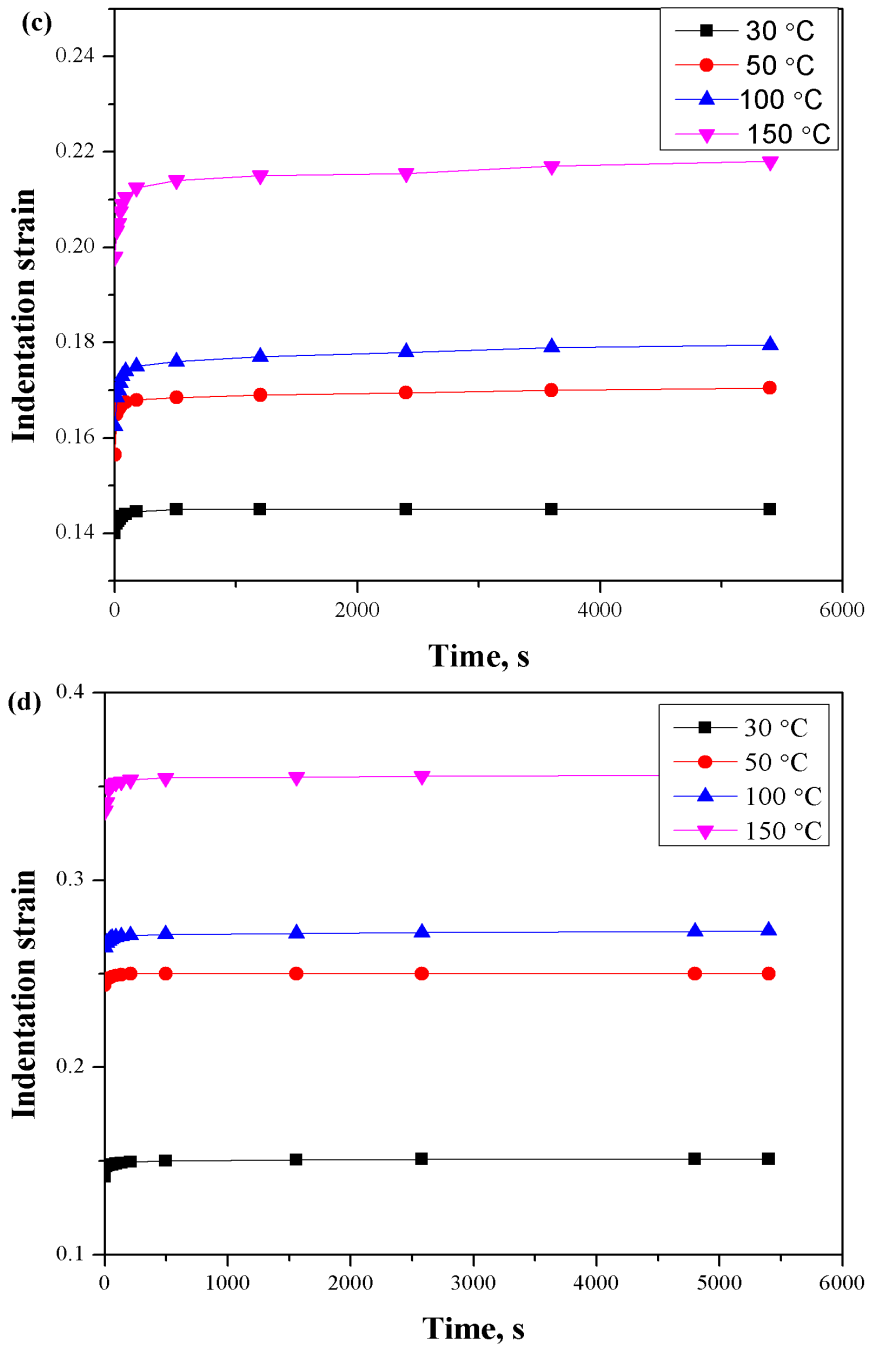
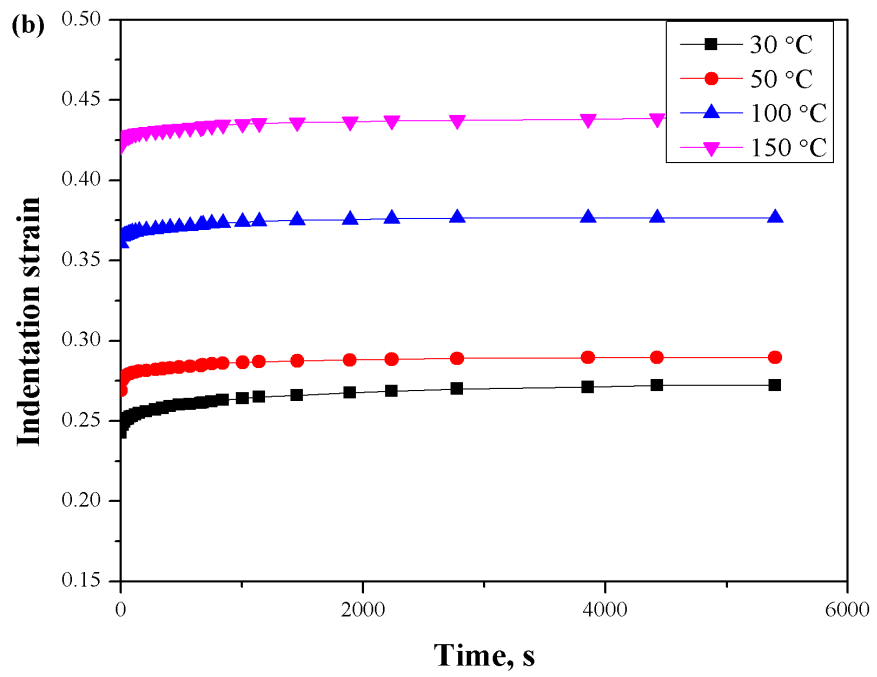
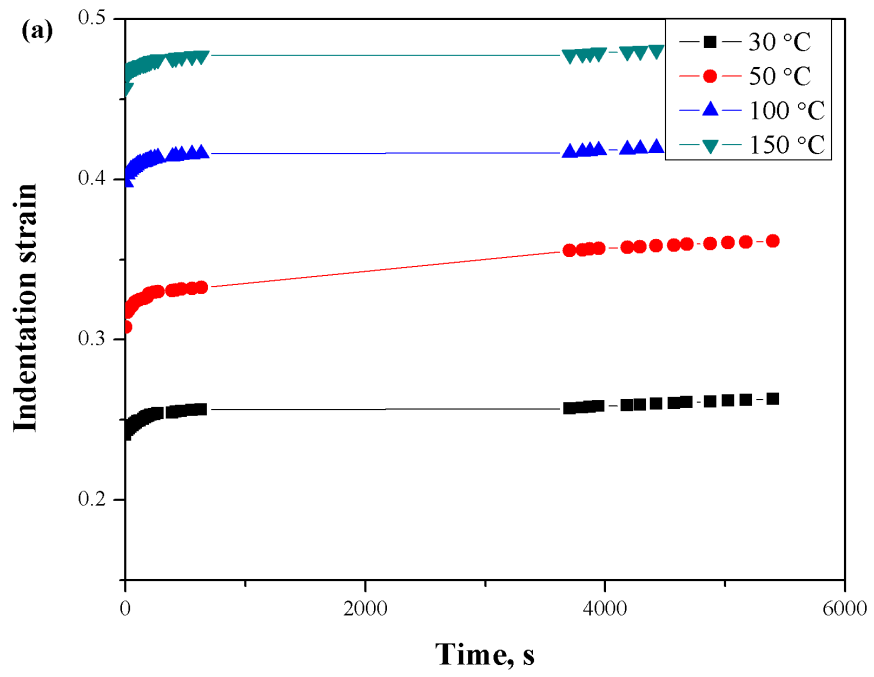


Figure 4.34 Typical impression creep curves of the materials tested under constant load of 2 kg and different temperatures from 30 to 150 °C: (a) Solutionized (b) MDF at 100 °C for three passes (c) MDF at 200 °C for three passes and (d) MDF at 200 °C for six passes.



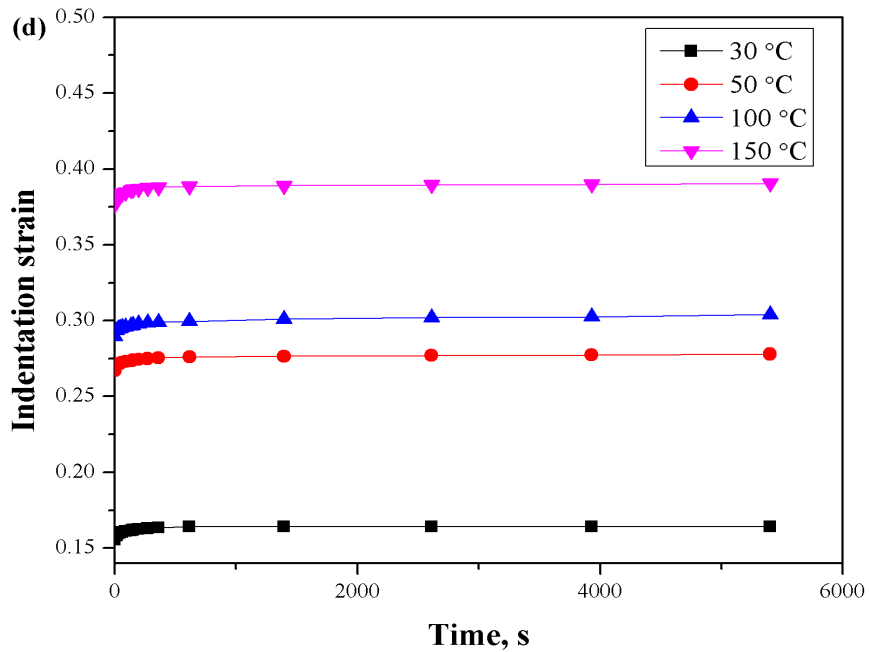
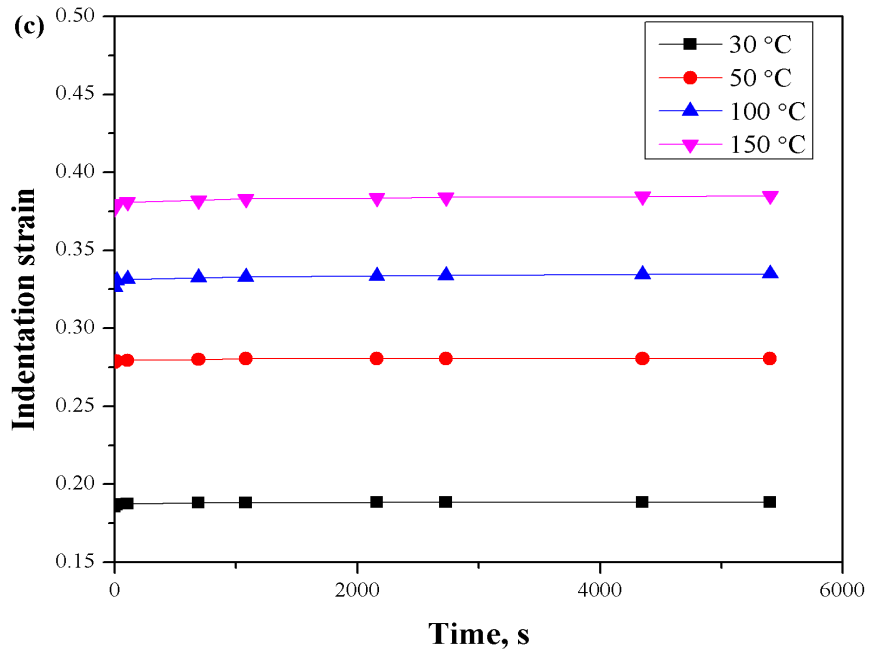


Figure 4.35 Typical impression creep curves of the materials tested under constant load of 2.5 kg and different temperatures from 30 to 150 °C: (a) Solutionized (b) MDF at 100 °C for three passes (c) MDF at 200 °C for three passes and (d) MDF at 200 °C for six passes.

Figure 4.34 and Figure 4.35 show the creep curves for solutionized and MDF processed samples at 2 kg and 2.5 kg respectively. Instantaneous strain increased as creep testing temperature increased in all the cases. It records the fact that the higher the creep testing temperature greater is the steady state creep rate.

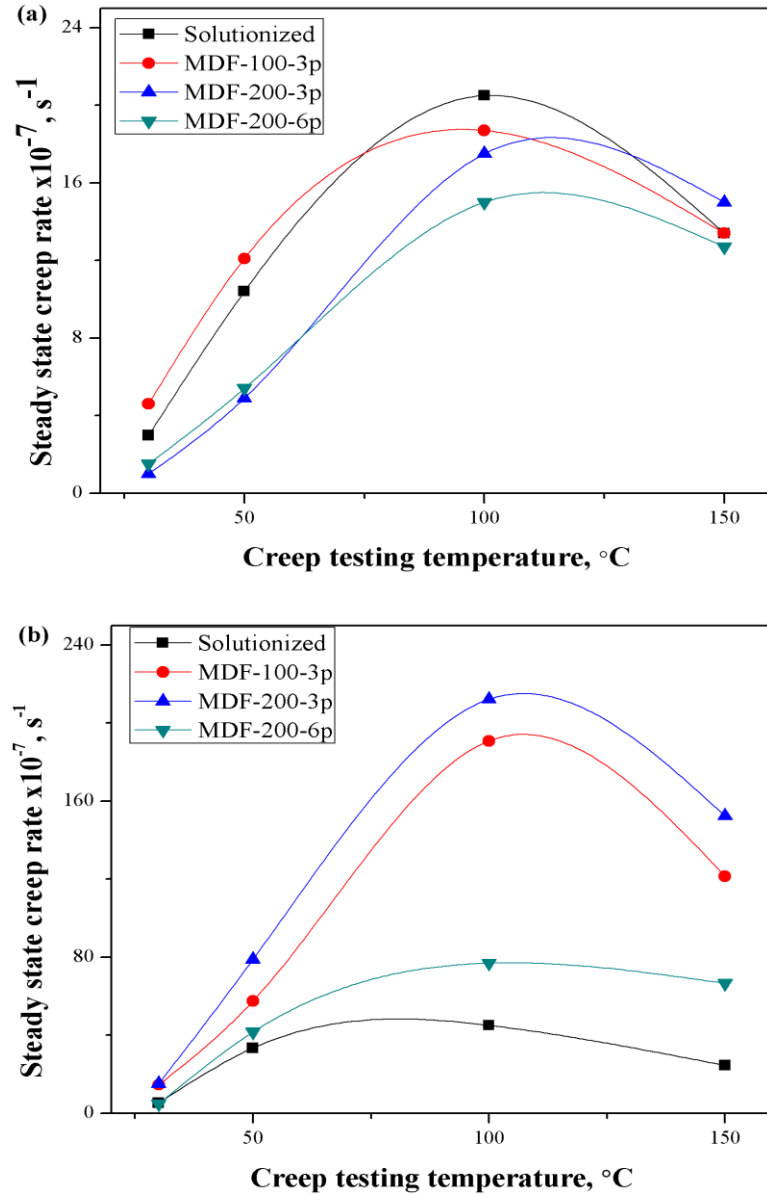


Figure 4.36 Comparison of steady state creep rate obtained at different temperatures for the materials tested at: (a) 2 kg load and (b) 2.5 kg load.

The values of SSCR are estimated at different temperatures for both solutionized and MDF processed samples for 2 kg and 2.5 kg load and these values are presented in Figure 4.36 (a) and (b) respectively. MDF processed material at 200 °C for six passes exhibited the highest creep resistance. For all the processed and unprocessed conditions, the creep resistance decreases or steady state creep rate increases as temperature is increased up to 100 °C.

The following significant observations are listed out from the Figure 4.36

- i. SSCR values are not sensitive to microstructural features if tested at 30 °C and 150 °C with 2 kg load. However, if material is tested with 2.5 kg load at temperature above 30 °C, the SSCR values are observed to be sensitive to the microstructural features.
- ii. In all the cases, the creep rate increases to a maximum at the testing temperature of 100 °C then start decreasing.
- iii. The MDF processed material at 200 °C for six passes experience least creep rate followed by those MDF processed at 100 °C and 200 °C for three passes.

4.6.1 Stress Exponent

The stress exponent values (n) were determined according to Equation 3.4. The temperature dependency of the stress exponent for the solutionized and MDF processed samples are presented in Table 4.4.

Table 4.4 Variations of stress exponent with temperature for different processing conditions.

Creep testing temperature	Stress exponent values (n)			
	30 °C	50 °C	100 °C	150 °C
Solutionized	2.5	5.2	3.5	2.7
MDF-100 °C -3 pass	5.1	7.0	10.4	9.9
MDF-200 °C -3 pass	12.1	12.4	11.2	10.4
MDF-200 °C -6 pass	5.0	9.1	7.3	7.4

The stress exponent (n) values of the solutionized and MDF processed materials are observed to be in the range of 2.5-12.4. In all the cases, n values are almost maintained constant if creep testing is carried out above 100 °C. The observed discrepancies in the n values are explained with the help of threshold stress in the Zn-24Al-2Cu alloys in section 4.6.3.

4.6.2 Apparent Activation Energy

The apparent activation energy was calculated by plotting strain rate ($\dot{\epsilon}$) versus (1/T) using a semi-logarithmic scales at different stresses. The apparent activation energy is obtained from the slope of the data points, which is equal to $(-Q_a/R)$ and tabulated in Table 4.5.

Table 4.5 Apparent activation energy (Q_a) values.

Load	Apparent activation energy (Q_a) kJ/mol	
	2 kg	2.5 kg
Solutionized	12.6	11.1
MDF-100 °C -3pass	8.7	18.8
MDF-200 °C -3pass	13.1	19.0
MDF-200 °C -6pass	17.8	20.1

4.6.3 Threshold Stress

The stress exponent (n) from Table 4.4 has a value of 2.5 to 12.4. This large value of n for the present alloy is higher than what is usually reported for binary Zn-Al alloys (n = 2 or 5) at similar temperatures and stresses (Gobien et al., 2010, Alibabaie and Mahmudi 2012). In power law creep, stress exponent can range from 1 to 5. If the stress exponent increases significantly above 5 i.e., 12.4 as in the present case, the effect of threshold stress on the creep behavior of the material has to be introduced. Threshold stresses are most often seen where an intentional or unintentional dispersion of precipitates or oxides are observed (Xun et al., 2005 and Chauhan et al., 2005). The dominant active creep mechanism is influenced by the way in which the dispersion affects the apparent stress exponent. Significant number of fractions of the grains are contributing to strong threshold stress effects as seen in the present creep data. A second

possibility which could cause an interference with the sources and sinks of vacancies leading to the threshold stress behavior is non-uniform solute segregation. If the Al is being forced into solid solution during the solutionizing heat treatment process, it is possible that solute atoms surrounding the grain boundaries are interfering with vacancy production and transportation which drive the strain as a result of diffusion creep mechanisms.

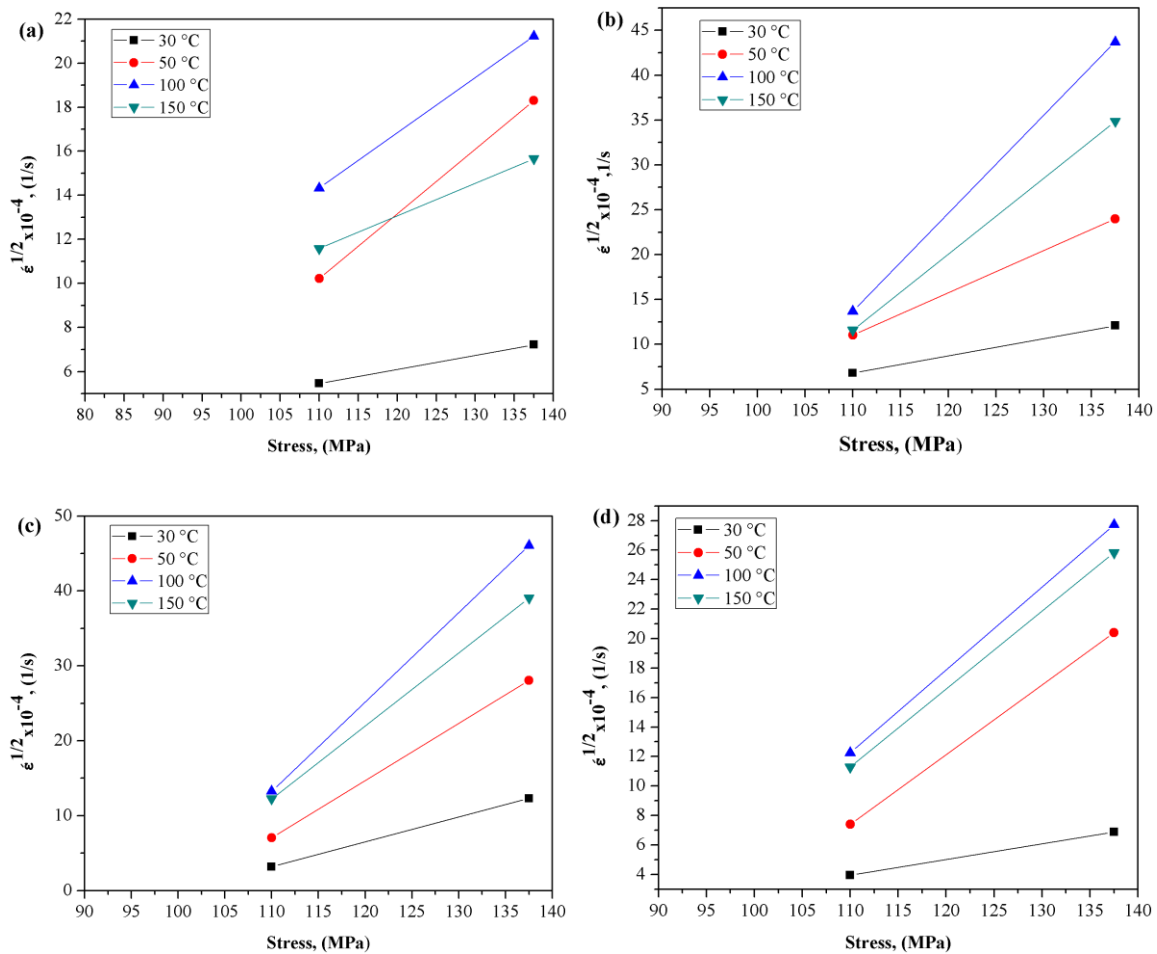


Figure 4.37 Double linear plot for $\dot{\epsilon}^{1/2}$ versus stress at different temperatures (a) solutionized (b) MDF at 100 °C up to three passes (c) MDF at 200 °C up to three passes and (d) MDF at 200 °C up to six passes.

Presence of threshold stress could be the reason for higher values of stress exponent n. Interaction of dislocation with second phase particles as observed in TEM images

indicates the existence of threshold stress, explained in section 4.6.5. The value of threshold stress at the given temperature is explored by plotting strain rate ($\dot{\epsilon}^{1/n}$) versus stress (σ). Regression analysis found that n value of 2 yielded the best fit of the data. This is explored by plotting $\dot{\epsilon}^{1/2}$ versus stress (σ) using a double linear scale as shown in Figure 4.37. The data points for each temperature fall on a segment of the straight line and extrapolation of this line to zero strain rate gives the value of threshold stress (σ_0). It is represented in Table 4.6.

Table 4.6 Threshold stress (σ_0) values.

	Average threshold stress (MPa)
Solutionized	45
MDF-100 °C -3pass	88.5
MDF-200 °C -3pass	99
MDF-200 °C -6pass	85.9

The present results along with previous studies (Yong et al., 1997, Chaudhury and Mohamed 1988) suggest that threshold stress, σ_0 is a function of temperature. The temperature dependence of the normalized threshold stress (σ_0/E) is shown in Figure 4.38 for solutionized sample. This dependence can be expressed as,

$$\frac{\sigma_0}{E} = B_0 \exp\left(\frac{Q_0}{RT}\right) \quad \text{Equation 4.2}$$

Taking logarithm,

$$\ln\left(\frac{\sigma_0}{E}\right) = \frac{Q_0}{RT} + \ln(B_0) \quad \text{Equation 4.3}$$

Where B_0 = constant, Q_0 = activation energy term associated with the binding energy between the dislocations and the obstacles, E = elastic modulus.

For the present materials, the temperature dependence of the elastic modulus of pure Zn was used. This has been proposed to be obtained from the following Equation 4.4 (Frost and Ashby, 1982).

$$E = 60,000 - 35.58 T \quad \text{Equation 4.4}$$

By plotting $\log\left(\frac{\sigma_0}{E}\right)$ versus $\left(\frac{1}{T}\right)$, the slope of this curve gives Q_0 . The values of the activation energy from threshold stress for solutionized, MDF processed at 100 °C up to three passes, 200 °C up to three and six passes are 5.3, 1.8, 0.2 and 0.8 kJ/mol respectively. This behavior is similar to that observed in Al alloys processed by powder metallurgy technique (Mohamed 1998). The stress exponent (n) is calculated by using the effective stress $(\sigma-\sigma_0)$, it is inferred that n values are being close to 2. It is represented in Table 4.7.

Table 4.7 Variations of the stress exponent by considering effective stress.

Creep testing temperature	Stress exponent values (n) by considering effective stress			
	30 °C	50 °C	100 °C	150 °C
Solutionized	1.6	3.3	2.2	1.7
MDF-100 °C -3 pass	1.4	1.9	2.8	2.7
MDF-200 °C -3 pass	2.2	2.2	2.0	1.8
MDF-200 °C -6 pass	1.5	2.7	2.1	2.2

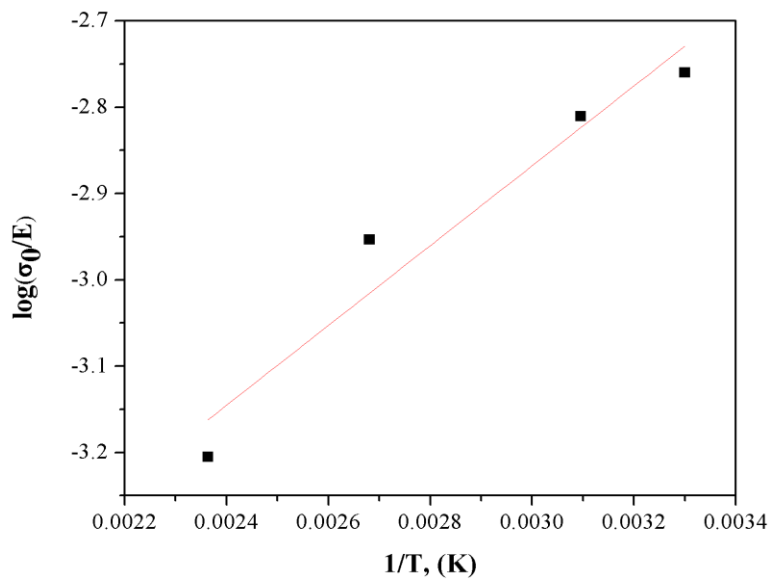


Figure 4.38 Semi-logarithmic plot for normalized threshold stress (σ_0/E) versus reciprocal of absolute temperature for solutionized sample.

4.6.4 True Activation Energy and Creep Mechanism

Under the presence of threshold stress, the applied stress (σ) is replaced by an effective stress ($\sigma - \sigma_0$). Apparent activation energy (Q_a) must be modified to reveal the true activation energy (Q_t) using the following Equation 4.5,

$$Q_t = Q_a \frac{n Q_0}{\left(\frac{\sigma}{\sigma_0} - 1\right)} \quad \text{Equation 4.5}$$

Using the experimental data previously described apparent activation energy, threshold stress and threshold activation energy are used for calculating true activation energy. The calculated true activation energy for solutionized and MDF processed sample obtained for the data corresponding to stress exponent $n = 2$ is presented in Table 4.8.

Table 4.8 True activation energy (Q_t) values.

Load, Kg	True activation energy (Q_t) values in kJ/mol			
	Solutionized	MDF-100-3p	MDF-200-3p	MDF-200-6p
2	92	129	54	103
2.5	57	122	22	54

The true activation energy values for solutionized and MDF processed materials are in the range of 22 to 129 kJ/mol. It should be noted that, true activation energy values determined for solutionized material are in the range of 92 kJ/mol which compare well with the lattice diffusion of Zn ($Q = 91.7$ kJ/mol). The lower activation energy 57 kJ/mol with an applied load of 2.5 kg may imply that another mechanism parallel to lattice diffusion controlled dislocation climb is operative. Similar type of observation is recorded for binary Zn-Al alloys by Alibabaie and Mahmudi (2012).

The true activation energy (Q_t) values are determined for MDF processed materials and they are represented as, (i) MDF processed material at 100 °C up to three passes are having Q_t in the range of 122 to 129 kJ/mol which is somewhere close to the values of lattice self-diffusion activation energies in pure Al, ($Q = 143$ kJ/mol as measured by Arieli and Mukherjee (1980)). (ii) MDF at 200 °C up to three passes is having average true activation energy of 54 to 22 kJ/mol which is somewhat low value compared to that

of the activation energy for grain boundary diffusion in pure Zn of 60 kJ/mol as found by Frost and Ashby (1982). (iii) MDF at 200 °C up to six passes shows 54 to 103 kJ/mol which suggest that lattice diffusion controlled dislocation climb is the possible mechanism of creep taking into consideration of stress exponent (n) greater than 5. For all the unprocessed and processed materials it is observed that activation energy decreases as applied load increases.

From these results, it is possible to say that the different creep behaviors for Zn-24Al-2Cu alloy with different grain sizes are related to changes in the diffusion mechanisms associated with the change in the grain size of the deformed samples. Tiny, dense and dispersed copper rich ϵ phase in the η matrix improves the strength of the Zn-Al based alloy (Durman and Murphy, 1997). This strengthening weakens as the decomposition of the ϵ phase is encouraged in the processed alloys with higher Al contents. Furthermore, the phase boundaries in the eutectic or eutectoid structures and the refined structures, which provide hardening at low temperatures, can also give rise to grain boundary sliding at high temperatures, and thus causing softening. The combination of these two effects is thought to be the main reason for the lower creep resistance of the alloys with sample processed by MDF at 200 °C for six passes.

4.6.5 Microstructural Characterization: TEM Studies

The TEM images of the microstructure of the MDF at 100 °C up to three pass sample and MDF at 200 °C up to six pass samples are shown in Figure 4.39. The X-Ray diffraction patterns of the alloys after creep test at 150 °C are presented in Figure 4.40. It reveals that α , η and ϵ phases are present in solutionized and heat treated samples. After creep test on solutionized and MDF processed samples, intensity of peak of ϵ -phase appears to be slightly decreasing while the intensity of τ' phase shows noticeable increase.

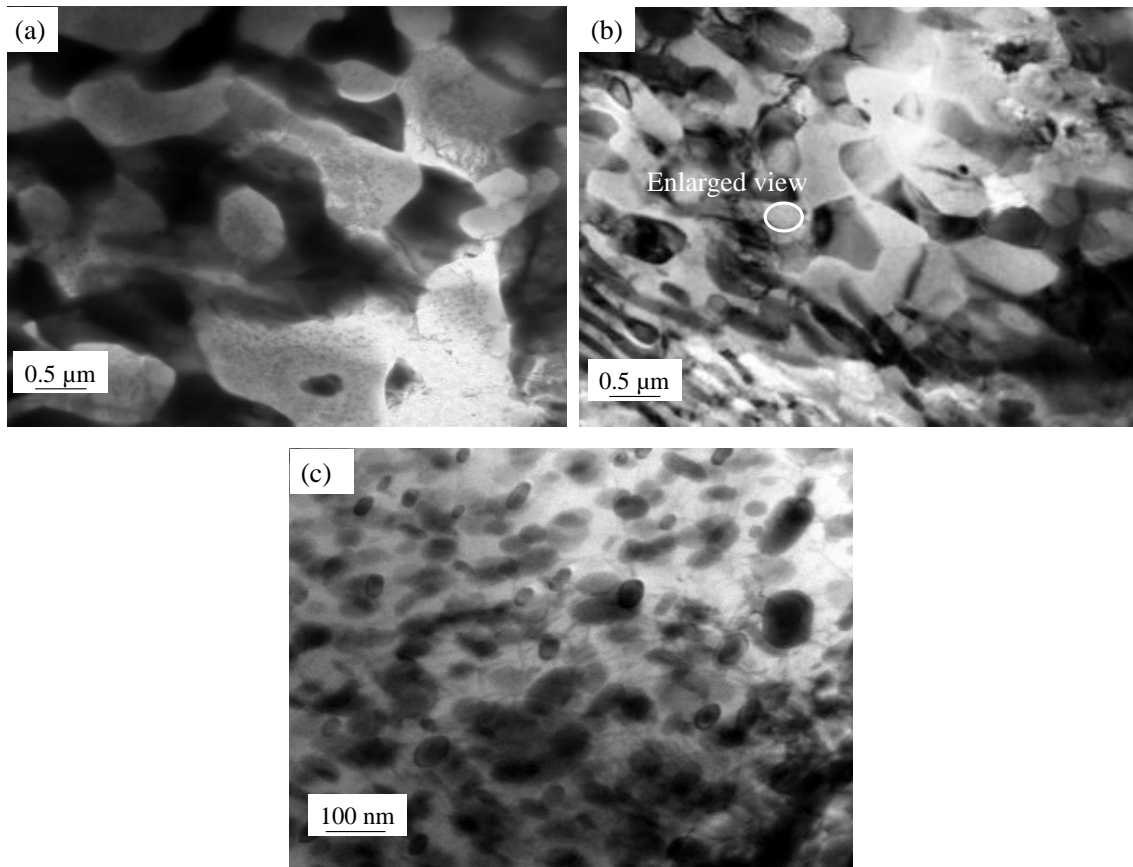


Figure 4.39 Bright field TEM micrograph of (a) MDF at 100 °C for three passes (b) MDF at 200 °C for six passes reveals a large number of dislocations and (c) images showing nano-crystalline dispersion particles inside the α phase shown in (b).

Since mechanical properties are in close relation with the microstructure of the alloys, the influence of MDF process at different temperatures and number of passes on the creep resistance of the tested alloys are visible from their respective microstructures. In the present work, solutionized material contains an average grain size of 30 μm . MDF of solutionized sample at 100 °C for three passes resulted in a material with an average grain size of 2 μm and when samples were further processed at 200 °C for six passes, the average grain size was reduced to 1 μm . TEM micrographs of the alloys, as shown in Figure 4.39 consist of α -Al rich phase, η -Zn rich phase and intermetallic compound ϵ (CuZn_4) phases.

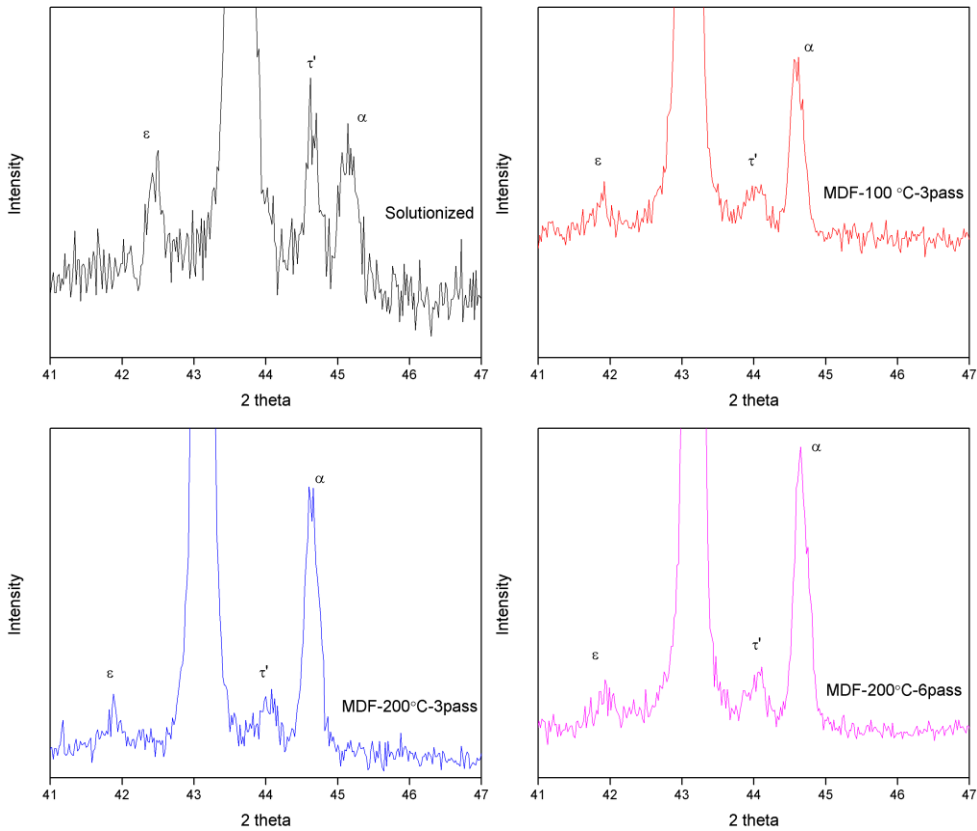
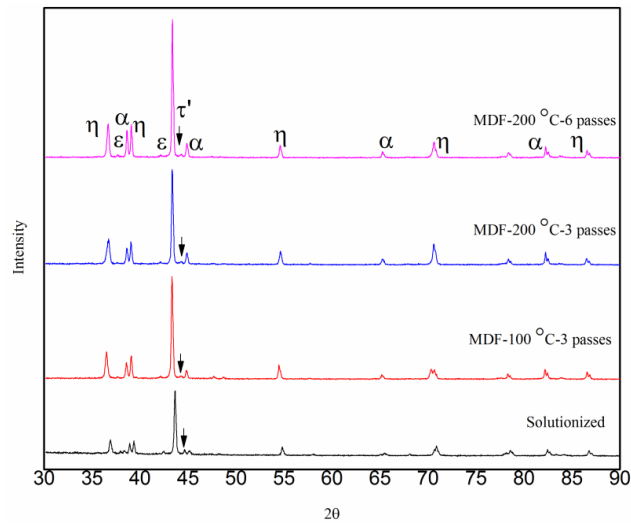


Figure 4.40 X-Ray diffraction patterns of the different processed conditions after creep test at 150 °C; enlarged view showing τ' phase peak.

The X-Ray diffraction patterns of the alloys after creep test at 150 °C are presented in Figure 4.40. It reveals that α , η and ϵ phases are present in solutionized heat treated

samples. After creep testing on solutionized and MDF processed samples, it is observed that intensity of ϵ -phase appears to be slightly decreased while the intensity of τ' phase shows noticeable increase. This implies that the ϵ phase decomposed during the creep test by the phase transformation to τ' phase by following reaction: $\alpha + \epsilon \rightarrow \tau' + \eta$. It is anticipated that the imposed stress on specimen during prolonged creep deformation at higher temperature has led to the faster decomposition of the ϵ phase, resulting in higher amounts of the τ' phase, as indicated by higher intensities of the relevant peaks in the XRD patterns. For these reasons the creep resistance recorded at temperature 150 °C is better than that of 100 °C. The fine precipitates at a higher temperature of testing inhibit the movement of dislocation there by changing the mechanism of creep. This kind of phase transformation has been also observed previously in the specimens of eutectoid Zn-Al based alloys subjected to various thermal processes, such as tensile and creep tests (Zhu 2001).

4.7 Dry Sliding Wear Test

Dry sliding wear test was carried out by using a pin-on-disc machine on solutionized, aged, MDF processed and MDF processed combined with aging samples and they are explained in the following sections.

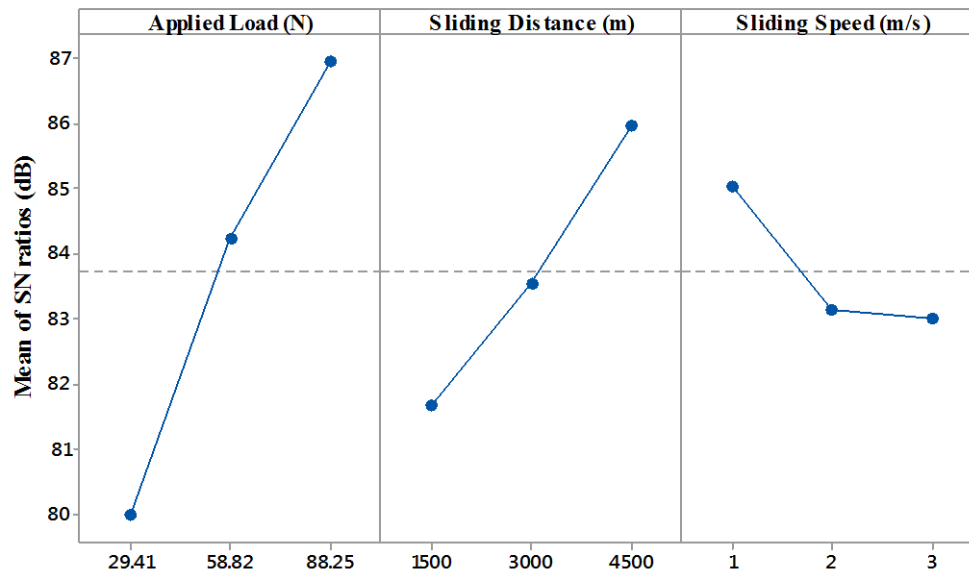
4.7.1 Wear Study on Solutionized Specimens Using Taguchi Method

To optimize the experimental variable in order to achieve the minimum wear rate, the wear process parameters were analyzed using a software called Minitab 17. The experimental values of specific wear rate are presented in Table 4.9 using which signal to noise ratio (S/N ratio) is found out. The highest value of S/N ratio gives the minimum specific wear rate (Palanikumar 2008). The overall mean value of S/N ratio, which is necessary for further analysis, is found to be 83.72 dB. The corresponding main effect plot for S/N ratios of process parameters is shown in Figure 4.41. The ranking of parameter was done with respect to delta value and recorded in Table 4.10. Delta is the difference between the maximum and minimum mean response across levels of a factor.

The specific wear rate is highly influenced by the maximum value of delta. Accordingly, the applied load has the maximum influence on the specific wear rate followed by sliding distance and sliding velocity. The influence of controlled process parameters on S/N ratios is graphically represented in Figure 4.41. It shows that optimal conditions for specific wear rate is 88.25 N load, 4500 m sliding distance and one m.s⁻¹ sliding speed. Therefore, better wear resistance of alloy was attained through the optimized parameters.

Table 4.9 Experimental layout using the L₉ orthogonal array and performance results for dry sliding wear test for Zn-24Al-2Cu alloy under solutionized condition.

Sl. No.	(A) Applied load (N)	(B) Sliding distance (m)	(C) Sliding speed (m/s)	Weight loss (g)	Specific wear rate x 10 ⁻⁵ (mm ³ /Nm)	S/N ratio (dB)
1	29.41	1500	1	0.0359	11.4034	78.8592
2	29.41	3000	2	0.0658	9.8624	80.1203
3	29.41	4500	3	0.0701	8.9672	80.9468
4	58.83	1500	2	0.0373	8.8718	81.0397
5	58.83	3000	3	0.0715	7.0996	82.9752
6	58.83	4500	1	0.035	3.6690	88.7089
7	88.25	1500	3	0.044	5.5769	85.0720
8	88.25	3000	1	0.0574	4.2120	87.5100
9	88.25	4500	2	0.0788	3.8549	88.2796



Signal-to-noise: Smaller is better

Figure 4.41 Main effect plot of S/N ratio on specific wear rate.

Table 4.10 Response table of S/N ratios on specific wear rate.

Level	(A) Applied load (N)	(B) Sliding distance (m)	(C) Sliding speed (m/s)
1	79.98	81.66	85.03
2	84.24	83.54	83.00
3	86.95	85.98	83.05
Delta	6.98	4.32	2.03
Rank	1	2	3

4.7.2 Analysis of Variance

The parameters which control the effect on S/N ratio values are analyzed by using Analysis of Variance (ANOVA) using Minitab software. Level of significance of 5% is maintained for analysis, i.e., for a confidence level of 95%. The ANOVA results are shown in Table 4.11. P-value factor is statistically significant if it is less than 0.05 and has a major influence on the S/N ratio (Rajesh et al., 2012). Table 4.11 shows that applied

load (58.25 %) has the highest influence on specific wear rate preceded by sliding distance (28.19 %) and sliding velocity (8.32 %) and the pooled error accounts only 5.22 %.

Table 4.11 Analysis of variance for S/N Ratio.

Source	Degree of freedom (DOF)	Adjacent sequential sum	Adjacent mean sum	F-value	P-value	P %
Applied load	2	74.25	37.13	19.58	0.049	58.25
Sliding distance	2	28.17	14.09	7.43	0.119	28.19
Sliding speed	2	7.67	3.83	2.02	0.331	8.32
Error	2	3.79	1.89			5.22
Total	8	133.88				100

4.7.3 Multiple Linear Regression Model

A regression model has been developed based on the values of wear parameters and experimental results. Here a relationship is established between predictor variables and response variables by fitting a linear equation using Minitab 17 software. The regression equation developed for S/N ratio is shown in Equation 4.6:

$$\text{S/N Ratio} = 74.45 + 0.1186 (A) + 0.001440 (B) - 1.014 (C) \quad \text{Equation 4.6}$$

The recorded values of the variables were substituted into Equation 4.6 and the S/N ratio of the materials can be calculated for any combination of applied load (A), sliding distance (B) and sliding speed (C). The result shows that the estimated model for specific wear rate is significant at the level of 0.05 and the goodness of fit was checked by calculating R-squared (R^2) value. The values of both R^2 and adjusted R^2 are 94.15% and 90.64% of the response variation in the model and both the values show that the data are well fitted.

4.7.4 Confirmation Test

The confirmatory test is the essential step to validate the conclusion drawn during analysis. Table 4.12 shows selected set of factors and levels for confirmation test, where the first set parameter is optimal parameters and another set of values are randomly chosen with reference to Table 3.3. The predictions of response under optimal conditions were determined and a new set of experiments according to optimal conditions were carried out for comparison. Based on the confirmation experiment, the errors associated with S/N ratios range between 2.3 to 6.7 %. The error is within permissible level of 7 %. Therefore, obtained regression model can be effectively used to predict the wear rate of the Zn-24Al-2Cu alloy with good accuracy.

Table 4.12 Parameters and values used in the confirmation test and their comparison with a regression model.

Sl. No.	Applied load (N)	Sliding distance (m)	Sliding speed (m/s)	Predicted S/N ratio's	Experimental S/N ratio's	% Error
Optimal parameters						
1	88.25	4500	1	90.38	88.30	2.3
Randomly chosen parameters						
1	44.12	2250	1.5	81.40	86.85	6.7
2	63.75	2950	1.8	84.43	81.39	3.6
3	73.10	3750	2.5	85.98	82.28	4.3

4.7.5 Wear Behavior of Solutionized and Aged, MDF Processed, MDF with Post-Aging Samples using Optimized Parameters

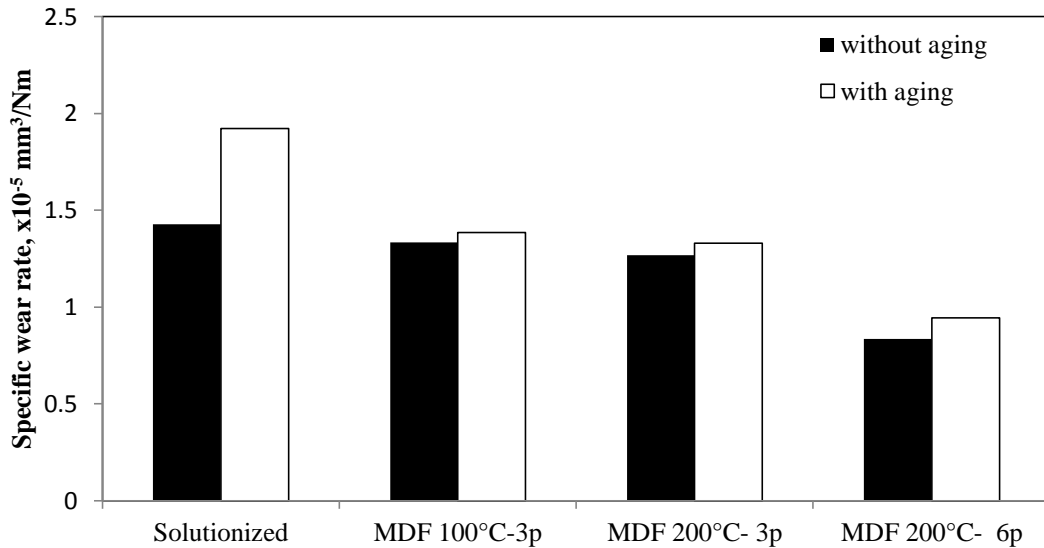


Figure 4.42 Variations of specific wear rate for different processing conditions.

The specific wear rate of the samples processed at different conditions with applied load of 88.25 N, sliding distance of 4500 m and sliding speed of one ms^{-1} are depicted in Figure 4.42. The specific wear rate of the MDF processed sample decreased as compared to solutionized samples. Samples which are processed by MDF at 200 °C for six passes exhibit minimum wear rate compared to those materials processed by different routes. This is expected because this alloy has exhibited the highest tensile strength and ductility. The foremost important features that influence the improvement of wear resistance of MDF processed samples are: higher strength, finer grain size and increased ductility. It is inferred from the charts presented in Figure 4.42 that MDF process improves the wear resistance, particularly with longer sliding distance and higher applied loads. It is predominantly due to better ductility and enhanced strength after processing the alloy in addition to refinement in the ϵ -phase. Aging heat treatment further increases the strength of this alloy, but reduces its wear resistance slightly. The reduction in wear resistance of this alloy may be related to over aging caused by temperature increase in the vicinity of

the subsurface region of the sample during dry sliding operation which reduced the hardness of the alloy (Avner 1974).

4.7.6 Mechanism of Wear

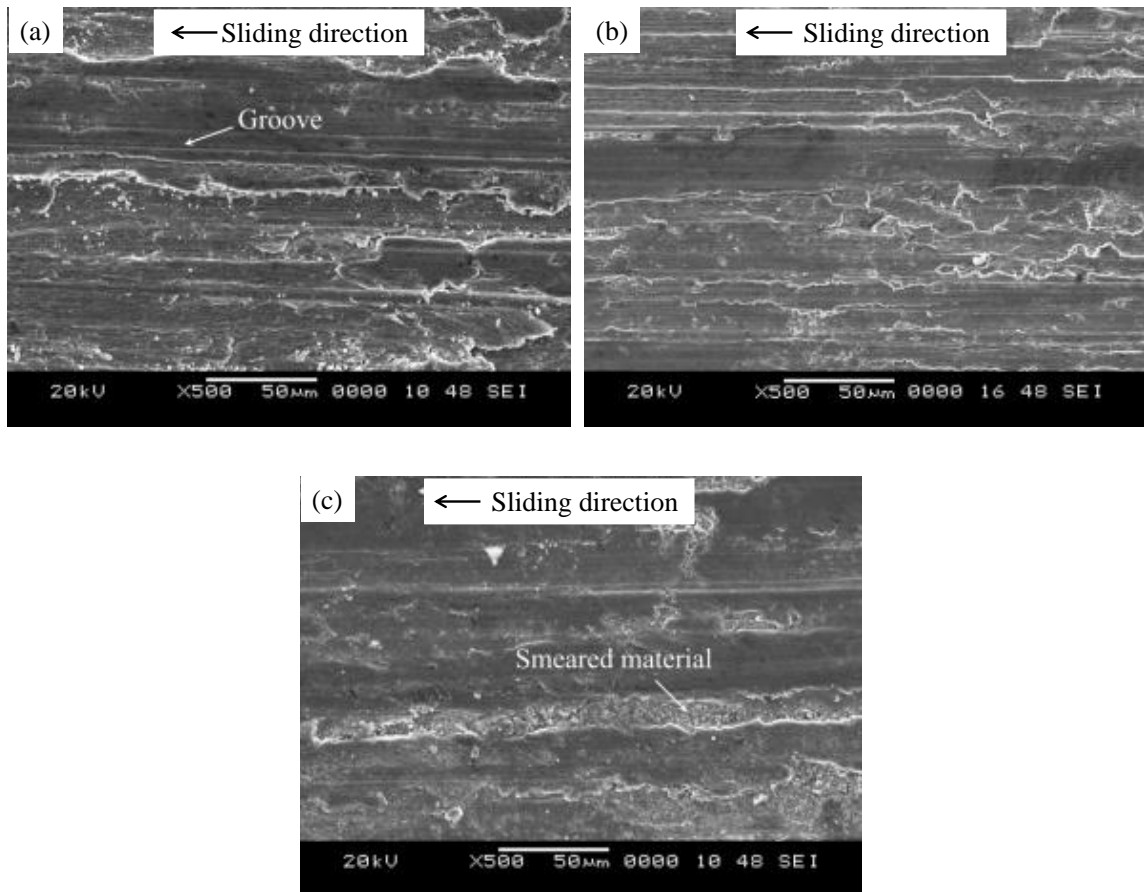


Figure 4.43 SEM micrographs showing the appearance of worn surfaces of (a) solutionized, (b) MDF at 100 °C up to three passes and (c) MDF at 200 °C for six passes.

The worn surface images of the solutionized and MDF processed samples after 4500 m sliding distance with applied load of 88.25 N and sliding speed of one $\text{m}\cdot\text{s}^{-1}$ are shown in Figure 4.43. Enlarged images of worn surfaces of the MDF processed samples with different number of passes are shown in Figure 4.44 with energy dispersive X-Ray spectroscopy (EDS) analysis which is shown in Figure 4.45.

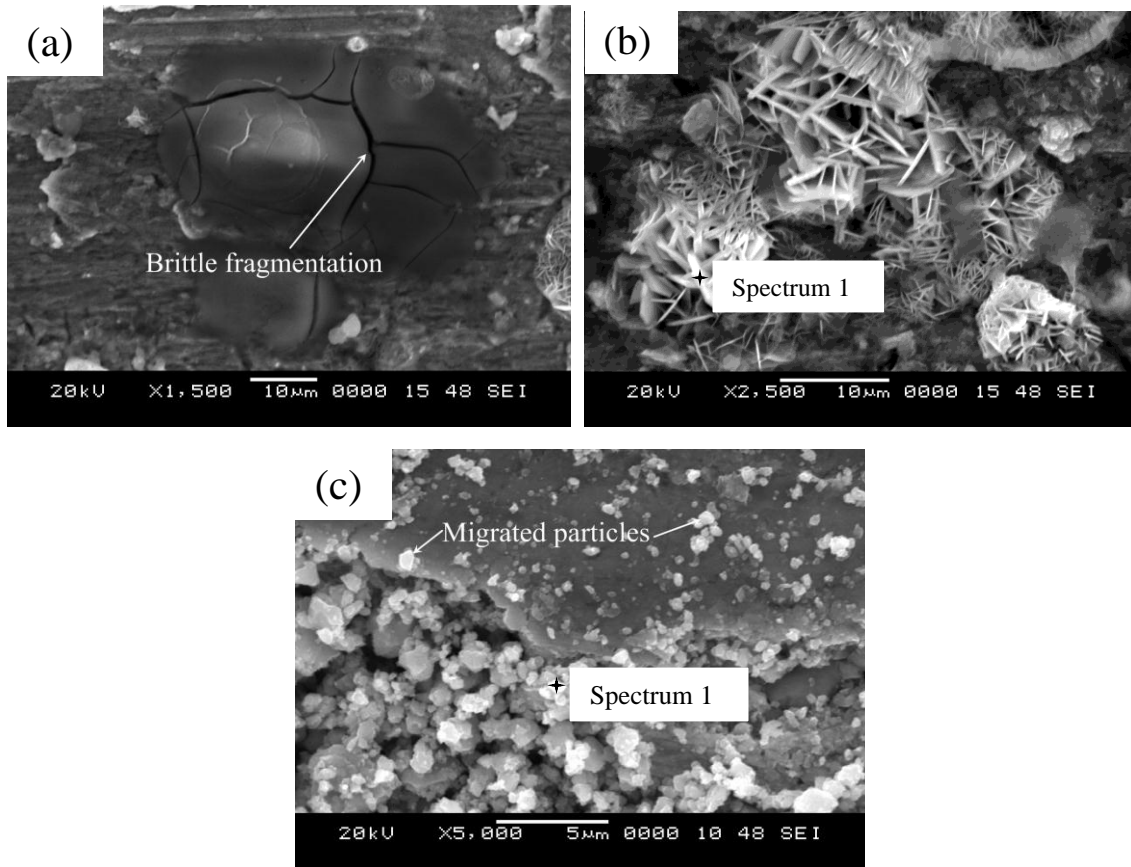


Figure 4.44 SEM micrographs showing enlarged images of worn surfaces (a) of brittle fragmentation in MDF at 100 °C up to three passes, (b) with ϵ particles in η phase for MDF at 100 °C up to three passes and (c) with migrated particles for MDF at 200 °C up to six passes.

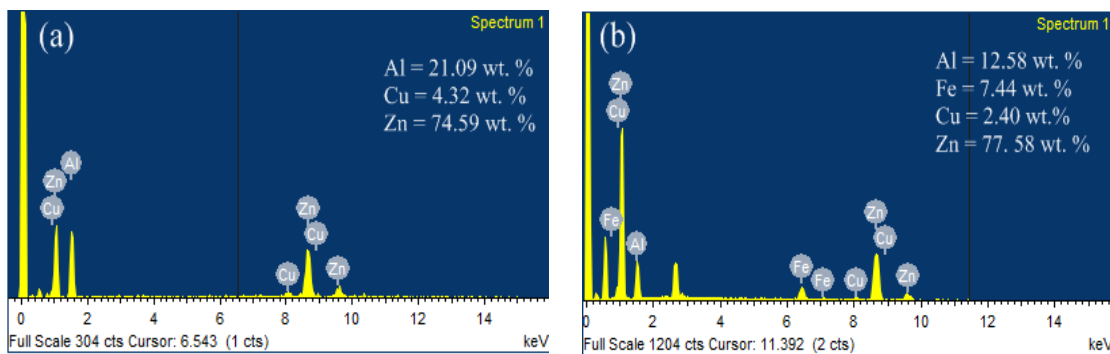


Figure 4.45 Results of EDS analysis on the worn surface of the Zn-24Al-2Cu alloy (a) MDF at 100 °C – 3 pass (see Figure 4.43(b)) and (b) MDF at 200 °C – 6 pass (see Figure 4.43(c)).

Figure 4.46 shows the microstructural features of the sections below the wear surface of the solutionized, MDF and MDF with post-ageing of samples taken after wear tests for 1.15 hours corresponding to an applied load of 88.25 N, sliding distance of 4500 m and sliding speed of one m.s^{-1} .

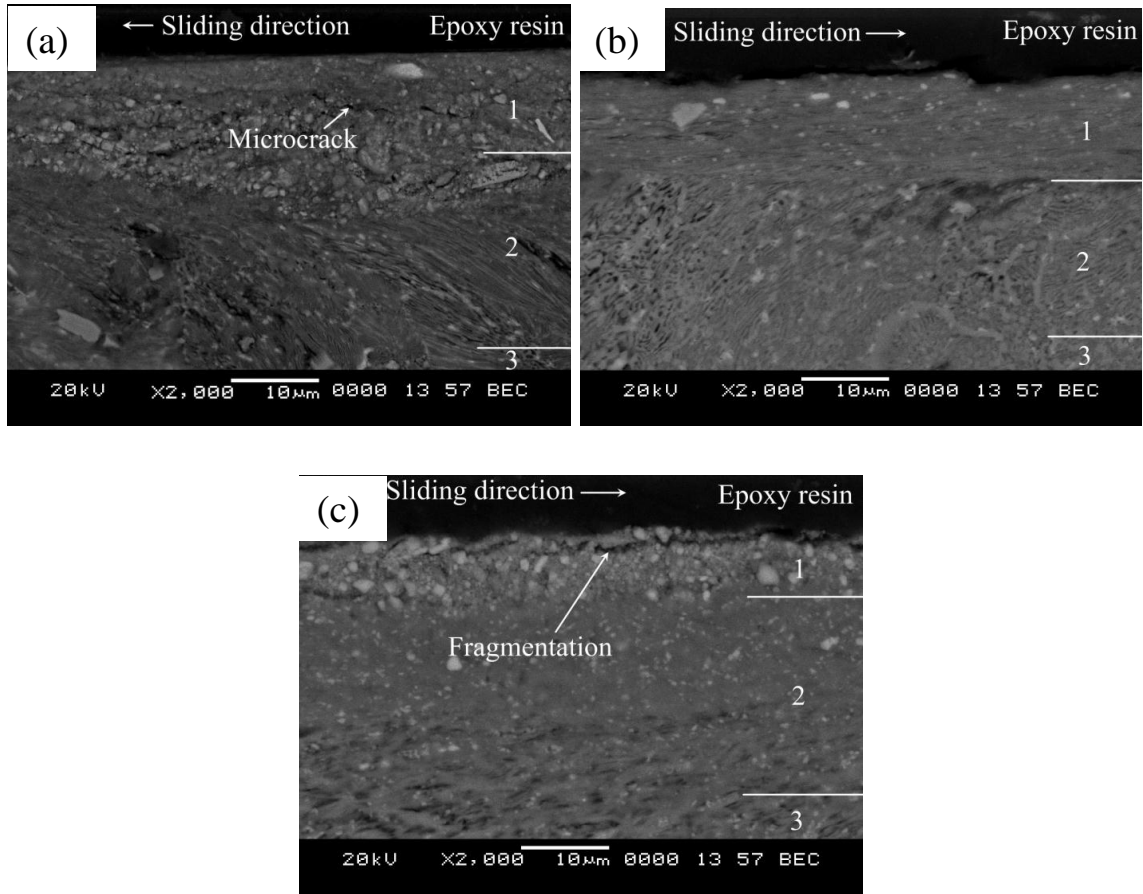


Figure 4.46 SEM micrograph showing the subsurface regions of (a) Solutionized (b) MDF at 200 °C - 6 pass and (c) MDF at 200 °C - 6 pass + aging.

Wear is a complex phenomenon occurring at the mating interfaces of two bodies. Not only mating surfaces, but also debris caught in between them take part in wear events. In the present study, choice of hardened steel material as the wear plate enables one to consider the wear mechanism being controlled by microstructural constituents of soft Zn-24Al-2Cu pin material. The worn surface images of the solutionized and MDF processed

samples after 4500 m sliding distance with applied load of 88.25 N and sliding speed of one m.s^{-1} are shown in Figure 4.43. In solutionized condition material, it is found to be consisting of three phases α phase, η phase and intermetallic compound ϵ phase. Out of three phases, ϵ phase is the hardest phase and most likely to come out of the matrix α and η phase, which generates the debris during the wear process, but in solutionized sample these particles are relatively large and segregated. Owing to their ploughing action, they cause large weight loss during sliding. The wear track formed by these debris is visible in Figure 4.43 (a) suggesting that the abrasive wear is the dominant mechanism for the solutionized materials. Solutionized material combined with aging at 100 °C for one hour is similar to the solutionized sample with fine debris of ϵ phase smeared over the surface. Smearing action may take place owing to back transfer of the wear material from disc to sample surface. Hardness of the sample and fineness of the debris are the two important factors which control the back transfer process. The finer the debris particle more will be the back transfer. Wear mechanism is changed after MDF process due to back transfer and when the base matrix (η phase) of the sample comes into contact with wear plate. SEM images in the Figure 4.43 (b) for MDF at 100 °C up to three passes reveal that wear tracks are replaced by adhesive patches. In the case of MDF at 200 °C up to six pass material, the ϵ phase got fractured during forging and became more homogeneous in the structure and such smeared particles over the surface are visible in Figure 4.43 (c). In the case of MDF processed at 100 °C up to three pass samples, the adhesion was the dominant mechanism with brittle fragmentations additionally contributing to material loss as shown in Figure 4.44 (a). Flake or needle type wear particles were observed inside the η phase with dissimilar size and shapes as revealed in Figure 4.44 (b). The chemical composition of these particles was confirmed to be 21.09 Al-4.32 Cu-74.59 Zn (wt. %) by means of the EDS analysis and it is presented in Figure 4.45 (a). Migrated particles were smeared over the sample surface which are discerned in Figure 4.44 (c). The chemical composition of the migrated particles is confirmed as 12.58 Al-7.44 Fe-2.4 Cu-77.58 Zn (wt. %) by means of the EDS analysis and it is presented in Figure 4.45 (b).

Similar type of wear mechanism was observed for MDF processed combined with aging heat treated samples.

Figure 4.46 (a-c) shows the microstructural features of the sections below the wear surface of the solutionized, MDF and MDF with post-aging samples taken after wear tests for 1.15 hours corresponding to an applied load of 88.25 N, sliding distance of 4500 m, and sliding speed of one m.s^{-1} . Micrograph of subsurface reveals three distinct regions marked as 1, 2 and 3. The uppermost region 1 reveals fine grain wear particles which are smeared and embedded in the surface. Region 2 shows flow line in the sliding direction. Finally, region 3 represents the unaffected bulk structure. For an MDF processed sample, region 1 shows very thick layer as compared to the solutionized sample. This layer contains fractured ϵ particles which spread over the entire surface and forms continuous solid lubricant. In the case of solutionized sample, these ϵ particles are large and non-uniformly distributed which may increase the abrasive action; it is seen in Figure 4.46 (a). In MDF process, samples are forged in multiple directions and aging heat treatment is carried which alters the size of the ϵ particles and distribution is more homogeneous as seen in Figure 4.46 (b and c). Thus, wear resistance is improved after processing the sample by minimizing the abrasive action caused by ϵ particles. The results from the present experiments clearly show that wear resistance of the Zn-24Al alloy containing a small amount (2 wt. %) of Cu can be increased. Improvement in wear resistance can make these alloys very attractive compared to traditional bearing alloys. Also, the improvement in wear resistance is significant at high pressures and long range distances which provide competencies for these alloys in different tribological applications, including low speed (low temperature) and high load.

The as-cast Zn-Al alloy has dendritic structure which results in lower ductility and high heterogeneity in the mechanical properties and hence their utility is generally restricted. After solutionizing heat treatment and MDF processing at 200 °C up to six passes i.e., total equivalent strain of 1.2, both strength and ductility of the material are improved to an larger extent due to grain refinement, bi-modal structure and uniform distribution of the Al-rich phase in the Zn-rich matrix. After post-aging of such MDF processed sample

at 100 °C for one hour, strength of the material is further improved along with maintaining good ductility. Wear behavior of the processed samples is better than initial solutionized samples. Hence, processed materials combined with aging heat treatment at 100 °C for one hour is suitable for many structural and engineering applications such as manufacturing of bearings and automobile components.

Chapter 5

CONCLUSIONS

It has received much attention about the development of producing bulk ultra-fine grained materials by imposing MDF technique. MDF of Zn-Al-Cu based alloys has received little attention and hence main objective is to enhance the mechanical properties such as tensile, creep and wear behavior of Zn-24Al-2Cu material through MDF process. The experiments were conducted and results are discussed. The conclusions drawn are presented in this chapter.

1. The bulk Zn-24Al-2Cu alloy was successfully processed with no sign of macro-defects by the MDF at higher temperature of 100 °C up to three passes and 200 °C up to six passes.
2. The average grain size was reduced from 30 µm to 2 µm in the case of MDF processed at 100 °C up to three passes, 1.5 µm and 1 µm for MDF processed at 200 °C up to three and six passes respectively. The initial lamellar Al-rich and Zn-rich phase were gradually refined to a spherical shape and distributed more uniformly with increasing number of passes. Moreover, the process carried out at 200 °C showed well refined uniform microstructure.
3. Ultimate tensile strength was increased from 185 MPa to 267 MPa by MDF processing at 100 °C up to three passes and 276 MPa in the case of sample processed at 200 °C up to six passes. Due to grain refinement, ultimate tensile strength has been increased and for similar reasons the ductility of the material showed 21% when MDF processed at 200 °C for six passes.
4. Precipitation hardening heat treatment results in peak aging occurring at 100 °C for one hour duration.
5. After post-aging of MDF processed sample at 100 °C for one hour, the average grain size was 2.3 µm for sample MDF processed at 100 °C up to three passes. It was 1.8 µm and 1.3 µm for samples MDF processed at 200 °C up to three and six passes respectively.

6. Materials MDF processed at 200 °C up to six passes possess the strength of 276 MPa with ductility of 21 %. Further, when such materials are aged at 100 °C for one hour tensile strength has been increased to 311 MPa with 20% ductility.
7. Creep curves generated from impression testing depict, steady state creep rate are not sensitive to microstructural features if tested at 30 °C. It increases to a maximum at the testing temperature of 100 °C and then starts decreasing if tested at higher temperature. Initial stress exponent values are in the range of 2.5 to 12.4. This high value of n for the Zn-24Al-2Cu alloy is higher than usually reported and it is confirmed from the present study that these differences in n values arise from the presence of threshold stress.
8. The true activation energy is calculated by considering the temperature dependence and it is in the range of 22 - 129 kJ/mol. For solutionized material, lattice diffusion mechanism has been suggested and for MDF processed materials creep mechanism is possibly dominated by lattice diffusion controlled by dislocation climb. The main result of the creep test on Zn-24Al-2Cu alloy with a very small grain size of 1 μm (MDF at 200 °C up to six pass sample) exhibits different creep properties from the same alloy with a grain size of 30 μm (Solutionized sample), when samples of both grain sizes are tested under the same range of stresses and temperatures.
9. Multiple linear regression model developed based on wear parameter suggests that applied load plays the most prominent role in the wear behavior of solutionized Zn-24Al-2Cu alloy followed by sliding distance and sliding speed. This fact is confirmed by experimentation.
10. Wear study of solutionized samples using Taguchi's approach indicated that specific wear rate was highly influenced by applied load and sliding distance. Solutionized samples show relatively higher wear resistance as compared to aged samples when tested with higher applied load, long sliding distance and lower speed. It was due to copper-rich intermetallic ϵ compound which is large in size, thereby increasing the abrasive action resulting in more weight loss.

11. Wear resistance of MDF sample and post-aged MDF processed sample was significantly improved as compared to solutionized combined with aging heat treated samples by refining the grain size and ϵ phase particles during the processing.
12. Adhesive type of wear mechanism has been proposed as revealed by SEM investigation of worn surfaces of processed samples. Brittle fragmentations together with flake or needle shape particles were identified in the η phase for MDF processed alloy at 100 °C up to three passes. In the case of alloy processed by MDF at 200 °C up to six passes, migrated particles were smeared over the sample surface which enhanced the wear resistance.

Scope for Future Work

Zn-24Al-2Cu alloy were processed through MDF up to six passes at 100 °C and 200 °C temperature. Microstructural studies were done using optical microscopy and electron microscopy. Mechanical properties have been improved in terms of ultimate tensile strength, percentage of elongation and hardness of the alloy. Fracture analysis and X-Ray diffraction analysis was done to know the behavior of the alloys after MDF. Post-aging heat treatment was carried out on MDF processed samples. Indentation creep and dry sliding wear behavior of MDF processed alloy was carried out. Apart from these characterization and observations, the following various studies can be considered to meet the requirement of the different applications.

- Wear behavior of the material under lubricated conditions can be considered for practical usage of this material in bearings.
- Electron back scattered diffraction (EBSD) study is in need for textures analysis, so that one can understand the behavior of material with different orientation of grains.
- Mechanical properties can be enhanced by additions of ceramics or other alloying elements to the base Zn-Al-Cu alloy and further processing through MDF technique.

- Further, fatigue and corrosion study is important for considering structural high temperature applications of Zn-Al alloy in the environment of intended applications.

REFERENCES

- Alibabaie, S., and Mahmudi, R. (2012). "Microstructure and creep characteristics of Zn–3Cu–xAl ultra high-temperature lead-free solders." *Materials & Design*, 39, 397-403.
- Al-Maharbi, M., Karaman, I., and Purcek, G. (2010). "Flow response of a severe plastically deformed two-phase zinc–aluminum alloy." *Materials Science and Engineering A*, 527(3), 518–525.
- Archard, J. (1953). "Contact and rubbing of flat surfaces." *Journal of applied physics*, 24(8), 981-988.
- Arieli, A., and Mukherjee, A. K. (1980). "High-temperature diffusion-controlled creep behavior of the Zn-22% Al eutectoid alloy tested in torsion." *Acta Metallurgica*, 28(11), 1571-1581.
- Ashby, M. F., and Lim, S. C. (1990). "Wear-mechanism maps." *Scripta Metallurgica et Materialia*, 24(5), 805-810.
- ASM Handbook. (1992). *Alloy Phase Diagrams*, ASM International, Tenth Edition, Volume 3, Metals Park, OH.
- Avner, S. H. (1997). *Introduction to Physical Metallurgy*. Tata McGraw-Hill Publication Second Edition.
- Babic, M., Mitrovic, S., and Jeremic, B. (2010). "The influence of heat treatment on the sliding wear behavior of a ZA-27 alloy." *Tribology International*, 43(1-2), 16–21.
- Babic, M., Ninkovi, R., Mitrovi, S., and Bobi, I. (2007). "Influence of heat treatment on tribological behavior of Zn-Al alloys." *Tribology in Industry*, 29, 23–31.
- Basavarajappa, S., and Chandramohan, G. (2005). "Wear studies of metal matrix composites: a Taguchi approach." *Journal of Material Science Technology*, 21, 845-850.

Bhaskar, H., B. and Abdul Sharief. (2012). "Dry sliding wear behavior of Aluminium /Be₃Al₂(SiO₃)₆ composites using Taguchi method." *Journal of Minerals and Material Characterization and Engineering*, 11, 679-684.

Bhushan, B. (2002). *Introduction to Tribology*. Second edition, John Wiley & Sons, New York.

Chaudhury, P. K., and Mohamed, F. A. (1988). "Effect of impurity content on superplastic flow in the Zn-22% Al alloy." *Acta Metallurgica*, 36(4), 1099-1110.

Chauhan, M., Roy, I., and Mohamed, F. A. (2005). "Creep behavior in near-nanostructured Al 5083 alloy." *Materials Science and Engineering: A*, 410, 24-27.

Cho, T., Lee, H., Ahn, B., and Kawasaki, M. (2014). "Microstructural evolution and mechanical properties in a Zn-Al eutectoid alloy processed by high-pressure torsion." *Acta Materialia*, 72, 67–79.

Choi, I. C., Kim, Y. J., Ahn, B., Kawasaki, M., Langdon, T. G., and Jang, J. I. (2014). "Evolution of plasticity, strain-rate sensitivity and the underlying deformation mechanism in Zn-22% Al during high-pressure torsion." *Scripta Materialia*, 75, 102–105.

Chou, C.Y., Lee, S.L., Lin, J.C., and Hsu, C.M. (2007). "Effects of cross-channel extrusion on the microstructures and superplasticity of a Zn–22wt.% Al eutectoid alloy." *Scripta Materialia*, 57(10), 972–975.

Conroad, H. and Dorn, J. E. (1961). *The role of grain boundaries in creep and stress rupture*. New York, McGraw Hill.

Cottrell, A.H. (1953). *Dislocations and plastic flow in crystals*, Oxford University Press, London.

Dieter, G. E. (1988). *Mechanical Metallurgy*. UK, McGraw Hill.

Dorantes-Rosales, H. J., Lopez-Hirata, V. M., and Zhu, Y. H. (1999). "Decomposition process in a Zn-22wt.% Al-2wt.% Cu alloy." *Materials Science and Engineering A*, 271, 366–370.

Dorantes-Rosales, H. J., Lopez-Hirata, V. M., De Jesus Cruz-Rivera, J., and Saucedo-Muñoz, M. L. (2005). "Coarsening of τ' precipitates during aging in a Zn–22 wt.% Al–2 wt.% Cu alloy." *Materials Letters*, 59(16), 2075–2078.

Dorantes-Rosales, H. J., López-Hirata, V. M., Moreno-Palmerin, J., Cayetano-Castro, N., Saucedo-Muñoz, M. L., and Castillo, A. T. (2007). " β' Phase decomposition in Zn-22 mass%Al and Zn-22 mass%Al-2 mass%Cu alloys at room temperature." *Materials Transactions*, 48(10), 2791–2794.

Dorantes-Rosales, H., Rivas-Lopez, D., Hernandez-Santiago, F., Saucedo-Munoz, M., and Lopez-Hirata, V. M. (2002). "Microstructural changes of the as-quenched Zn-22 mass% Al-2 mass% Cu alloy during cold rolling." *Materials Transactions*, 43(5), 1240–1242.

Durman, M., and Murphy, S. (1997). "An electron metallographic study of pressure die-cast commercial zinc–aluminium-based alloy ZA27." *Journal of Materials Science*, 32(6), 1603-1611.

El Aal, M. I. A., El Mahallawy, N., Shehata, F. A., El Hameed, M. A., Yoon, E. Y., and Kim, H. S. (2010). "Wear properties of ECAP processed ultrafine grained Al-Cu alloys." *Materials Science and Engineering: A*, 527(16), 3726-3732.

Estrin, Y., and Vinogradov, A. (2013). "Extreme grain refinement by severe plastic deformation: A wealth of challenging science." *Acta Materialia*, 61(3), 782–817.

Farge, J. C. T. (1965). Recrystallization of Zinc Alloys (Doctoral dissertation, McGill University Libraries).

Frost, H.J. and Ashby, M.F. (1982). *Deformation Mechanism Maps: The Plasticity and Creep of Metals and Ceramics*. Pergamon, Oxford, U.K.

- Giourntas, L., Hodgkiess, T., and Galloway, A.M. (2015). "Enhanced approach of assessing the corrosive wear of engineering materials under impingement." *Wear*, 338, 155-163
- Gao, L. L., and Cheng, X. H. (2008). "Microstructure, phase transformation and wear behavior of Cu–10% Al–4% Fe alloy processed by ECAE." *Materials Science and Engineering: A*, 473(1), 259-265.
- Gobien, J. M., Murty, K. L., Scattergood, R. O., Goodwin, F., and Koch, C. C. (2010). "Creep behavior of ultra-fine grained Zn–4.5 Al." *Materials Science and Engineering: A*, 527(27), 7382-7386.
- Hokkirigawa, K. and Kato, K. (1988). "An Experimental and Theoretical Investigation of Ploughing, Cutting and Wedge Formation During Abrasive Wear." *Tribology International*, 21, 51-57.
- Kaibyshev, O. A. (2001). "Grain refinement in commercial alloys due to high plastic deformations and phase transformations." *Journal of Materials Processing Technology*, 117, 300–306.
- Kawasaki, M., Ahn, B., and Langdon, T. G. (2010). "Microstructural evolution in a two-phase alloy processed by high-pressure torsion." *Acta Materialia*, 58(3), 919–930.
- Korbel, A., and Richert M. (1985). "Formation of shear bands during cyclic deformation of aluminium." *Acta Metallurgica*, 33, 1971-1978.
- Kucukomeroglu, T. (2010). "Effect of equal-channel angular extrusion on mechanical and wear properties of eutectic Al–12Si alloy." *Materials & Design*, 31(2), 782-789.
- Lee, S., Tazoe, K., Mohamed, I. F., and Horita, Z. (2015). "Strengthening of AA7075 alloy by processing with high-pressure sliding (HPS) and subsequent aging." *Materials Science and Engineering: A*, 628, 56-61.

- Li, J. C. M. (2002). "Impression creep and other localized tests." *Materials Science and Engineering: A*, 322, 23–42.
- Liu, Y., Li, H., Jiang, H., and Lu, X. (2013). "Effects of heat treatment on microstructure and mechanical properties of ZA27 alloy." *Transactions of Nonferrous Metals Society of China*, 23(3), 642–649.
- Mir, A. A. (1998). The creep properties of a series of zinc-rich zinc-aluminium alloys. (Doctoral dissertation, University of Aston, Birmingham).
- Miura, H., Maruoka, T., Yang, X., and Jonas, J. J. (2012). "Microstructure and mechanical properties of multi-directionally forged Mg–Al–Zn alloy." *Scripta Materialia*, 66(1), 49–51.
- Miura, H., Kobayashi, M., and Benjanarasuth, T. (2016). "Effects of strain rate during multi-directional forging on grain refinement and mechanical properties of AZ80Mg alloy." *Materials Transactions*, 57(9), 1418-1423.
- Mohamed, F. A. (1998). "Correlation between creep behavior in Al-based solid solution alloys and powder metallurgy Al alloys." *Materials Science and Engineering: A*, 245(2), 242-256.
- Murphy, S., Savaskan, T., and Hill, J. (2013). "The creep kinetics of zinc-aluminium-based alloys." *Canadian Metallurgical Quarterly*.
- Naziri, H., and Pearce, R. (1970). "The influence of copper additions on the superplastic forming behavior of the Zn-Al eutectoid." *International Journal of Mechanical Sciences*, 12(6), 513-521.
- Ortiz-Cuellar, E., Hernandez-Rodriguez, M. A. L., and García-Sánchez, E. (2011). "Evaluation of the tribological properties of an Al–Mg–Si alloy processed by severe plastic deformation." *Wear*, 271(9), 1828-1832.

Palanikumar, K. (2008). "Application of Taguchi and response surface methodologies for surface roughness in machining glass fiber reinforced plastics by PCD tooling." *The International Journal of Advanced Manufacturing Technology*, 36(1-2), 19-27.

Paul, A., Laurila, T., Vuorinen, V., and Divinski, S. V. (2014). *Thermodynamics, Diffusion and the Kirkendall Effect in Solids*. Springer.

Phadke, and Madhav, S. (1989). *Quality Engineering Using Robust Design*. Englewood Cliffs, New Jersey: Prentice Hall.

Porter, F. C. (1991). *Zinc Handbook: Properties, Processing, and Use in Design*. CRC Press. New York.

Prasad, B. K. (1996). "Influence of heat treatment on the physical, mechanical and tribological properties of a zinc based alloy." *Zeitschrift Für Metallkunde*, 87, 226–232.

Prasad, B. K. (1998). "Tensile properties of some zinc-based alloys comprising 27.5 % Al : effects of alloy microstructure, composition and test conditions." *Materials Science and Engineering A*, 245, 257–266.

Preetham Kumar, G. V., and Uday Chakkingal. (2011). "Flow behaviour of commercial purity Titanium subjected to equal channel angular pressing." *Materials Science Forum*, 667, 867-872.

Prozhega, M. V., Tatus, N. A., Samsonov, S. V., Kolyuzhni, O. Y., and Smirnov, N. N. (2014). "Experimental study of erosion-corrosion wear of materials: A review." *Journal of Friction and Wear*, 35(2), 155-160.

Purcek, G. (2005). "Improvement of mechanical properties for Zn–Al alloys using equal-channel angular pressing." *Journal of Materials Processing Technology*, 169(2), 242–248.

Purcek, G., Saray, O., Karaman, I., and Kucukomeroglu, T. (2008). "Effect of severe plastic deformation on tensile properties and impact toughness of two-phase Zn–40Al alloy." *Materials Science and Engineering: A*, 490(1-2), 403–410.

Purcek, G., Saray, O., Kucukomeroglu, T., Haouaoui, M., and Karaman, I. (2010). "Effect of equal-channel angular extrusion on the mechanical and tribological properties of as-cast Zn–40Al–2Cu–2Si alloy." *Materials Science and Engineering: A*, 527(15), 3480–3488.

Rajesh, S., Rajakarunakaran, S., and Pandian, R. S. (2012). "Modeling and optimization of sliding specific wear and coefficient of friction of aluminum based red mud metal matrix composite using Taguchi method and response surface methodology." *Materials Physics and Mechanics*, 15, 150-166.

Rao, P. N., Singh, D., and Jayaganthan, R. (2014). "Mechanical properties and microstructural evolution of Al 6061 alloy processed by multidirectional forging at liquid nitrogen temperature." *Materials and Design*, 56, 97-104.

Reed-Hill, R. E. and Abbaschian, R. (2003). *Physical Metallurgy Principle*, Third edition, Thomson Asia Pvt. Ltd., Singapore.

Rezgui, M., Trabelsi, A., Ayadi, A., and Hamrouni, K. (2011). "Optimization of friction stir welding process of high density polyethylene." *International Journal of Production and Quality Engineering*, 2(1), 55-61.

Saito, Y., Tsuji, N., Utsunomiya, H., Sakai, T., and Hong, R. G. (1998). "Ultra-fine grained bulk aluminum produced by accumulative roll-bonding (ARB) process." *Scripta Materialia*, 39(9), 1221-1227.

Sakai, T., Belyakov, A., Kaibyshev, R., Miura, H., and Jonas, J. J. (2014). "Dynamic and post-dynamic recrystallization under hot, cold and severe plastic deformation conditions." *Progress in Materials Science*, 60, 130–207.

Salishchev, G., Zaripova, R., Galeev, R., and Valiakhmetov, O. (1995). "Nanocrystalline structure formation during severe plastic deformation in metals and their deformation behaviour." *Nanostructured materials*, 6, 913-916.

Sastry, D. H., (2005). "Impression creep technique an overview." *Materials Science and Engineering: A*, 409(1), 67-75.

Savaskan, T., and Murphy, S. (1983). "Creep behaviour of Zn--Al--Cu bearing alloys." *Zeitschrift Für Metallkunde*, 74(2), 76-82.

Savaskan, T., and Murphy, S. (1990). "Decomposition of Zn-Al alloys on quench-aging." *Materials Science and Technology*, 6, 695-703.

Stowers, I. F., and Rabinowicz, E. (1973). "The mechanism of fretting wear." *Journal of lubrication Technology*, 95(1), 65-70.

Suh, N. (1990). *The Principles of Design*. New York: Oxford University Press.

Suh, N. P., Jahanmir, S., Abrahamson, E. P., and Turner, A. P. L. (1974). "Further investigation of the delamination theory of wear." *Journal of Lubrication Technology*, 96(4), 631-637.

To, S., Zhu, Y. H., and Lee, W. B. (2006). "Ultra-precision machining induced decomposition of surface of Zn-Al based alloy." *Applied surface science*, 253, 2165-2170.

Turk, A., Durman, M., and Kayali, E. S. (2007). "The effect of manganese on the microstructure and mechanical properties of zinc-aluminum based ZA-8 alloy." *Journal of Materials Science*, 42(19), 8298-8305.

Valiev, R. Z., and Langdon, T. G. (2006). "Principles of equal-channel angular pressing as a processing tool for grain refinement." *Progress in Materials Science*, 51(7), 881–981.

- Valiev, R. Z., Estrin, Y., Horita, Z., Langdon, T. G., Zechetbauer, M. J., and Zhu, Y. T. (2006). "Producing bulk ultrafine-grained materials by severe plastic deformation." *Journal of the Minerals, Metals and Materials Society*, 58(4), 33-39.
- Valiev, R.Z., Islamgaliev, R., and Alexandrov, I. (2000). "Bulk nanostructured materials from severe plastic deformation." *Progress in Materials Science*, 45,103-189.
- Villegas-Cardenas, J., Saucedo-Muñoz, M. L., Lopez-Hirata, V. M., Dorantes-rosales, H. J., and Gonzalez-Velazquez, J. L. (2014). "Effect of phase transformations on hardness in Zn-Al-Cu Alloys." *Materials Research*, 1–8.
- Wang, C. T., Gao, N., Wood, R. J., and Langdon, T. G. (2011). "Wear behavior of an aluminum alloy processed by equal-channel angular pressing." *Journal of Materials Science*, 46(1), 123-130.
- Xun, Y., Rodriguez, R., Lavernia, E. J., and Mohamed, F. A. (2005). "Processing and microstructural evolution of powder metallurgy Zn-22 Pct Al eutectoid alloy containing nanoscale dispersion particles." *Metallurgical and Materials Transactions A*, 36(10), 2849-2859.
- Yeh, M. S., and Chang, C. B. (2002). "Microstructure effects on the forgeability of Zn-22Al eutectoid alloy." *Journal of Materials Engineering and Performance*, 11, 71–74.
- Yong, L., Nutt, S. R., and Mohamed, F. A. (1997). "An investigation of creep and substructure formation in 2124 Al." *Acta Materialia*, 45(6), 2607-2620.
- Zehetbauer, M. J., and Zhu, Y. T. (2009). "*Bulk Nanostructured Materials*". Wiley-VCH.
- Zhilyaev, A. P., and Langdon, T. G. (2008). "Using high-pressure torsion for metal processing: fundamentals and applications." *Progress in Materials Science*, 53, 893-979.
- Zhu, Y. H. (2001). "Phase transformations of eutectoid Zn-Al alloys." *Journal of Materials Science*, 36(16), 3973-3980.

Zhu, Y. H., and Islas, J. J. (1997). "Microstructures and dimensional stability of extruded eutectoid Zn-Al alloy." *Journal of Materials Processing Technology*, 66(1-3), 244-248.

Zhu, Y. H., and Lee, W. (2000). "Tensile deformation and phase transformation of furnace-cooled Zn-Al based alloy." *Materials Science and Engineering: A*, 293(1-2), 95–101.

Zhu, Y. Hua. (2004). "General rule of phase decomposition in Zn-Al based alloys (II)-on effects of external stresses on phase transformation." *Materials Transactions*, 45(11), 3083–3097.

List of Publications based on Ph.D Research Work

Sl. No.	Title of the Paper	Authors (In the same order as in the paper, underline the Research Scholar's name)	Name of the Journal / Conference / Symposium, Vol., No., Pages	Month & Year Of Publication	Category*
1	Mechanical Properties of Zn-24 wt. % Al-2 wt. % Cu alloy processing by multi directional forging	<u>Sharath, P. C.</u> , Preetham Kumar G. V. and Rajendra Udupa K.	NMD-ATM IIM 2015, PSG Coimbatore	2015	4
2	Effect of τ' Precipitates During Aging of Zn-24 wt.% Al- 2 wt.% Cu alloy	<u>Sharath, P. C.</u> , Preetham Kumar G. V. and Rajendra Udupa K.	International Journal of Core Engineering and Management, Vol. 3, page no. 25-32	2016	1
3	Impression Creep Behavior of Zn-24Al-2Cu Alloy Processed by Multi Directional Forging	<u>Sharath, P. C.</u> , Preetham Kumar G. V. and Rajendra Udupa K.	NMD-ATM IIM 2016, IIT Kanpur	2016	4
4	Effect of Multi Directional Forging on the Microstructure and Mechanical Properties of Zn-24 wt.% Al-2 wt.% Cu Alloy	<u>Sharath, P. C.</u> , Rajendra Udupa K and Preetham Kumar G. V.	Transactions of the Indian Institute of Metals, Vol. 70, page no. 89-96	2017	1
5	Effect of Multi Directional Forging on Wear Behavior of Zn-24Al-2Cu Alloy	<u>Sharath, P. C.</u> , Preetham Kumar G. V. and Rajendra Udupa K.	NMD-ATM IIM 2017, BITS Pilani Goa	2017	4

Category*

1 : Journal paper, full paper reviewed

2 : Journal paper, Abstract reviewed

3 : Conference/Symposium paper, full paper reviewed

4 : Conference/Symposium paper, abstract reviewed

5 : Others (including papers in Workshops, NITK Research Bulletins, Short notes etc.)

(If the paper has been accepted for publication but yet to be published, the supporting documents must be attached.)

Research Scholar

Research Guide

Research Guide

Sharath P C

Dr. Preetham Kumar G V

Dr. K Rajendra Udupa

List of papers communicated

Sharath, P. C., Rajendra Udupa, K., and Preetham Kumar, G. V. “Impression Creep Characteristics of Multi Directional Forged Zn-24Al-2Cu alloy.” *Materials Today*: Accepted (2017).

Sharath, P. C., Anjan B. N., Rajendra Udupa, K., and Preetham Kumar, G. V. “Mechanical and Tribological Characteristics of Zn-24Al-2Cu Alloy Processed by Multi Directional Forging.” *Journal of Materials Engineering and Performance* (Under review).

BIO-DATA

Name: Sharath P C

Father's Name: Chikkegowda P N

Date of Birth: 19-12-1988

Nationality: Indian

Marital Status: Single

Permanent Address: No. 91, "Kalabhairaveshwara Nilaya",

Behind Ramakrishna Nursing Home, Ravindranagar

M.G. Road, Hassan-573201

Mobile: +91-9036362126

E-mail: pcsharath1988@gmail.com

Academic Qualification:

Bachelor of Engineering (B.E.): Mechanical Engineering, Department of Mechanical Engineering, Malnad College of Engineering, Hassan, V.T.U University, Batch: 2006-2010.

Master of Technology (M.Tech): Process Metallurgy, Metallurgical and Materials Engineering Department, N.I.T.K, Surathkal, Batch: 2010-2012.

Work Experience:

One and half years of teaching experience as an Assistant Professor, Mechanical Engineering Department, Rajeev Institute of Technology, Hassan, V.T.U University.